

© Prince James Adeti
University of Cape Coast

UNIVERSITY OF CAPE COAST

EXTENDING THE ANALYTICAL CAPABILITIES OF THE EXISTING X-
RAY FLUORESCENCE SPECTROMETER FOR THE ANALYSIS OF
RARE EARTH ELEMENTS

BY
PRINCE JAMES ADETI

Thesis submitted to the Department of Physics of the School of Physical
Science, College of Agriculture and Natural Science, University of Cape
Coast, in partial fulfillment of the requirements for the award of Doctor of
Philosophy degree in Physics


JULY, 2021

CLASS NO.	
ACCESSION NO. 7354	
CAT. CHECKED	FINAL CHECKED

DECLARATION

Candidate's Declaration


I hereby declare that this thesis is the result of my own original research and that no part of it has been presented for another degree in this university or elsewhere.

Candidate's Signature:  Date: 23/01/2023

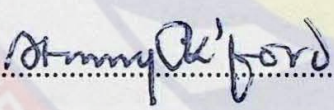
Candidate's Name : Prince James Adeti

Supervisors' Declaration

We hereby declare that the preparation and presentation of the thesis were supervised in accordance with the guidelines on supervision of thesis laid down by the University of Cape Coast.

Principal Supervisor's Signature:  Date: 24/01/22

Principal Supervisor's Name: Prof. George Amoako

Co-Supervisor's Signature:  Date: 23/01/2023

Co-Supervisor's Rev/Dr. Samuel Akoto Bamford

ABSTRACT

This study aims at extending the analytical capabilities of an existing X-ray fluorescence spectrometer, in order to provide accurate, cost-effective analytical technique for REEs analysis. This was achieved through the integration of Am-241 excitation-based system into the existing Ag anode-X-ray tube spectrometer (EXP-1) in the X-ray fluorescence (XRF) laboratory of Ghana Atomic Energy Commission (GAEC) for the analysis of rare-earth elements (REE). With the attached Am-241 excitation-based system the following REEs were identified and quantified; *Sc, Y, La, Ce, Nd, Sm, Eu, Gd* and *Er*. The "Elemental Sensitivities Method" was employed in the development of the quantitative analysis of the identified REEs. These results were confirmed by the Instrumental Neutron Activation Analysis (INAA) and the Inductively Coupled Plasma Mass Spectrometer (ICP-MS) analytical technique. On the other hand, the current EXP-1 could only identify and quantify the following REEs; *Sc, Y, and Eu*. Comparative analysis of the results of the Am-241 excitation-based system with ICP-MS and INAA technique established 80% of the reliability and accuracy of the attached Am-241 excitation-based system as alternative for analysis of REEs. This was confirmed by the statistical results which gave R^2 values higher than 0.95, slopes close to 1, and intercept close to zero (0). This means that, the results obtained using the two methods were not found to be significantly different for REEs. Consequently, the attached Am-241 excitation-based expanded the scope of analysis of REE elements for the existing XRF spectrometer (EXP-1). From the validation using the IAEA-Soil 7 reference standard.

KEYWORDS

Am-241 excitation-based System

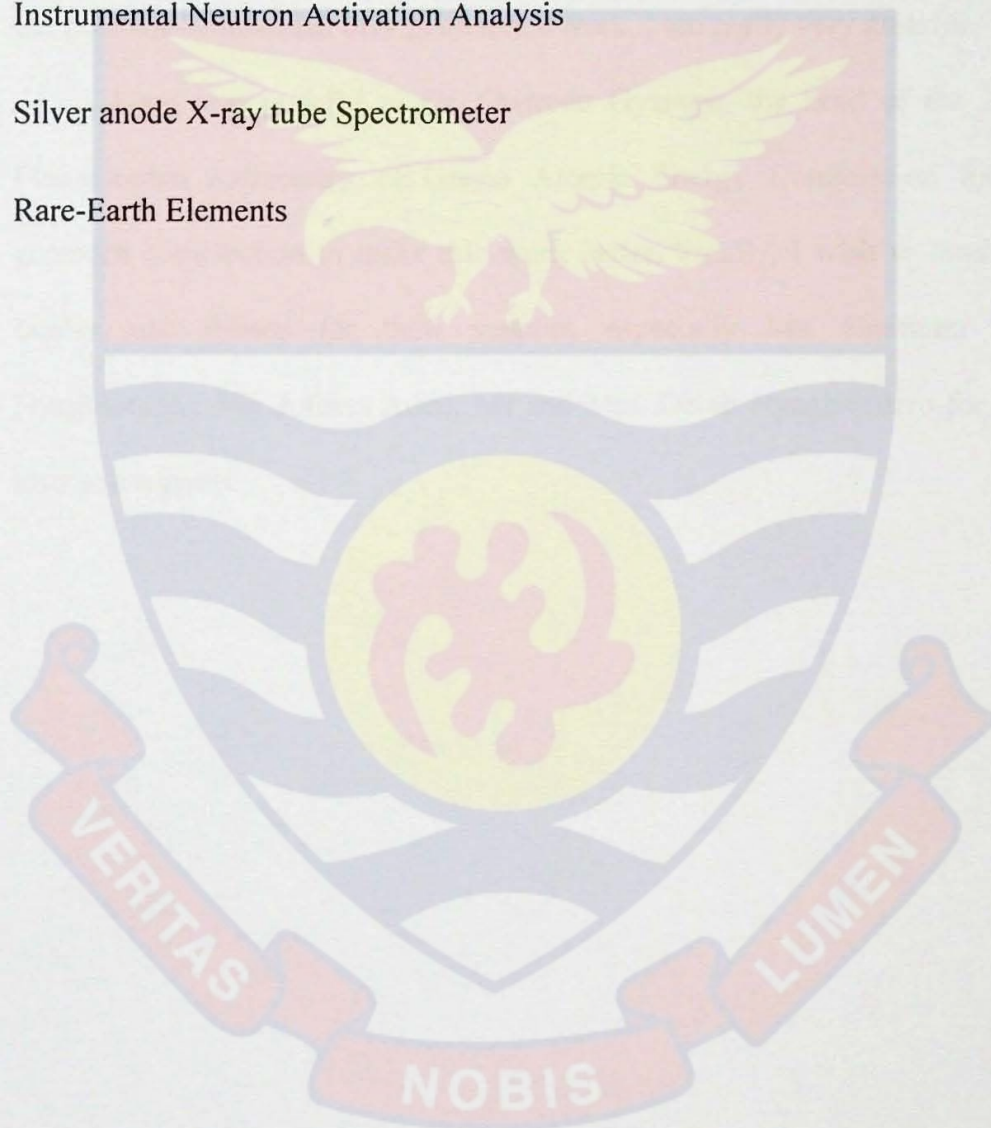
EDXRF Technique

Inductively Coupled Plasma Mass Spectrometry

Instrumental Neutron Activation Analysis

Silver anode X-ray tube Spectrometer

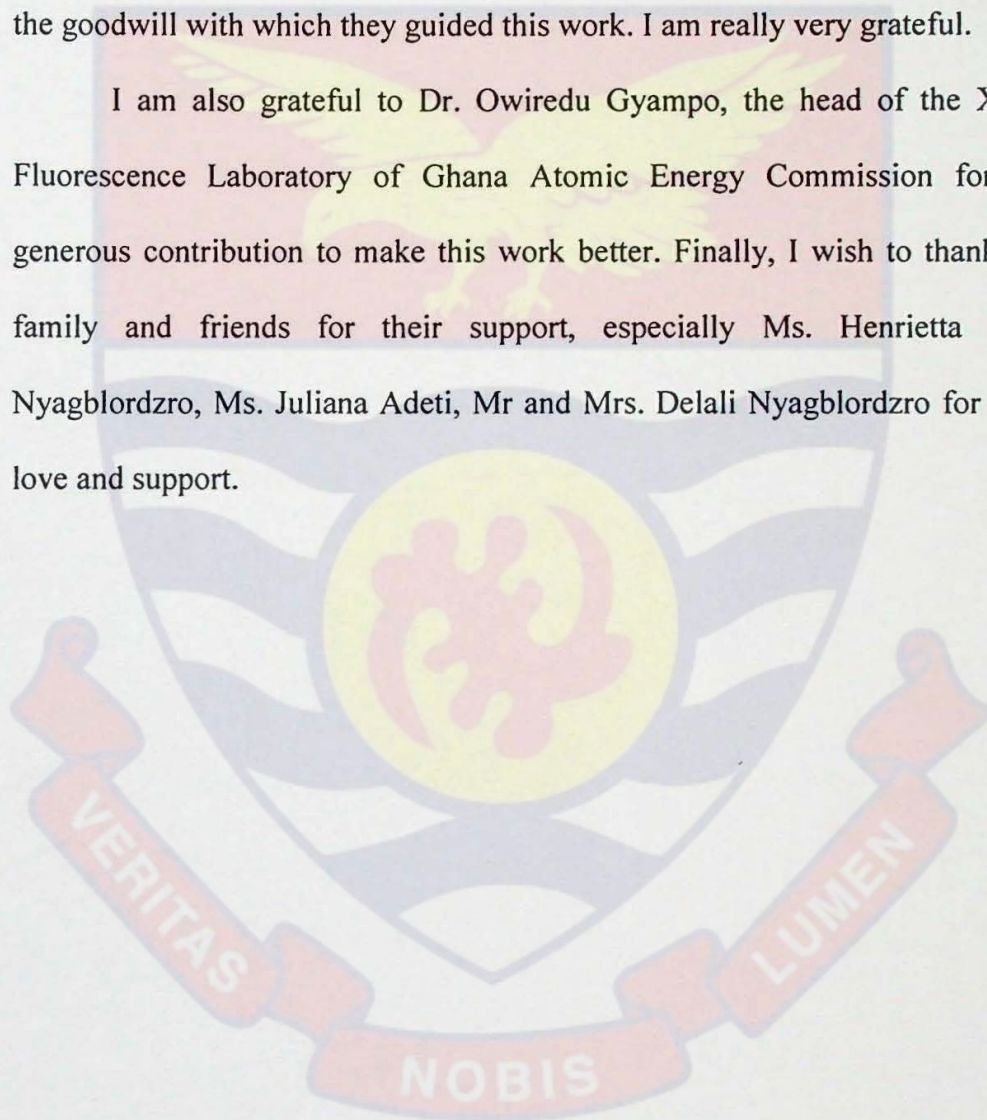
Rare-Earth Elements



ACKNOWLEDGEMENTS

I am most grateful to the Almighty God for His protection throughout the program and for seeing me to a successful end. I would like to express my sincere gratitude to my Supervisors, Rev/Dr. Samuel Akoto Bamford and Prof. George Amoako for their professional guidance, advice, encouragement and the goodwill with which they guided this work. I am really very grateful.

I am also grateful to Dr. Owiredu Gyampo, the head of the X-ray Fluorescence Laboratory of Ghana Atomic Energy Commission for his generous contribution to make this work better. Finally, I wish to thank my family and friends for their support, especially Ms. Henrietta Abla Nyagblordzro, Ms. Juliana Adeti, Mr and Mrs. Delali Nyagblordzro for their love and support.



DEDICATION

To my parents of blessed memory



TABLE OF CONTENTS

DECLARATION	ii
ABSTRACT	iii
KEYWORDS	iv
ACKNOWLEDGEMENTS	v
DEDICATION	vi
LIST OF TABLES	xi
LIST OF FIGURES	xii
CHAPTER ONE: INTRODUCTION	
Background to the Study	1
Statement of the Problem	8
Significance of the Study	10
Delimitation	10
Limitations	11
Organization of the Study	12
CHAPTER TWO: LITERATURE REVIEW	
Introduction	13
Overview of Rare Earth Elements	14
Technological Applications of Rare Earth Elements	15
Mineralogy of Rare Earth Elements Ore Deposits	16
Global Rare Earth Resources and Production	19
Types of Rare Earth Elements Deposits	20
Alkaline Igneous Rare Earth Elements Deposits	20
Residual Deposits	23

Placer Deposits with Heavy Mineral	23
Rare-Earth Elements in Coal Deposit	24
Rare Earth Elements in Sediments of Continental Shelf and Ocean Bottom	25
Extraterrestrial Rare Earth Elements Resources	28
Rare Earth Elements in Agriculture	29
Rare Earth Elements in Medicine	30
Analytical Techniques used in Mining Rare-Earth Elements	31
Laser-Induced Breakdown Spectroscopy (LIBS)	34
Instrumental Neutron Activation Analysis (INAA)	34
Inductively Coupled Plasma Optical Emission Spectrometry (ICP OES)	36
Microwave Plasma Atomic Emission Spectrometry (MP-AES)	38
Glow Discharge Mass Spectrometry	39
X-ray Fluorescence Spectrometry (ED-XRF)	39
Principle of X-ray Fluorescence	41
Interaction of X-rays with Matter	42
Scattering	42
Photoelectric Effect	43
X-ray Absorption Phenomena	44
X-ray Fluorescence Spectroscopy (XRF)	48
Statistical Theory for Method Validation	69
Chapter Summary	70
CHAPTER THREE: RESEARCH METHODS	

Introduction	71
Research Design	72
Sample Collection	73
Sample Preparation	73
X-Ray Spectrometer Re-configuration	78
X-ray Spectrometer Chamber and Sample Holder Construction	77
Description of Instrumentation Systems	78
Laboratory Analysis and Identification of Elements	86
Quality Control	92
Chapter Summary	94
CHAPTER FOUR: RESULTS AND DISCUSSIONS	
Introduction	95
Energy Calibration	95
Redesigned Optimum Source-Sample-Detector Geometry for the Am-241 Excited-based System	96
Method validation	107
Application in Rare Earth Elements Analysis	116
Chapter Summary	132
CHAPTER FIVE: SUMMARY, CONCLUSIONS AND RECOMMENDATIONS	
Introduction	134
Summary	134
Conclusions	135
Recommendations	136

REFERENCES	138
APPENDIX	
Appendix A	167
Appendix B	167
Appendix C	168
Appendix D	169



LIST OF TABLES

	Page
1. The Selected REEs Containing Minerals, Formular and Approximate REO	17
2. For Reference Materials, an Analytical System has been Devised 899	
3 Intensity and the Background Produced from the Various Distance from the Am-241 Source	98
4. The Standards with their Respective Concentrations for Sensitivity Calibration	100
5. The Standards used in the $K\alpha$ -sensitivity Curve and their Fitted Intensity Values	101
6. The Standards used in the $L\alpha$ -sensitivity Curve and their Fitted Intensity Values	104
7. Testing the Repeatability/Precision of Am-241 and Ag-X-ray Tube EDXRF Spectrometer	108
8. Accuracy and Standard Deviation	115

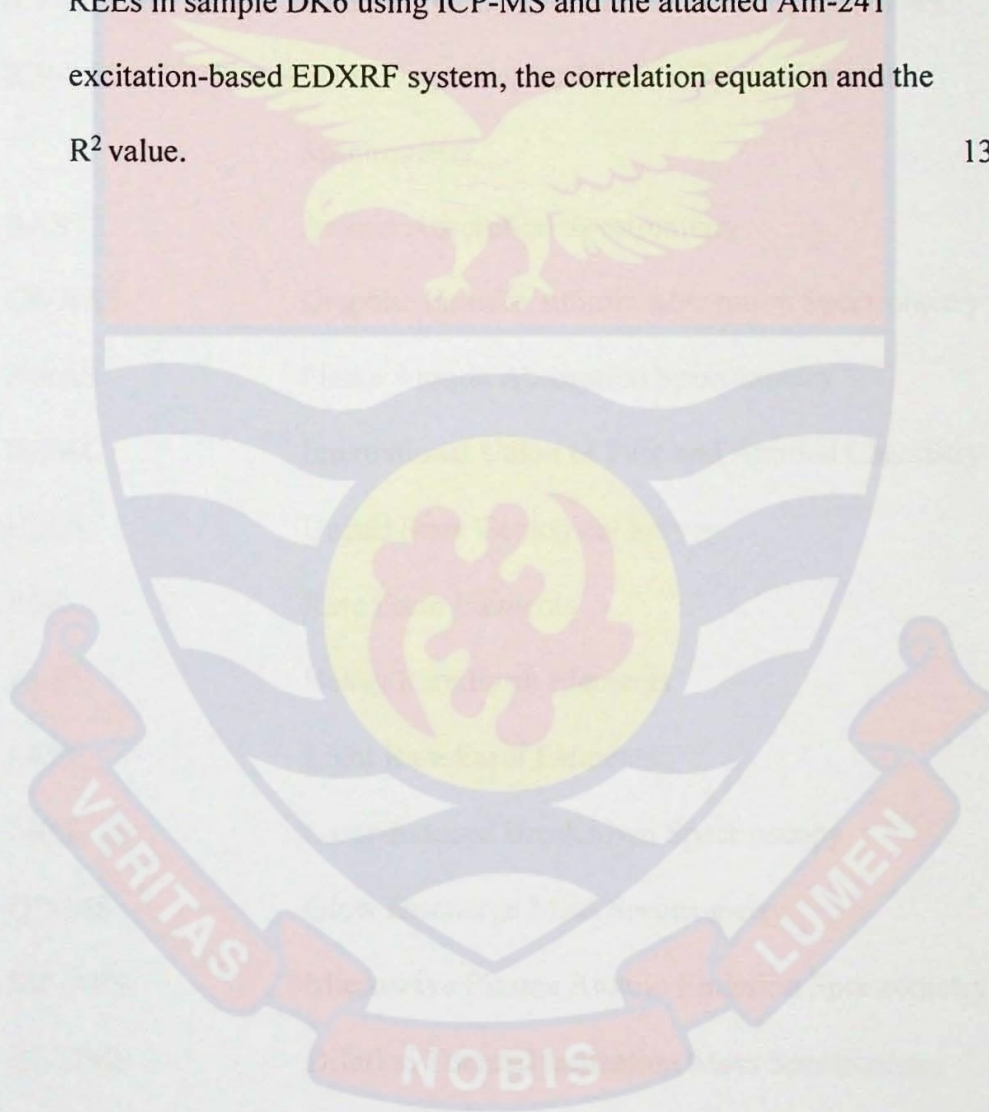
LIST OF FIGURES

	Page
1. Light (marked Purple) and Heavy (marked Orange) Rare-Earth Elements on the Periodic table	3
2. Usage of Rare earth Elements in U.S (USGS, 2013)	4
3. Interaction of X-ray with Matter (Jenkins, 1995)	42
4. Observed Characteristic Line in K Series for X-ray Fluorescence (Moore, 2014)	50
5. Diagram Showing the Am-241 Decay Scheme with two Major Energies Emitted at 59.5 keV and 26.3 keV	52
6. Project Framework	72
7. Assembly of the Pressing Die	74
8. Prepared Pellets in a Petri-dish	75
9. Photograph of EXP-1 (a) with the Attached Am-241 excitation-based System (b), Connected to the Monitor to Display the Spectra	778
10. Aluminium Plate that Serve as the Spacer and the Sample Holder	78
11. Labelled EXP-1, Ag anode X-ray Tube Spectrometer Experimental Setup at GAEC	79
12. Am-241 Excited-based System Experimental Setup	80
13. Optimum Source-Sample-Detector Geometry for Am-241 Excited-based System (measurements in degrees and millilitres) Excited-Based	81

14.	An Overview of AXIL Package Various Components and their Interdependencies	83
15.	The XRF Method for Determining the Concentrations of Elements in a Sample is Described	88
16.	The GHARR-1 Facility's INAA Analytical Workflow (Osei et al 2021)	90
17.	The INAA Method for Determining the Elements in a Sample and their Concentrations is Described	91
18.	A Graph of Energy Calibration Showing the Regression Equation and the R ² Value	96
19.	Plot of Fitted Fe-standard for Sensitivity Calculation showing the Peak Area (Intensity)	102
20.	Am-241 K α -Sensitivity Curve	103
21.	X-ray Tube L α -Sensitivity Curve	105
22.	Comparison of K α and L α Sensitivity Curve	106
23.	The Control Chart that shows the Mean, Standard Deviation, Lower and Upper Control Limit for the Am-241 EDXRF System	109
24.	Fluorescence Spectrum of the various REEs in IAEA-Soil 7 with Am-241 EDXRF and thier Peak areas.	111
25.	Fluorescence Spectrum of the various REEs in IAEA-Soil 7 with Ag-tube EDXRF and thier Peak areas.	112
26.	Analysis of REEs in Sample Soil7 with INAA	113
27.	Fluorescence Spectrum of the various REEs in Sample DK6 with Ag-tube EDXRF and thier Peak areas.	117

28. Fluorescence Spectrum of the various REEs in Sample DK7 with Ag-tube EDXRF and thier Peak areas.	118
29. Fluorescence Spectrum of the various REEs in Sample DK8 with Ag-tube EDXRF and thier Peak areas.	119
30. Fluorescence Spectrum of the various REEs in Sample DK6 with Am-241 EDXRF and thier Peak areas.	120
31. Fluorescence Spectrum of the various REEs in Sample DK7 with Am-241 EDXRF and thier Peak areas.	121
32. Fluorescence Spectrum of the various REEs in Sample DK8 with Am-241 EDXRF and thier Peak areas.	122
33. The Graph that Shows INAA Analysis Results of REEs in Sample DK6	123
34. The Graph that Shows INAA Analysis Results of REEs in Sample DK7	124
35. The Graph that Shows INAA Analysis Results of REEs in Sample DK8.	124
36. Graph that Shows the Concentrations of the REE in Sample DK6	126
37. The Graph that Shows the Concentrations of the REE in Sample DK7	126
38. Graph that Shows the Concentrations of REE in Sample DK8	127
39. The graph shows a comparison between the results obtained for REEs with INAA and Am-241excitation-based EDXRF, the correlation and R ² values.	127

40. The graph shows a comparison between the results obtained for REEs with Ag anode X-ray tube spectrometer and Am-241 excited-based system, the Correlation Equation and the R^2 Value 129
41. The graph shows a comparison between the results obtained for REEs in sample DK6 using ICP-MS and the attached Am-241 excitation-based EDXRF system, the correlation equation and the R^2 value. 130



LIST OF ABBREVIATIONS

INAA	Instrumental Neutron Activation Analysis
Am-241	Americium-241 radioisotope
XRF	X-ray Fluorescence Analysis
EDXRF	Energy Dispersive X-ray Fluorescence
ICP-MS	Inductively Coupled Plasma- Mass Spectrometry
ICP-OES	Inductively Coupled Plasma- Optical Emission Spectrometry
AAS	Atomic Absorption Spectrometry
GF-AAS	Graphite Furnace Atomic Absorption Spectrometry
F-AAS	Flame Atomic Absorption Spectrometry
IUPAC	International Union of Pure and Applied Chemistry
USGS	United State Geological Survey
REE	Rare Earth Elements
HREE	Heavy Rare Earth Elements
LREE	Light Rare Earth Elements
LIBS	Laser-Induced Breakdown Spectroscopy
GD-MS	Glow Discharge Mass Spectrometry
MP-AES	Microwave Plasma Atomic Emission Spectrometry
ID-TIMS	Dilution Thermal Ionization Mass Spectrometry
SSMS	Spark Source Mass Spectrometry

CHAPTER ONE

INTRODUCTION

Background to the Study

Multiple analytical techniques have been developed in response to the requirement for rapid, sensitive, and non-destructive approaches throughout a multitude of scientific fields, trace elements could be found in a wide range of materials of interest (geological, and biological materials). Physical approaches, such as spectroscopic techniques, have largely replaced many of the previous classical methods for determining rare-earth elements (REEs) (Balaram, 2016). Using atomic absorption and plasma emission spectrometry, the simultaneous measurement of lanthanides at lower concentrations has recently been performed (Potts et al., 2015). These approaches were found to be insufficient, inductively coupled plasma spectrometry (ICP-MS) and instrumental neutron activation analysis (INAA) are the only exception (Kin et al., 1999). X-ray fluorescence (XRF) method is still the most versatile approach for concentrations less than or equal to 1 mg/g (Taam et al., 2013). The ability to measure each element without giving separation in columns is a major benefit of using XRF analysis in REEs.

The utilization of various main radiation sources, such as X-ray tubes, radioactive sources, or synchrotron light, has advanced these spectrometric approaches, particularly XRF (Taam et al., 2013). Furthermore, spectrometer development for diverse applications is an on-going research area (Sitko, 2009). Previous research conducted in the XRF unit of the Ghana Atomic Energy Commission (GAEC) laboratory used silver anode X-ray tube

benchtop X-ray spectrometer (EXP-1) to determine medium and moderate Z elements (Afrifa et al., 2013). Rare-earth elements, on the other hand, have received virtually little attention. To address this issue, a photon scattering experiment was set up with Am-241 excitation-based source and a silicon drift detector to acquire data for REEs with K-edges absorption near Am-241 exciting photon energies at 26.4 and 59.5 keV. A work has been done by Taam et al., (2013) using tube-based XRF to analysed REEs in laterite sample and only *La*, *Pr*, and *Nd*, could be identified (Taam et al., 2013). This thesis describes the modification of an existing EXP-1 with an Am-241 excitation-based system for REE studies. Scandium (^{21}Sc), yttrium (^{39}Y), and lanthanides are the three groups of elements that make up rare earth elements (REEs) (see Figure 1). There are seventeen (17) rare earth elements according to the International Union of Pure and Applied Chemistry (IUPAC).

The first, cerium group, includes lighter elements such as lanthanum (*La*), cerium (*Ce*), praseodymium (*Pr*), neodymium (*Nd*), samarium (*Sm*), and europium (*Eu*), whereas the second, yttrium group, includes heavier elements such as gadolinium (*Gd*), terbium (*Tb*), dysprosium (*Dy*), holmium (*Ho*), erbium (*Er*) (Savichev & Vodyanitskii, 2012). Because of its identical atomic and ionic radii, yttrium (^{39}Y) is commonly classified as a REEs (Henderson, 1984; Van Gosen et al., 2017). Scandium (^{21}Sc) is also occasionally included in the group of REEs since it resembles the elements in some ways. However, due to differences in other features induced by a reduced radius of its 3+ ion, the element's occurrence merits a special research (Henderson, 1984).

The cerium group comprises lighter elements like lanthanum (*La*), cerium (*Ce*), praseodymium (*Pr*), neodymium (*Nd*), samarium (*Sm*), and europium (*Eu*), whereas the yttrium group includes heavier elements like gadolinium (*Gd*), terbium (*Tb*), dysprosium (*Dy*), holmium (*Ho*), and erbium (*Yb*) (Savichev & Vodyanitskii, 2012). Yttrium (^{39}Y) is typically classed as a REE due to its same atomic and ionic radii (Henderson, 1984; Van Gosen et al., 2017). Scandium (^{21}Sc) is sometimes grouped with the REEs since it resembles the elements in some ways. However, because of changes in other properties caused by a smaller radius of its 3+ ion, the element's presence warrants further investigation (Henderson, 1984).

HEAVY Rare Earth Elements																					
LIGHT Rare Earth Elements																					
<small>by Geology.com</small>																					
H																	He				
Li	Be															B	C	N	O	F	Ne
Na	Mg															Al	Si	P	S	Cl	Ar
K	Ca	Sc	Ti	V	Cr	Mn	Fe	Co	Ni	Cu	Zn	Ga	Ge	As	Se	Br	Kr				
Rb	Sr	Y	Zr	Nb	Mo	Tc	Ru	Rh	Pd	Ag	Cd	In	Sn	Sb	Te	I	Xe				
Cs	Ba	La-Lu	Hf	Ta	W	Re	Os	Ir	Pt	Au	Hg	Tl	Pb	Bi	Po	At	Rn				
Fr	Ra	Ac-Lr	Rf	Db	Sg	Bh	Hs	Mt													
<small>Lanthanides</small>																					
La Ce Pr Nd Pm Sm Eu Gd Tb Dy Ho Er Tm Yb Lu																					
<small>Actinides</small>																					
Ac Th Pa U Np Pu Am Cm Bk Cf Es Fm Md No Lr																					

Figure 1: Light (marked Purple) and Heavy (marked Orange) Rare earth elements on the Periodic table

Rare earth elements can be found in a variety of high-tech devices as listed below. "REEs are necessary components of more than 200 products across a wide range of applications, especially high-tech consumer products, such as

cellular telephones, computer hard drives, electric and hybrid vehicles, and flat-screen monitors and televisions," according to the USGS news release "Going Critical." Electronic displays, navigation systems, lasers, radar and sonar systems are all critical defense tools. Even if the amount of REE utilized in a product does not make up a significant fraction of the product in terms of weight, value, or volume, the REE may be required for the device to function. REE magnets, for example, make only a small part of the total weight, yet desktop and laptop spindle motors and voice coils would not function without them (USGS, 2002). *Figure 2* depicts some of the REEs' applications in the United States (USGS, 2013).

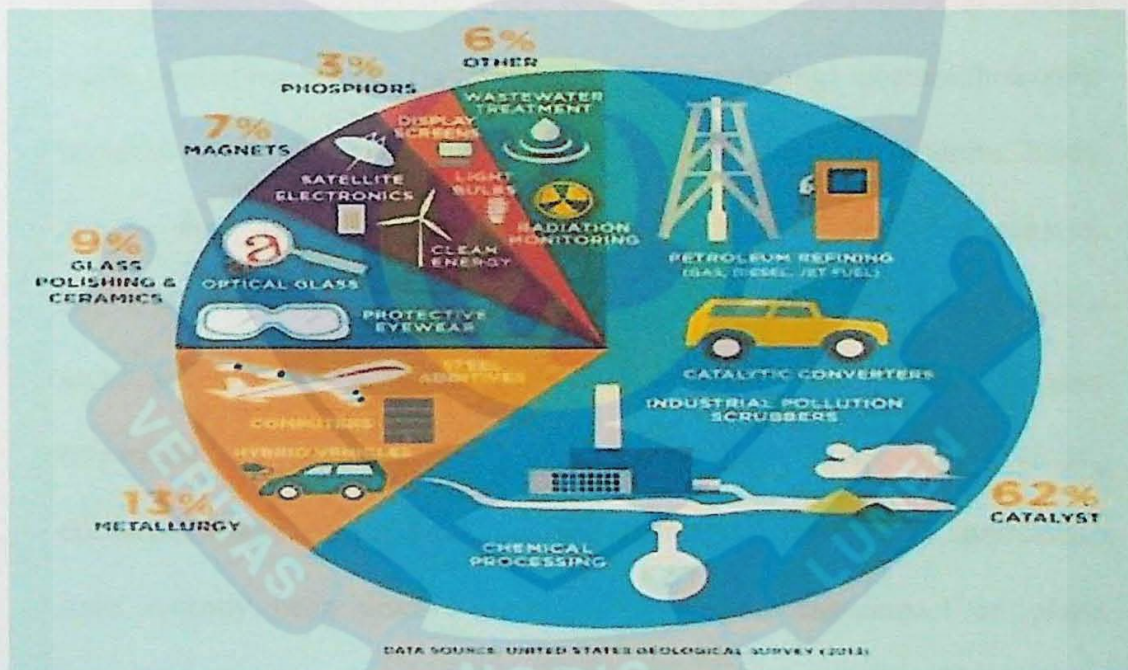


Figure 2: Usage of Rare earth Elements in U.S. (USGS, 2013)

REEs normally occur in geological environment in the form of carbonatites, alkaline complexes, rhylitic, granitic, hydrothermal, skarn, placers and heavy mineral sand; Radioactive Coastal Sands in Australia, Sri Lanka, Brasil, Malaysia, South Africa, United States of America (U.S.A), and India; Mineral deposits in the form of Bastinaesite, Allanite, Euxenite,

Microlite, Pyrochlore, Samarskite and Xenotime (Lusty & Walters, 2010). REEs are a useful indicator of a variety of geological processes, including magma production and fluid-rock interaction.

Although REEs enormous reactive capacity was well recognized, the lanthanides were long thought to be biologically inert elements (Savichev & Vodyanitskii, 2012). Later, it was shown that lanthanides have a strong interaction with calcium-binding proteins (Furie et al., 1973). In the biological nitrogen cycle, the medium's redox conditions are crucial, which is accelerated by lanthanides under oxidative conditions, nitrification is enhanced, whereas ammonification is accelerated under reductive conditions (Zhu et al., 2002). Some microorganisms (in particular, iron-reducing chemolithotrophic bacteria) favour lanthanide buildup and biogenic fractionation (Tsuruta, 2005). Among these is the *Gallionella ferruginea* bacteria, which could generate lanthanides in concentrations thousands of times higher than those found in rocks and millions of times higher than those found in soil-groundwater (Anderson & Pedersen, 2003). For Fe-Mn concretions, iron-oxidizing chemolithotrophic bacteria cause a large buildup of lanthanides. Lanthanides have recently been discovered to have a significant impact on plants (Perelomov, 2007). Agro-chemists discovered that a little dose of lanthanides has a favorable influence on the development of numerous plants (Rogan et al., 2006; Tyler, 2004; Wu & Guo, 1995). At the same time, this effect was not widespread, which was attributed to insufficient knowledge of soils. The most significant challenge appears to be identifying territories with negative lanthanide anomalies, where the most efficient administration of Lanthanide

fertilizers is required. The use of Lanthanide fertilizers to farmlands (where they are extensively used) would be challenging without knowing the amount of lanthanide in natural soils. Because lanthanides are difficult to identify, there is a scarcity of data on their presence in Ghana's soils. Physical approaches tend to be the most reliable for identifying lanthanides since they allow for the analysis of solid samples without the need for soil breakdown.

For spectrometric methods such as ICP-MS and atomic absorption spectroscopy (AAS), sample preparation is required (the process of converting a powder sample into a real solution). Normal soil decomposition techniques for determining lanthanide concentrations either do not allow for high analytic productivity at reasonable labour costs, or they result in significant analytic errors due to element loss during sample preparation for analysis (Karandashev et al., 2007). The most successful physical methods for estimating the total concentration of lanthanides in soils are neutron activation analysis (NAA), γ -spectrometry, and X-ray fluorescence (Savichev & Vodyanitskii, 2012). Instrumental and radiochemical neutron activation analyses with heat neutrons are the two types of analyses. The former entails spectrometric analysis of samples that have been activated in reactors following a series of exposure cycles (Kolesov, 1994). In the latter situation, the radionuclides in question are removed using radiochemical procedures, and their induced activity is then determined. Because the experimental approach is completely physical, its sensitivity is higher (the detection threshold for the majority of lanthanides is equal to the first mg/kg, with a 20 percent analytic error (Savichev & Vodyanitskii, 2012). However, it does not

allow the analysis of particular lanthanides, such as *Gd* (because of its low sensitivity) and *Dy* (because the nuclides produced by activation have a short lifespan) (Nikonov et al., 1999). The radiochemical approach is more sensitive, and it yields a longer list of elements, but it takes much longer time (Zaitsev et al., 1978) and cannot be regarded entirely physical. Direct sample analysis is also used in γ -spectrometry; after determining the content of natural nuclides, the total content is computed using isotope ratios. This approach could only be used to analyze lanthanides with a limited number of natural radionuclides. The detection threshold is measured in milligrams per kilogram (Kogan et al., 1991). The easiest and cheapest way of analysing heavy metals in soils is by the use of X-ray fluorescence analysis (Savichev & Sorokin, 2000). This approach, however, cannot be used to study all rare metals. The traditional XRF is obviously ineffective for determining the lanthanide content. When the X-ray fluorescence spectra of REE samples is excited with an X-ray beam, only lanthanide L-lines (far weaker than K-lines) would be activated (Savichev & Vodyanitskii, 2012); Strong K-lines from macro-elements would be placed on these weak L-lines., whose abundance is several orders larger than that of lanthanides. The radioisotope-based XRF looks to be the most convenient method for exciting lanthanide K-lines. The Am-241 radioisotope excitation source was employed, which has a 59.5 keV emission line energy and a radiation intensity of $100\ 100\ mCi$ ($1\ Ci = 3.7\ 10^{10}/s$). It is worth noting that no microelement lines superimpose on the K-lines of the lanthanides.

The simultaneous determination of lanthanides at lower concentrations has recently been done using ICP-MS in geological samples (Taam et al., 2013).

Statement of the Problem

Knowledge of REEs concentrations in different samples are very important in the mining industries for REE prospecting. However, the analysis of REEs concentrations is very difficult because of their strictly similar, physical and chemical properties. The most common analytical technique for the accurate analysis of REE is ICP-MS analytical technique (Abaka-Wood et al., 2019). This technique requires sophisticated separation technique, is expensive and not readily accessible in the country. Consequently, samples must be sent to foreign countries for analysis which makes analysis very expensive and relatively longer turn out time.

The other analytical techniques used for REE analysis are nuclear technique of INAA and EDXRF analysis. However, with the INAA facility available in Ghana. It takes considerable time to analyse REEs, even some of the REEs like Dy and Gd cannot be identified with INAA because of low sensitivity or short lifespan. On the other hand, EDXRF facility employs X-ray tube excitation system, with analysis of REE by X-ray tube-based XRF system is limited only to the L-lines of the lanthanides series due to system sensitivity. In addition, the accuracy of the results obtained are compromised, only lanthanide L-lines (far weaker than K-lines) would be activated. Strong K-lines from macro-elements would be placed on these weak L-lines, whose abundance is several orders larger than that of lanthanides. The evaluation of

the X-ray spectrum is made much more complex as a result of this. These problems may be circumvented through integrating Am-241 excitation-based system into the EXP-1 EDXRF spectrometer at GAEC.

The issue is most commonly linked to the use of an X-ray tube system in XRF.

Main Objective

The main objective of this study was to extend the analytical capabilities of an existing X-ray fluorescence spectrometer, in order to provide accurate, cost-effective analytical technique for REEs analysis; through the integration of Am-241 excitation-based system.

Specific Objectives

The specific objectives of this study were:

1. To reconfigure the EXP-1 (Ag anode X-ray tube XRF spectrometer) with the attachment of an Am-241 excitation-based system, to facilitate the identification of REEs;
2. To develop and validate a quantitative method of analysis for the reconfigured XRF spectrometer; and,
3. To compare the analytical results of selected geological samples using EXP-1 XRF, Am-241 based XRF, INAA and ICP-MS.

Significance of the Study

Am-241 offers the possibility of analysis of high Z-elements with their K-X-ray. EDXRF based on Am-241 is a cost-effective method for accurately identifying REEs and their concentration. It would make energy-dispersive

XRF available to all analytical laboratories in the low- and middle-income sub-region of Africa, where obtaining ICP-MS for rare earth element analysis may be challenging.

Delimitation

The scope of this research is to determine the amount of rare earth elements (high Z elements) with Am-241 excitation-based as a source in EDXRF to avoid peak interference. Peak interference could result in one broader peak instead of two individual peaks, making it impossible to detect individual elements. As it occurs between the L_{α} of REE and the K_{α} of transition metals. In this case, L_{α} of REE overlaps with K_{α} of the Transition metals. It makes it difficult to use the L-line to detect the REEs. Many research studies in EDXRF address the peak interference problem at the signal processing stage; however, using Am-241, characteristic peaks present in REE are well separated using their K_{α} line. The peak interference in REE is usually not a major concern using Am-241.

The goal of this study was to use Am-241 as a source in EDXRF to measure rare-earth elements (high Z elements) while avoiding peak interference. Peak interference could result in a single larger peak rather than two discrete peaks, making individual elements impossible to distinguish. It happens between REE and transition metals, for example. In this situation, REE's L_{α} and the Transition metals' K_{α} overlap. It makes detecting REEs using the L-line difficult. The peak interference problem is addressed in several EDXRF research studies at the signal processing stage; however,

utilizing Am-241, characteristic peaks present in REE are well separated using their K_α line. In REE, maximum interference occurs.

Limitations

Standards were used to create sensitivity calibration curves. These standards were chosen to span the range of energies to be determined in the study (33.44-54.06 kV). However, due to the unavailability of the other standards, energies of 33.44-44.47 kV were used in this study. As a result, energy above 44.47 kV cannot be accounted for. In this project, Annual Am-241 sources were used, which required precise determination of incident and take-off angles. The inability to precisely measure these angles may add error, resulting in the inability to acquire exact results, despite the accuracy of the results being good. Validation should have been done with a variety of certified reference materials (CRM), but due to lack of funding, only IAEA-SOIL 7 was used.

Organization of the Study

This thesis is divided into five sections. The thesis's introduction, highlights, and context are all covered in the first chapter. The research problem, the scope and objective of the study, the significance of the study, and the structure of the thesis are all stated. The second chapter discusses the literature that was used in this study as well as earlier work that was done using various methodologies for rare earth element analysis. The materials and method to be used in conducting this research are presented in Chapter 3. The fourth chapter delves into the findings, presentation and discussion of the

findings and their consequences. Inferences leading to conclusions are presented in Chapter 5.



CHAPTER TWO

LITERATURE REVIEW

Introduction

This chapter contains a comprehensive overview of the literature, on the subject of "rare earth elements and related analytical tools." Between sodium and uranium, with sensitivity in the part per million (ppm) range XRF analysis is a well-established multi-elemental analysis technique that could offer quantitative results on most elements in the periodic table's (Vekemans et al., 1995). There are an increasing number of applications that require precise X-ray line intensity measurements. Heavy element X-ray spectra measurements in the K-series, such as REE is gaining popularity. The Am-241 radioisotope has a 59.54 keV energy, which is enough to excite most elements with K-lines. The use of heavy element K-series X-ray lines rather than L-series radiation in EDXRF spectra should increase detection limits and minimize peak overlap. When using a radioisotope source for XRF, the needed equipment is mechanical, basic in design, and relatively less costly. These bring energy-dispersive XRF to practically every analytical facility in the low- and middle-income sub-region. The following is how this chapter is structured: REEs are defined as well as their applications, deposits, and the numerous analytical instruments used to analyse these elements. It also establishes the fundamental knowledge of XRF, including the physics of XRF spectra creation, X-ray interaction with matter, as well as XRF spectrometry. The XRF analysis help in evaluating X-ray spectrum without damaging the samples, the technique can be used to analyse the samples' chemical makeup.

Overview of Rare Earth Elements

The strategic and critical minerals recognized globally are REEs. Therefore, the easily accessible tool of REEs mining is of particular interest to many stakeholders. REEs are classified into two groups: light and heavy REEs. Light rare earth elements (LREE) include lanthanum (La), Cerium (Ce) Praseodymium (Pr), Neodymium (Nd) and Samarium (Sm). They are common and relatively easy to extract. Heavy REE (HREE), which contain yttrium and elements with Z-numbers ranging from 64 - 71 [europium (*Eu*), gadolinium (*Gd*), terbium (*Tb*), dysprosium (*Dy*), erbium (*Er*), thulium (*Th*), ytterbium (*Yb*), and lutetium (*Lu*)], are less abundant but important in demand and supply. Yttrium is the lightest REE but is regarded as HREE because it occurs with the other HREE as a result of similarity in outermost electronic configuration and atomic size to HREE. Scandium, yttrium, and fourteen (14 REEs) are the three groups of elements that make up REEs.

These metals possess similar chemical make-up, which means they are mostly found in geological deposits together. However, they have unique electrical and magnetic properties that allow them to be used in a small niche where no other technology can. The geological name for rocks that could dissolve in acid was rare in the 18th century, which is why these components are referred to as "Rare." (ISPI publication, 2021) It is "rare" because of their low concentration: they do not occur in pure form in nature but are always compounded with other elements (Gupta & Krishnamurthy, 1992; Hoatson et al., 2011; ishnamurthy & Gupta, 2015b). Individual abundances range from Ce, the most abundant at around 60 ppm, to Lu, with a concentration of less than 1.0 ppm, with the general crustal abundance of REEs being more than

silver and similar to copper and lead (USGS, 2002). Hybrid cars, wind turbines, fuel cells, electronics, medical and defense technology, and metallurgy/specialty alloys are examples of technological and industrial uses. REEs have been steadily gaining in relevance.

REE have multiple occurrences and liberal substitution with each other in the crystal lattice of a host mineral as a result of the similarities in ionic radii and oxidation state. Varying physical and chemical characteristics may be attributed to the marginal ionic radii differences which are responsible for either having heavy or light lanthanide (Long et al., 2012).

Technological Applications of Rare Earth Elements

There are no easy substitutes for the REE in most of their applications because of the properties they contribute to magnets, phosphors, and other specialized applications, largely facilitated by the properties of the 4f electrons that form the lanthanide series (Eggert, 2013; Hulle, 2022). REE forms a major constituent of many advanced materials and is critically important in high technology and green energy sectors. The applications of REE include; metallurgy, autocatalysis, glass additives, fluid cracking catalyst, battery alloy, polishing powder, magnets, and phosphors (Abaka-Wood et al., 2017). The most major REE application industry has been permanent magnets. Wind turbines use permanent magnet generators to convert wind energy into electricity, while electric vehicles, hybrid-electric vehicles, and plug-in hybrid-electric vehicles use motors to convert energy stored in the battery into mechanical power for propulsion (Lafleur et al., 2012; Zepf, 2013). REE is also utilized to improve the strength, malleability, corrosion and oxidation

resistance, and creep resistance of certain alloys. As catalysts, oxides of REE may be used in the cracking of crude petroleum and hydrogenation of ketones to form alcohol as well as olefins to form alkanes. The glass industry is one of the major REE consumers, using them for glass polishing and as additives by enhancing optical properties. Precision guide munitions (PGMs), smart bombs, sonars, and radars are just a few of the military applications that utilise REEs (Gibson & Parkinson, 2011; Lafleur et al., 2012; Robinson, 2011).

Mineralogy of Rare Earth Elements Ore Deposits

Rare earth elements generally occur in ore deposits as (a mixture) minerals commonly classified as carbonates, oxides, halides, phosphates, and silicates (Castor & Hedrick, 2006; Cordier & Hedrick, 2010; Lusty & Walters, 2010). They occur as trivalent cations with other elements such as copper, gold, uranium, phosphorous, and iron. REE are relatively abundant in the earth crust, but minable concentrations are generally less than other minerals and are usually made up of about 80-99% of La, Ce, Y, Pr, and Nd (Castor & Hedrick, 2006; Cordier & Hedrick, 2010; Lusty & Walters, 2010). They are mineralized in about 250 mineral phases, with gadolinite, xenotime, samarskite, euxenite, fergusonite, yttrotantalite, yttrotungstite, and yttrialite, predominantly containing HREE, whilst bastnasite, monazite, allanite, loparite, ancylite, parisite, cerite, britholite, florencite, and cerianite are noted to contain LREE (Abaka-Wood et al., 2019). Table 1 provides a summary of some selected REE minerals and their estimated rare earth oxide (REO) content. Bastnasite, monazite, xenotime, and loparite are considered principal commercial sources of REE minerals (Abaka-Wood et al., 2017; Jordens et al., 2013;

Krishnamurthy & Gupta, 2015). Bastnasite occurs as a primary mineral, while monazite is found in primary deposits of other ores and typically recovered as a by-product (HUMPHRIES, 2012; Lusty & Walters, 2010).

Table 1: Selected REE Containing Minerals, Formular and Approximate REO %

Mineral	Chemical Formula	REE Content %
Allanite	$(Ce, Ca, Y)_2(Al, Fe^{3+})_3(SiO_4)_3(OH)$	38
Bastenasite	$(Ce, La, Y)(CO_3)F$	75
Fergusonite	$(Ce, La, Nd)NbO_4$	53
Florencite	$CeAl_3(PO_4)_2(OH)_6$	32
Kainosite	$Ca_2(Y, Ce)_2Si_4O_{12}(CO_3) \cdot H_2O$	38
Loparite	$(Ce, La, Na, Ca, Sr)(Ti, Nb)O_3$	30
Monazite	$(Ce, La, Nd, Th)PO_4$	65
Parisite	$Ca, (Ce, La)_2(CO_3)_3F$	61
Synchysite	$Ca(Ce, La)(CO_3)_2F$	51
Xenotime	YpO_4	61

(Abaka-Wood et al., 2017)

Bastnasite

Bastnasite [(Ce, La, Y) CO₃F], a fluoro-carbonate mineral containing about 65-75 weight (wt). % REO is the most common LREE bearing mineral. It is an important mineral constituent for major REE deposits at Bayan Obo (Inner Mongolia, China), Mount Pass (California, USA), and Sichuan Manning, China (Krishnamurthy & Gupta, 2015; Li et al., 2014). Vein deposits, contact metamorphic zones, and pegmatites are all examples. (Krishnamurthy & Gupta, 2015). Bastnasite is a paramagnetic mineral and has

a specific gravity ranging 4.9-5.2, rendering it amenable for magnetic and multi-gravity beneficiation techniques. Most bastnasite deposits employ flotation using fatty acids and hydroxamate collectors (Jordens et al., 2013).

Monazite

Monazite [(Ce, La, Nd, Th) PO_4], a phosphate of REE and thorium (Th), is predominantly exploited for its LREE content. The mineral usually contains about 50-70% REO and 4-12% thorium content depending on the deposit. The REO components may constitute 20-30% Ce_2O_3 , 10-40% La_2O_3 and 10-15% Nd_2O_3 . In placer deposits, monazite is mostly found with heavy minerals as ilmenite, zircon, magnetite, and rutile (Dushyantha et al., 2020). It was the major REE-bearing mineral exploited on a commercial basis until 1965 when bastnasite emerged as a preferred option (Dushyantha et al., 2020; Krishnamurthy & Gupta, 2015).

Xenotime

Xenotime is mostly a yttrium phosphate YPO_4 mineral with a high percentage of REO (54–65 percent). It predominantly contains the HREE (Y), thorium, and uranium. It is often a component of heavy mineral sands, pegmatite, and igneous rocks. It is recovered as a minor mineral in many heavy mineral sand operations which are worked primarily for monazite in Brazil, India, South Africa, and Australia. The concentration of xenotime in a deposit can range from 0.5 percent to 5% of the monazite mineral (Krishnamurthy & Vissing-Jorgensen, 2015; Krishnamurthy & Gupta, 2015).

Global Rare Earth Resources and Production

Rare earth metals are primarily found all throughout the world, but only a few governments have set aside sufficient concentrations for mining. The United States Geological Survey (USGS) reports that, by 2020, 120 million metric tons of REE is expected that would have been generated globally. China has 44 million metric tons of REE deposits as of 2020, followed by Vietnam (22 million), Brazil (21 million), Russia (12 million), India (6.7 million), Australia (4.1 million), Greenland (1.5 million), and the United States (1.5 million). Other countries that account for the majority of the world's rare earth economic resources include Malaysia, South Africa, Sri Lanka, Thailand, and Tanzania. Reserves could also be used for other purposes. Over the last decade, new deposits have been identified in different countries, resulting in extensive exploratory activities to construct REE projects. New projects are being developed by China, Brazil, Canada, Australia, Turkey, Finland, Greenland, South Africa, Madagascar, India, Kyrgyzstan, Malawi, Mozambique, Namibia, Sweden, Tanzania, and Vietnam. China, the United States, the Commonwealth of Independent States, Australia, India, Brazil, and Malaysia have all produced REEs on a steady basis. Sri Lanka, Canada, Thailand, Madagascar, and South Africa, on the other hand, have contributed to world REE production on a sporadic basis (Krishnamurthy & Gupta, 2015; Li et al., 2014).

Li, are commonly found in alkaline magma (Balaram, 2019). As the magma rises, as a result of a complex combination of factors such as pressure, temperature, and the chemistry of the rocks it contacts, it experiences chemical changes. As a result of this complex interplay, a diverse spectrum of REE deposits has formed (Balaram, 2019; Ray & Shukla, 2004). Differentiated rocks such as nepheline syenites and trachytes, as well as peralkaline granites, act as hosts.

These complexes usually occur in continental within-plate tectonic settings associated with rifts, faults, or hotspot magmatism (Balaram, 2019).

Layered alkaline complexes, granitic stocks, and late-stage dikes, as well as trachytic volcanic and volcanoclastic deposits, all contain REE mineralization (Balaram, 2019; Dostal, 2017). Mountain Pass, California, Bayan Obo, China, and Ytterby, Sweden have all discovered REE deposits in alkaline igneous rocks. The world's largest REE deposit, China's Bayan Obo, is a high-grade, igneous-related carbonatite deposit that contributes 80% of the world's LREE (Verplanck, 2014). Carbonatites from Meghalaya's Sung Valley ultramafic–alkaline–carbonatite Complex, West Jaintia Hills, and East Khasi Hills districts were studied. Singh et al., (2014) found encouraging REE values. (HREE levels range from 60.98 to 81.92 g/g, whereas LREE levels are between 895.17 to 1264.85 g/g.) (Balaram, 2019). Economic considerations such as market pricing for both main and by-products, mining and processing costs, and metallurgical recovery tonnage grade distribution influence cut-off grades in mining metallurgical processes (Nieto & Zhang, 2013). As a result, determining the ore's cut-off grade may be difficult. The Saranu carbonatite

deposit in Rajasthan is a large carbonatite deposit in India with high REE concentrations. The deposit is made up of carbonatite dikes with a diameter of 10 cm and a concentration of 5.5 percent REO (rare earth oxides). LREE minerals such as bastnäsite, parisite, and synchysite have been discovered in the Amba Dongar carbonatite complex in Gujarat (Doroshkevich et al., 2009). The discovery of carbonatite plugs, sills, and dykes was made by (Bhushan & Kumar, 2013).

According to a recent analysis of these carbonatites and the host ijolite plug, the creation of this deposit was linked to mantle 'hot spot' activity coeval with Deccan volcanism (Singh, 2020). Using geological mapping and grid channel geochemical sampling methods, Bhushan and Kumar discovered carbonatite plugs, sills, and dykes hosting REE deposits at Kamthai (very close to Saranu deposit), Barmer district, Rajasthan, India, with a possible REE resource of 4.91 Mt and approximated up to 84 m depth with the highest value of LREE of 17.31 percent and the mean grade of 3.33 percent (Balaram, 2019).

The REE and Y potentials of Neoproterozoic peralkaline Siwana granite from the Malani igneous group in Rajasthan's Barmer area were investigated by (Bhushan & Somani, 2019). They also categorized the REE minerals in the suite, which comprised well-exposed and outcrops, and determined that the site is suitable for open-pit mining. The Malani igneous series' Neoproterozoic Peralkaline Siwana granite has an overall REE concentration of 2.0 to 2.5 percent. Mineralogy, leachability, and separation during the metallurgical test will all have an impact on the economic viability.

Because HREE is so expensive, even extracting 50% of the ore will be profitable. The cost of opencast mining will be minimal because the area is extremely exposed and the outcrops have significant relief (Balaram, 2019; Bhushan & Somani, 2019).

Residual Deposits

Extreme weathering of igneous rocks produces pegmatite and iron-oxide copper-gold deposits as a result of deep weathering. Carbonatite and peralkaline intrusive deep weathering have the potential to yield concentrated REE mineral residual deposits. One example is REE-laterite, which is generated by the weathering of tin granite in south China. Only China is known to have ion-adsorption ores in this group. The climate in a large region of North East India is ideal for the formation of a thick lateritic profile, making this kind of REE deposit attractive (Singh et al., 2014). Bauxite, the principal source of aluminum produced by the weathering of numerous types of aluminosilicate source rocks, is also a substantial source of REE, according to Valetton (Valetton, 1972). The solid residue created in the Bayer process for aluminum production is known as bauxite residue (red mud). This red mud, as well as some other bauxite deposits, might be prospective REE sources (Vind et al., 2018).

Placer Deposits with Heavy Mineral

Placer deposits may contain REE-bearing minerals, which could be valuable. The majority of REE-rich placer deposits are Tertiary or Quaternary deposits generated from granitic or high-grade metamorphic rocks as source materials; nevertheless, REE resources have been detected in Precambrian

paleo placer deposits. In placer deposits, monazite [(Ce, Th)PO₄], a common REE-bearing accessory mineral found in igneous, metamorphic, and sedimentary rocks, can be concentrated alongside other heavy minerals. Monazite is a notable REE mineral since the majority of its ore deposits are economically viable REE resources. Monazite contains cerium, but light and heavy REEs including Tb, Dy, and Gd are scarce and less concentrated. Monazite is the primary source of light REE in India. As a result, HREE in India is heavily reliant on imports. Tin-rich river placers in Malaysia, paleo-placers in the Witwatersrand, South Africa; Elliot Lake, Ontario; and beach sand deposits in Kerala, Andhra Pradesh, Tamil Nadu, and Odisha, India are just a few examples of REE placer deposits. Although monazite is currently only processed in India, China, and Malaysia, Russia and Brazil are gaining more interest (Palaparthy et al., 2017) conducted a comprehensive research to analyze radioelement and REE concentrations in beach placer deposits along the eastern coast of Andhra Pradesh, India, in order to better understand the economic potential of beach placer deposits. Monazite is a limited 'atomic' mineral in India due to low thorium and uranium concentrations.

Rare-Earth Elements in Coal Deposit

As the gap between worldwide REE demand and availability widens, the quest for alternative resources has become increasingly crucial, especially for countries that rely heavily on imports. Coal fly ash, often thought to be trash, is now recognized as a viable source of a variety of elements, including REE (Franus et al., 2015). Because the REE concentrations in many coals and coal ashes are comparable to or higher than those in typical REE ores, this is

the case. REE values in coal samples from Iran's Mazino Coal Mine ranged from 16.4 to 184 g/g, with an average of 88.9 g/g (Pazand, 2015). In comparison to world average coal, REE levels were found to be much lower in Indian coal samples from the North Eastern Region (NER). Coal ash, on the other hand, has a global REE value of 404 g/g (Dai et al., 2016). In the literature, even higher REE (including Y) values of up to 1358 g/g have been reported (Hower et al., 2016). This has the potential to minimize our reliance on others for these important ingredients while also creating new sectors in locations where coal has historically played a significant role in the economy. The concept of recovering rare earth elements from abundant coal and coal ash is an exciting new research topic that offers a significant shift in the coal paradigm (Franus et al., 2015).

Rare Earth Elements in Sediments of Continental Shelf and Ocean Bottom

Mineral resources on the continental shelf are comparable to those on neighbouring land. Minerals eroded from the soil may concentrate as placer deposits along the coast, and comparable placer deposits may exist deeper beneath the sea. Massive volumes of phosphorite (phosphate rock or rock phosphate), a non-detrital sedimentary rock that is also a major source of REE, can be found on continental shelves. According to recent investigations of marine phosphorite deposits, the phosphorites contain significant levels of REE (Dar & Saman, 2014; Li & Schieber, 2020; Mazumder et al., 1999; Nath & Sharma, 2000). Unlike manganese nodules and cobalt crusts, phosphorite deposits develop as chemical precipitates on continental shelves at much

higher depths in seas (Balaram, 2019). When phosphate-rich fluids are heated, they lose their insolubility and deposit. REE is abundant in the francolite mineral phase of phosphorites, which replaces Calcium in the francolite lattice (Jarvis et al., 1994). The amount of REE in these rocks varies greatly depending on the kind and provenance of the rock. However, certain phosphorite deposits contain up to 2000 g/g (Balaram, 2019). Embo (Emsbo et al., 2015) determined that phosphorite deposits are more REE-rich than most typical REE resources after analyzing chemical data from 23 sedimentary phosphate deposits (phosphorites) with REE up to 18,000 g/g and HREE up to 7000 g/g. Current discoveries (Balaram, 2019; Hein et al., 2013; Kato et al., 2011; Zhong et al., 2018) imply that substantial REE deposits can be found in ocean bottom sediments.

Polymetallic nodules, ferromanganese crusts (cobalt crusts), and deep-sea muds are the three primary forms of REE deposits found in deep oceans. Polymetallic nodule deposits grow on sediment-covered abyssal plains (at depths of 4500–6000 m in water) and are found in surficial seabed sediments in abyssal plain muds, mainly in the Pacific and Indian Oceans (Nath et al., 1994). Cobalt crust can be found on seamounts, ridges, and highlands on hard-rock substrates all over the world, and as a surface encrustation on seamounts and rock outcrops in all seas, having the richest deposits in the western Pacific (Paropkari et al., 2010; Zeng et al., 2015). The proportions of influxes of genetically varied components: hydrogenic, biogenic, hydrothermal, volcanogenic, and lithogenic elements (Banakar & Borole, 1991; Nath et al., 1992). Cobalt crust is the more important of the two kinds in terms of REE.

REE enrichment is mostly caused by the sorption of ferromanganese oxides and clay minerals in crusts and nodules. They form when cold ambient bottom fluids at depths of 1000–3000 meters precipitate (Balaram, 2019). Large concentrations of strategically and economically important metals (e.g., *Co, Ti, Ce, Zr, Ni, Pt, Mo, Te, Cu, W*) (Savichev & Vodyanitskii, 2012), as well as unusually high quantities of REE, are found in the crusts, which form at a sluggish rate of around 1–7 mm/Ma. The two types of ferromanganese crusts are hydrothermal (generally episodic) and hydrogenous (normally continuous). REE patterns can aid in identifying the two types of deposits (Balaram, 2019). The level of REE in these ocean bottom sediments (REE 2511 g/g) is very high. Ce enrichment is exceptionally high, accounting for more than 60% of total REE content (Zhong et al., 2018). Over millions of years, hot plumes from hydrothermal vents extracted these elements from seawater and deposited them on ocean floors (Savichev & Vodyanitskii, 2012). Balaram et al., (2019), looked studied the seamount crust of the Afanasy Nikitin Seamount (ANS) in the Indian Ocean to prove that the bottom sediments of the Indian Ocean also contain massive concentrations of these valuable metals (Savichev & Vodyanitskii, 2012). Using multi-beam swath bathymetry, the research was then broadened to include detailed geochemical and bathymetric examinations of cobalt crust of seamount (Krishna et al., 2014).

The third main source of REE is deep-sea muck, which is abundant on the ocean floor (Yasukawa et al., 2015). A fresh and comprehensive data collection of their bulk chemical compositions, including REE, major, minor, and trace elements, was developed using 1338 deep-sea sand samples

collected from 19 Deep Sea Drilling Project/Ocean Drilling Program locales in the Indian Ocean. The high REE-rich mud and Fe–Mn nodule formations, which frequently overlap, have significant resource potential. Minamitorishima Island, Japan, developed a successful mineral processing approach with a hydro cyclone separator to selectively remove biogenic calcium phosphate grains with high REE concentration (up to 22,000 g/g) when reporting deep-sea mud from the western North Pacific Ocean. (Takaya et al., 2018). According to the experts, this new REE resource could be used in the near future. In some spots, the Pacific mud deposit has 100–1000 times the world's current known terrestrial REE reserves of 130 million tons. According to several analyses, undersea REE reserves are far more promising than on-land REE resources. A 2.3-kilometer-square of metal-rich muck may supply most of the world's REE needs for a year (Kato et al., 2011). They showed that REE and Y can be easily recovered from mud using simple acid leaching, suggesting that deep-sea muck could be a source for these elements (Balaram, 2019). The economic viability of deep-sea mining, however, is unclear given the current level of ocean mining technology (Balaram, 2019). Deep-sea mining could be a viable long-term solution if environmental and economic problems are addressed.

Extraterrestrial Rare Earth Elements Resources

According to recent analyses (McLeod & Krekeler, 2017), the world's accessible REE resources will persist for no more than 2500 years. Exploration of extra-terrestrial REE resources is unavoidable, based on present demand, mining operations, and technologies, as well as a predicted growth in

population and technological needs. Our Solar System's Moon, Mars, and other surrounding objects may have one or more alien REE deposits that will be utilised one day (Haque et al., 2014; Savichev & Vodyanitskii, 2012).

Rare Earth Elements in Agriculture

Rare Earth Elements are also used as fertilizer in agriculture to improve crop development and yield, resulting in an increase in REE concentrations in the soil (Tyler, 2004). In general, macronutrients (*Ca*, *Mg*, *N*, *P*, and *S*), micronutrients (such as *Fe* and *Si*), and rare earth elements are found in mineral fertilizers (phosphate fertilizers) and soil conditioners. REE can also be found in soils as a result of local geological sources (Liu et al., 1993). To enhance productivity and quality, REE-containing micro-fertilizers are applied directly to plants on a wide scale in China (Balaram, 2019; Diatloff et al., 1995; Pang et al., 2002). REE accumulated concentrations have been reported to be extremely low in general. Plant accumulation capacity, on the other hand, is influenced by a variety of elements such as plant type, growing conditions, and REE content in the substrate soil or rock, among others (Fu et al., 2001). Rice got greater readings than maize, indicating that rice is more prone to REE buildup (Fu et al., 2001). Environmentalists are concerned that, as a result of REE abuse in agriculture, these elements may enter the food chain through plant absorption, posing a health risk to humans. REE concentrations in cereal grains are rather modest, according to some research (Redling, 2006), and there is no considerable build-up due to REE fertilization. As a result, cereals and products made from them, such as wheat flour, are considered safe. According to (Thomas et al., 2014), nations with

high natural occurrence levels of REE in their soils, like Russia and Nigeria, will suffer larger environmental hazards as a result of increased REE input. Careful monitoring may be required in areas where phosphate-based fertilizers (mined from monazite deposits) are commonly employed.

Rare Earth Elements in Medicine

REEs could be used in a variety of therapeutic and diagnostic applications in modern medicine due to their unique features, such as radiation emission or magnetism. Only a few key uses of REE in medicine exist now, but many more are on the way. REE has antibacterial and antifungal effects comparable to copper ions, according to research (Wakabayashi et al., 2016; Zhang et al., 2000; Zhong et al., 2018), and these elements are now employed in pharmaceuticals. Although gadolinium has been used as a contrast agent in MRI studies in a chelated form (Raju et al., 2010), recent study has discovered direct evidence of gadolinium buildup in brain tissues, which could be dangerous to neurons (Gulani et al., 2017; McDonald et al., 2015). Because they stop fungal spores from growing and germinating, REE can be used as a nematicide, impacting a wide spectrum of species (Balaram, 2019). When pharmaceutical samples are tested by ICP-MS for inorganic impurities, it is determined that they contain large amounts of LREE (*La* 25 g/g; *Ce* 7 g/g; *Gd* 8 g/g) (Balaram, 2016). The ramifications of having such a broad range of REE concentrations in drugs are unknown at this time (Balaram, 2019). Residents in mining areas have been exposed to REE, which has been related to a variety of health problems, including occupational toxicity, water contamination, and agricultural damage. According to an increasing amount of

research (Rim, 2016), REE-related antioxidant properties have been demonstrated in the therapy of a variety of diseases. These elements' therapeutic applications are now being found at a rapid rate, and emerging technologies like nanotechnology could be applied to maximize their utilization in the future.

Analytical Techniques used in Mining Rare-Earth Elements

Chemical analysis of REE in geological, industrial, and environmental materials is required for geochemical exploration investigations, mining, extraction, quality checks of both raw materials and end products in the industry, and environmental monitoring. REE are difficult to distinguish due to their physical and chemical similarities. This is especially true if, due to various interferences and coincidences, a specific element among them must be identified in the mix of the other REE. Traditional methods for determining REE in geological materials at their crustal abundance levels, such as flame atomic absorption spectrometry (F-AAS), gravimetry, titrimetry, spectrophotometry, and graphite furnace atomic absorption spectrometry (GF-AAS), were previously extremely difficult and time-consuming (Onishi et al., 1962; Saxena, 1970; Wengert et al., 1952). However, these jobs have grown much easier now that powerful instrumental analytical tools are available. Because of its multi-element capabilities, high sensitivity, wide linear dynamic range, low interferences, ease of operation, and accuracy, instrumented neutron activation analysis (INAA) and ICP-MS, particularly HR-ICP-MS, are frequently used for REE detection in a variety of materials. In such investigations, X-ray fluorescence spectrometry (XRF), inductively coupled

plasma optical emission spectrometry (ICP-OES), glow discharge mass spectrometry (GD-MS), laser-induced breakdown spectroscopy (LIBS), and the recently introduced microwave plasma atomic emission spectrometry (MP-AES) have all proven to be extremely useful. Although techniques such as isotope dilution thermal ionization mass spectrometry (ID-TIMS) and spark source mass spectrometry (SSMS) have been used in the past to determine REE, their applicability is currently limited due to the need for time-consuming sample preparation methods and high costs (Jochum et al., 1988; Klinkhammer et al., 1994). Because REE are widely used in electronics and sustainable energy systems, the search for economically viable REE concentrations is ongoing. Many investigations of REE concentrations in coal and coal ash have been published, indicating that they are potentially cost-effective sources of REE (Eskenazy, 1987; Hower et al., 2013; Qi et al., 2007). Because REE are found in low concentrations in most geological materials (Gromet et al., 1984; Haskin & Haskin, 1966; Taylor & McLennan, 1985), it is necessary to optimize sample preparation and testing methods in order to reduce uncertainty and maximize recovery.

Inductively Coupled Plasma-Mass Spectrometry (ICP-MS) and Instrumental Neutron Activation Analyses are two of the most used methods for analyzing REE in geologic materials (INAA). While INAA has the advantage of not requiring sample digestion prior to analysis, it takes longer to complete and has greater detection limits than ICP-MS (Golightly & Simon, 1989; Palmer & Baedeker, 1989). Except for an enrichment of Sm in INAA data, a study comparing REE concentrations by ICP-MS and INAA found that

the two procedures produced comparable results (Cruse et al., 2000). The most widely used analytical approach for measuring REE is ICP-MS following solid sample digestion (Potts et al., 2015). REE in geological samples has also been measured using pre-treatment, correction standards, and other techniques like as Raman and X-ray fluorescence (Bayon et al., 2009; Lee et al., 2000; Makreski et al., 2011; Raut et al., 2003; Zawisza et al., 2011). Although ICP-MS has been shown to be a reliable and repeatable method for measuring REE, appropriate preparation of samples for ICP-MS is critical for accurate results. A comparison of REE in geological reference materials using INAA and ICP-MS revealed that ICP-MS was more accurate for light REE (La-Gd) than heavy REE (Tb-Lu), but INAA provided results that were closer to published values, implying that sample preparation for ICP-MS was the cause (Kin et al., 1999). The examination of REE in geologic samples digested using a 4-acid approach, for example, yielded results that were lower than those obtained using neutron activation analyses (NAA), owing to insufficient digestion of very insoluble mineral phases (Totland et al., 1992; Tsai & Yeh, 1997).

However, in terms of analytical repeatability, the MC-ICP-MS (multi-collector inductively coupled plasma mass spectrometer) outperforms quadrupole ICP-MS or ID-TIMS method for REE measurement in geological materials. Precisions of less than 0.4 percent can be achieved for all REEs (Baker et al., 2002). The next section examines some of the most essential analytical techniques and how they can be applied to REE analysis in a variety of situations.

Laser-Induced Breakdown Spectroscopy (LIBS)

LIBS is a sort of emission spectroscopy that makes use of a plasma produced by a laser to ablate and excite the atoms in a sample, which can be solid or liquid (Balaram, 2017; Cremers & Radziemski, 2013). The unique optical emission spectra of elemental elements can be directly fingerprinted by laser ablation of liquid or solids (Balaram, 2019). Detection limits for most REEs in common applications range from 10 g/g to 100 g/g (Balaram, 2019), Precisions range from 3% to 5%, and for homogeneous materials, precisions are generally better than 2%. (Cremers & Radziemski, 2006). Various manufacturers provide both desktop and portable variants. LIBS technology has a number of advantages over other approaches, including the ability to take measurements quickly, the ability to utilize it in the field, the lack of sample preparation, and the consumption of small amounts of sample. The most significant advantage of LIBS is that it can quickly identify a wide range of metals and non-metals, including REE (Bhatt et al., 2018). This capability is notably beneficial for REE component recovery and processing procedures. LIBS-based solid-state measurements are commonly comparable to XRF in terms of precision. It can also instantly characterize solid objects. The applicability of LIBS for field analysis is comparable to that of XRF in terms of overall accuracy (Takahashi and Thornton, 2017)

Instrumental Neutron Activation Analysis (INAA)

INAA is a very sensitive and versatile analytical technique for determining major, minor, and trace element concentrations in a range of media. A small sample is subjected to a neutron flux in a nuclear reactor.

Stable nuclei absorb neutrons and decay into unstable radioactive isotopes, which produce particles or, more significantly, gamma rays that are unique to the elements from which they were produced. The energy of the emitted gamma rays identifies the nuclide, and the intensity of the radiation can be used to estimate its abundance. Quantitative measurements are usually performed with semiconductor radiation detectors. When the strength of these gamma rays is compared to that of a standard, the concentrations of the individual nuclides may be quantified. Because the chemical and physical structure of the material has little effect on nuclear reactions and decay processes during and after irradiation, this technology is exceedingly popular. Several researchers have used the INAA method to assess REE concentrations in a range of earth and environmental materials at extremely low levels (Alharbi & El-Taher, 2016; Baidya et al., 1999; Balaram, 2019; Bounouira et al., 2007). INAA investigated the geochemical behaviour of REE in beach sands from Tamil Nadu, India (Ravisankar et al., 2006). The data gathered by the author utilizing other popular analytical techniques such as ICP-MS and ICP time-of-flight MS (ICP-TOF-MS) is compared to the REE values determined by INAA for Ocean bed polymetallic nodule reference sample (2388) from the Indian Ocean (Pandey, 1992). Because certified data for a variety of elements, including REE, is not currently available for this unique Indian reference material, this information would be useful in the future for delivering certified values for all REEs. INAA has some flaws, despite being a sensitive and multi-element technique. To account for the emitted X-rays that undergo self-attenuation in the sample under the same counting conditions, INAA requires matrix matching reference materials for calibration. As a

result, synthetic standards made from REE combinations are not suitable unless the matrix matches that of the sample. INAA measured REE concentrations (g/g) in ferromanganese crust (cobalt crust) samples taken from the ANS (Afanasy Nikitin Seamount) in the Eastern Equatorial Indian Ocean, following the procedure outlined by (Balaram, 2019; Figuelredo & Marques, 1989). The Nod-A-1 and Nod-P-1 worldwide polymetallic nodule reference samples were used to calibrate the system. Because INAA is such a sensitive technology, it is highly useful for determining REE in geological and environmental materials. Despite these benefits, INAA is not a widely used analytical technique since it takes time, is not self-contained, requires the presence of a reactor, and requires longer cooling times for specific elements (Balaram, 2019)

Inductively Coupled Plasma Optical Emission Spectrometry (ICP OES)

ICP-OES is a multi-element analytical technique for determining distinct elements in a wide range of materials at major, minor, and trace concentration levels. At high temperatures, a liquid sample is converted into an aerosol and transferred to an inductively coupled plasma. In the plasma, the sample undergoes dissolution, vaporization, atomization, and ionization. The atoms and ions take energy from the plasma, which causes electrons to jump from one energy level to the next. When electrons return to a ground state, light with wavelengths unique to each element is released. To determine the relative elemental levels in an unknown sample, the intensity of measured emissions is compared to the intensity of known-concentration reference materials (Greenfield et al., 1964; Wendt & Fassel, 1965). The ICP-OES could

measure up to 60 elements simultaneously with great sensitivity and a very large linear dynamic range, which is possibly its most impressive feature (Balaram, 1995). After selecting the most acceptable spectra lines, determined low concentrations of the fourteen naturally occurring lanthanides directly by ICP-OES (Bentlin and Pozebon, 2010). However, due to several spectral interferences encountered during the determination of REE in geological materials, it is necessary to use a separation and pre-concentration procedure before using ICP-OES (Jarvis et al., 1994). Who used ICP-OES to evaluate REE and Y in 37 international rock reference materials after using cationic-exchange chromatography for secession and pre-concentration, accompanied by a conventional rock solubilisation method. Because of the line-rich spectra emitted by REE, it is difficult to reliably quantify REE and other trace elements in the presence of high REE concentrations in a sample using ICP-OES. The analysis of cerium oxide, gadolinium oxide, and NdFeB magnetic materials matrices was done using high-resolution ICP-OES to get very high-quality results (Chausseau et al., 2014) . Because of the spectral complexity and low quantities of REE in various types of rocks, ion exchange separation is required after sample digestion before ICP-OES analysis, making this approach less productive (Amaral et al., 2017; Balaram, 1995; Jarvis & Jarvis, 1985; Walsh et al., 1981) employed ICP-OES to collect data on geochemical formation history, plant nutrition status, the need for supplementation, and possible contamination in geological and agricultural materials by measuring emission signals in radial and dual viewing modes.

Microwave Plasma Atomic Emission Spectrometry (MP-AES)

In 2011, the MP-AES, new commercial equipment that represents yet another method of analysis, was developed, for REE measurements. It appears to be a viable alternative to ICP-OES. According to reports, The MP-AES system employs a relatively new type of plasma torch that generates high-temperature microwave plasma using nitrogen gas (Hammer, 2008). During the previous years, the applicability of MP-AES has been proven in a wide range of geological and environmental matrices, including industrial effluents, water, sediments, soils, rocks, and ores, with detection limits in the $\mu\text{g/g}$ range for many REE (Balaram et al., 2013; Helmeczi et al., 2016; Kamala et al., 2014; Sreenivasulu et al., 2017; Vysetti et al., 2014). The unique approach for quick digestion of REE ores and determined REE both by MP-AES and dynamic reaction cell-ICP-MS was developed (Helmeczi et al., 2016). The REE values obtained by MP-AES were identical to those obtained by ICP-MS (Tupaz et al., 2020). The MP-AES was employed to determine scandium in a laterite sample, and the results were comparable to ICP-MS (Tupaz et al., 2020). MP-AES is currently a feasible analytical strategy for inorganic contents in a variety of geological and environmental materials due to its multiple clear advantages over techniques like F-AAS and ICP-OES. Because MP-AES and classic ICP-OES use identical sample introduction procedures, sample introduction and sample pre-concentration strategies developed for ICP-OES should be equally resilient for MP-AES, making MP-AES a viable alternative approach in the future.

Glow Discharge Mass Spectrometry

The glow discharge mass spectrometry (GD-MS), which works like mass spectrometric techniques, it is well established analytical tool for the analysis of major, minor, trace, and ultra-trace compositions in solid materials, including geological, metallurgical, and semi-conductor materials, over a wide dynamic range (ng/g to 100 percent), with a variety of applications spanning several disciplines (Becker & Dietze, 2003; King et al., 1995). In 1985, the first commercial GD-MS was created, the magnetic sector model VG 9000 ("Thermo Elemental", Winsford, UK). This technique is useful for analysing REEs because it has lower detection limits for various REEs to sub- $\mu\text{g/g}$ levels.

X-ray Fluorescence Spectrometry (ED-XRF)

X-ray fluorescence spectrometry (XRF) is a suitable approach for trace element research at the g/g level, notwithstanding the technique's insensitivity to REE in the current setting (X-ray tube system). However, as a traditional analytical technique for measuring REEs, XRF has distinct advantages over other methods in terms of accuracy, time, and cost. Its only drawback is that it has a low sensitivity to REEs when employed in an X-ray tube system arrangement. There are two forms of XRF: EDXRF (energy-dispersive X-ray fluorescence spectrometry) and WDXRF (Wavelength-dispersive X-ray fluorescence spectrometry) (Potts & Webb, 1992). With success, the WD-XRF and ED-XRF procedures were utilized to determine REE in environmental and geological samples that have been pre-separated from other constituents. Due to the higher detection limits provided with this methodology for REE, many

analysis techniques require extraction and pre-concentration phases for precise estimation (De Vito et al., 2000). For example, after all REEs were separated from other constituents using an ion-exchange process (Juras et al., 1987) employed XRF to assess REE in geological samples ranging in composition from ultramafic rocks to rhyolite. A study of the uses of XRF analysis in the Chinese rare earth mining was presented (Wu and Guo, 1995). Among the applications were REE analysis in ores and soil concentrates, compounds, metals, alloys, functional materials, and rapid and online analysis in the separation process (Smoliński et al., 2016). In recent times, geochemical exploration studies have effectively used portable XRF (ED-XRF form) to measure REE such as *La*, *Ce*, *Pr*, and *Nd*, and also REE pathfinders such as *Y*, *Th*, and *Nb* (Balaram, 2017). These devices are very valuable in the field since they enable quick decisions in prospecting, ore grade/process control, and environmental sustainability analyses. Even though identifying trace impurities of rare earth elements in Ghanaian mines is becoming increasingly important for the categorization of mine materials, there are few fast and sensitive methods for doing so. Rare earth elements (REEs) are a useful indicator of a variety of geological processes, including magma production and fluid-rock interaction. There are an increasing number of applications that require precise X-ray line intensity measurements. Measurements of heavy elements' K-series X-ray spectra, such as rare earth elements are also gaining popularity. The energy emitted by the Am-241 source is 59.54 keV, which may excite the K-lines of most heavy elements. The use of heavy element K-series X-ray lines instead of L-series radiation in EDXRF spectra should increase detection limits and eliminate peak overlap.

Principle of X-ray Fluorescence

The principle that each element produces secondary fluorescent X-rays when exposed to appropriate X-ray energy and the area under the X-ray spectra (intensity) could be used to estimate the concentration of an element in the sample could be used to analyse rare earth elements. Wilhelm Conrad Röntgen discovered X-rays in 1895 while examining cathode rays in high-voltage, gaseous discharge tubes, and they were given the letter 'X' due to the unknown nature of radiation (Van Grieken & Markowicz, 2001). For his discovery of X-rays, Röntgen was awarded the Nobel Prize in 1901. There were various attempts to employ this radiation for the characterization of matter within a short period after its discovery (Haschke, 2014b). Henry Gwyn Jeffreys Moseley developed a particular link between the wavelength of characteristic X-ray photons and an atomic number of the exciting element in 1913, which paved the way for the use of X-rays for element characterization (Jenkins, 2012). The X-ray spectrum ranges from 0.010 nm (100 eV) to 10 nm (100 keV). The wavelength of X-ray photons is inversely proportional to their quantum energies, and thus on par with the binding energies of atoms' inner shell electrons (Gauglitz & Moore, 2014a; Vogel-Mikuš et al., 2012). X-rays were first used to excite a sample in 1925, but it was not until 1948 that the technology became feasible with the invention of the first commercial X-ray spectrometer (Tsuji et al., 2005). This spectrometer monitored the wavelength of one element at a time and was a wavelength dispersive X-ray spectrometer (WDXRF). Later, multi-element analysis was made possible by the discovery of energy dispersive X-ray spectrometers (EDXRF).

Interaction of X-rays with Matter

When an X-ray beam interacts with a substance, it is attenuated, resulting in a reduction in the incident beam's intensity (Jenkins, 1995). As shown in Figure 3, when an X-ray beam travels through a sample, some photons may be dispersed or absorbed inside the material (Storm & Israel, 1970).

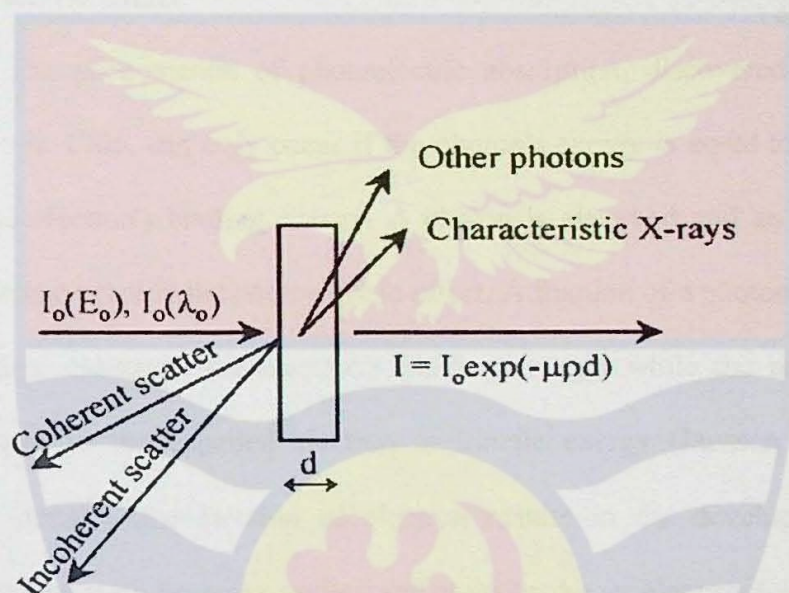


Figure 3: Interaction of X-ray with matter (Jenkins, 1995)

Scattering

The interaction of radiation and matter can cause the direction of X-rays to alter. If the photon's energy remains constant, the scattering is known as elastic or Rayleigh scattering. When X-ray photons collide with weakly bound electrons, scattering occurs. Inelastic or Compton scattering occurs when photons lose some energy (Beckhoff et al., 2007; Theodorakou & Farquharson, 2008). The interaction of a photon with a free electron at rest is known as Compton scattering (Van Grieken & Markowicz, 2001). The total scattering cross-section σ_t could be represented as the sum of two components:

$$\sigma_i = \sigma R_i + \sigma C_i \quad (2.1)$$

where σR_i and σC_i are the cross-sections for Rayleigh and Compton scatter of element i respectively.

Photoelectric Effect

The phenomenon of photoelectric absorption, discovered by Albert Einstein in 1905, can only occur if the photon's energy is equal to or greater than the electron's binding energy. A photon is absorbed and an inner shell electron is ejected in the photoelectric effect. A fraction of a photon's energy is utilized to overcome the electron's binding energy, while the remainder is transferred to the expelled electron as kinetic energy (Janssen & Lehner, 2014). Because the ejection of electron results in the development of a vacancy, the atom becomes excited and emits an Auger electron (characteristic photon) to return to its stable configuration. The ratio of released characteristic X-ray photons to the total number of inner shell vacancies created in the atomic shell is known as fluorescence yield (Beckhoff et al., 2007). After absorption, the intensity I_0 of an X-ray beam traveling through a layer of thickness d and density ρ is decreased to an intensity I , according to Lambert-well-known Beer's law as shown in equation (2.2):

$$I = I_0 e^{-\mu \rho d} \quad (2.2)$$

where μ is the mass attenuation coefficient.

The number of photons (intensity) decreases, but their energy remains relatively constant (Janssens et al., 2017).

As more vacancies are produced, the photoelectric cross-section grows, but at binding energies, the cross-section drops sharply because lower-energy X-rays cannot evict electrons from the K shell, but they can interact with weakly bonded electrons in the L and M shells. The absorption edge is the abrupt reduction in cross-section (Beckhoff et al., 2007), and the jump ratio is the ratio of the cross-section slightly above and below the absorption edge. Because X-ray fluorescence is caused by selective radiation absorption followed by spontaneous electron emission, an effective absorption process is required (Jenkins, 1995).

X-ray Absorption Phenomena

Absorption is the process of converting incident photon energy into the kinetic energy of a charged particle (usually an electron). The Beer-Lambert law yields four X-ray absorption coefficients (Storm et al., 1970).

1. Linear absorption coefficient μ_{lin} is given as absorption per unit thickness (cm^{-1}) as shown in equation (2.3)

$$\mu_{lin} = \ln(I_0/I)/d \quad (2.3)$$

2. Mass attenuation coefficient μ_M gives the absorption per mass in the unit area ($\text{cm}^2 \cdot \text{g}^{-1}$) as shown in equation (2.4)

$$\mu_M = \mu_{lin}/\rho \quad (2.4)$$

The absorption per atom in the unit area ($\text{cm}^2 \cdot \text{atom}^{-1}$) is given by the atomic absorption coefficient μ_a as shown in equation (2.5)

$$\mu_a = \mu_{lin} \cdot A/N \cdot \rho = \mu/n \quad (2.5)$$

The atomic weight is A , the Avogadro's number is N , and the number of atoms per unit volume is n .

3. The absorption per mole in a unit area ($\text{cm}^2 \cdot \text{mole}^{-1}$) is calculated using the molar absorption coefficient as shown in equation (2.6)

$$\mu_{mole} = \mu_{lin} \cdot A / \rho \quad (2.6)$$

The mass attenuation coefficient μ_M takes into consideration all of the possible interactions in the specimen. Thus μ_M is composed of three major compounds

$$\mu_M(E) = \tau(E) + \sigma_{coh}(E) + \sigma_{incoh}(E) \quad (2.7)$$

where $\tau(E)$, $\sigma_{coh}(E)$ and $\sigma_{incoh}(E)$ are photoelectric, coherent and incoherent mass attenuation coefficients, respectively.

Photons are completely absorbed in photoelectric absorption, providing energy for orbital electrons to move and imparting kinetic energy to them, leading to the emission of X-ray spectral lines. During the scattering phase, photons are not absorbed but deflected off their collimator path in the absorber.

Absorption Factor

The interelement impact is largely influenced by the absorption phenomena. The fluorescent element is believed to be unaffected by any other element in the sample in this section. As a result, its emission is purely owing to primary energy excitation. Taking into account that the excitation is monochromatic, the fluorescent intensity is simply given by

$$I_i(E) = S_i(E) \cdot C_i \cdot A_i(E) \quad (2.8)$$

where

$A_i(E) = 1 - \exp[-a(E)\rho d/a(E)]$ is known as the absorption factor,

$S_i(E)$ is the sensitivity of the system, C_i is the concentration of the element i in the sample and $a(E)$ is the average absorption correction factor which is given by

$$a(E) = \mu_i(E_0) \csc \varphi_1 + \mu_f(E_i) \csc \varphi_2 \quad (2.9)$$

Where E_0 is the photon's incident energy and E_i is the emergent energy, φ_1 is the incident angle and φ_2 is the emergent angle

For thin samples the absorption is negligible and the relation between the concentration and the intensity is linear

$$I_i(E) = S_i(E) \cdot C_i \quad (2.10)$$

For infinitely thick samples ρd in the absorption term

$$A_i(E) = 1/a(E) \quad (2.11)$$

The equation that relates the intensity and the concentration becomes

$$I_i(E) = \frac{S_i(E) \cdot C_i}{a(E)} \quad (2.12)$$

If the concentration C_i and the sample absorption $a(E)$ are known, the sensitivity for any element may be determined:

$$S_i = \frac{I_i(E) a(E)}{C_i} \quad (2.13)$$

In either scenario, a spectrometer's sensitivity can be written as

$$S_i = G \varepsilon_i K_i \quad (2.14)$$

where G is a proportionality constant that depends on spectrometer properties like source strength and system geometry, ε_i is the detector efficiency for element i and K_i is a factor comprising all the element-dependent basic parameters associated with element i . K_i is a number that is given by

$$K_i = \alpha_i E_o \left(r_k^{-1} / r_k \right) W_{ki} f \quad (2.15)$$

where $\alpha_i(E_o)$ is the element i 's photoelectric mass-absorption coefficient for the incident energy source. The K edge jump ratio is E , r_k , the K-shell fluorescence yield is W_k , and the branching ratio is f . Eqn (2.15) may be used to compute the factor k_i using Storm and Israel's tabulated data (Storm & Israel, 1970). A connection for the geometrical factor G can be found using Eqns (3.6), (3.8), and (1) (Greaves et al., 1992):

$$G = \frac{I_i(\mu_i \text{cosec}\phi_1 + \mu_f \text{cosec}\phi_2)}{\varepsilon_i K_i C_i} \quad (2.16)$$

In theory, regardless of the element being tested, this value should be the same. When determining a spectrometer's sensitivity, however, the standard deviation (SD) values computed with Eqn (2.16) vary for different elements. The average value of the calibration must not have a relative standard deviation (RSD) larger than 3% as a requirement for its quality (Greaves et al., 1992; Tang & Gomez, 1994). There is evidence of mistakes in the measurements of one or more thick samples when this restriction is not met (e.g. sample inhomogeneity, coarse grains in a pellet, lack of surface polish, concentration inaccuracy) (e.g. sample inhomogeneity, coarse grains in a pellet, lack of surface polish, error in the concentration).

Enhancement Factor

The enhancement is also a major contribution to the interelement effects and it occurs when the radiation from another element in the specimen excites the analyte. The essential criteria for excitation are that only X-ray photons with an energy greater than that of an element's absorption edge may stimulate that element's fluorescence. This adds more to the main X-rays' excitation of the target's characteristic lines. The main spectrum is the most important contribution to the specimen's emission. Secondary fluorescence occurs when an element with a higher atomic number than the fluorescent element is present. For example, consider a Fe-Ni alloy submitted to the same incident radiation. Both elements are excited by the primary radiation and consequently the Fe atoms are also subjected to the Ni fluorescent radiation. Because Ni – K_{α} radiations are sufficiently energetic to excite Fe atoms, an additional Fe emission is observed as secondary fluorescence which is indirectly produced by the primary radiation with energies greater than Ni energy absorption edge. Due to the enhancement factor $(1 + F_i^{Enh})$ the intensity becomes

$$I_i = G \times \varepsilon(E_i) \times K_i(E_o) \times C_i \cdot A_i(E) \times (1 + F_i^{Enh}) \quad (2.17)$$

X-ray Fluorescence Spectroscopy (XRF)

Basic principle of XRF

The X-ray region, also known as the Röntgen region, begins at 10 nm and extends to shorter wavelengths. Because X-rays have the same energy as inner-shell electron binding energies, they can be used to excite or analyze these atomic levels. (Beckhoff et al., 2007). The electromagnetic wave is

emitted and absorbed in photons, which are discrete units of energy proportional to the frequency of radiation. The atomic model postulated by Bohr consists of a nucleus with protons and electrons occupying discrete energy shells. The photoelectric effect occurs when the energy of a photon exceeds the binding energy of an electron in the shell, causing the electron to be expelled (Jenkins, 1999a). Due to the ejection of an electron from the K shell, the atom is left in a high energy state, resulting in atom instability. There are two methods by which the atom can recover to its normal state: auger effect and fluorescence (Van Grieken & Markowicz, 2001). The auger effect occurs when an electron from a higher orbital fall into the core hole, transferring energy to an electron from the outer shell and forcing the outer electron to expel. On the other hand, when an electron from the outer shell falls into the core hole, the extra energy can be released as an X-ray photon in a process known as X-ray fluorescence. Fluorescence radiation can be emitted by transitions that take less than 100 fs and follows the selection rules for electric dipole radiation (Beckhoff et al., 2007). The emission of this distinctive radiation allows elements to be identified. Measurement of the energy of characteristic X-ray photons generated from the sample from line spectra with all the characteristic lines superimposed above a fluctuating background can be used to quantify the elements (Gauglitz & Moore, 2014b).

Selection Rules and Characteristic Lines

X-ray spectral series, such as K, L, and M series include the allowed transitions that may fill the vacancy in a named atomic shell (Figure 4).

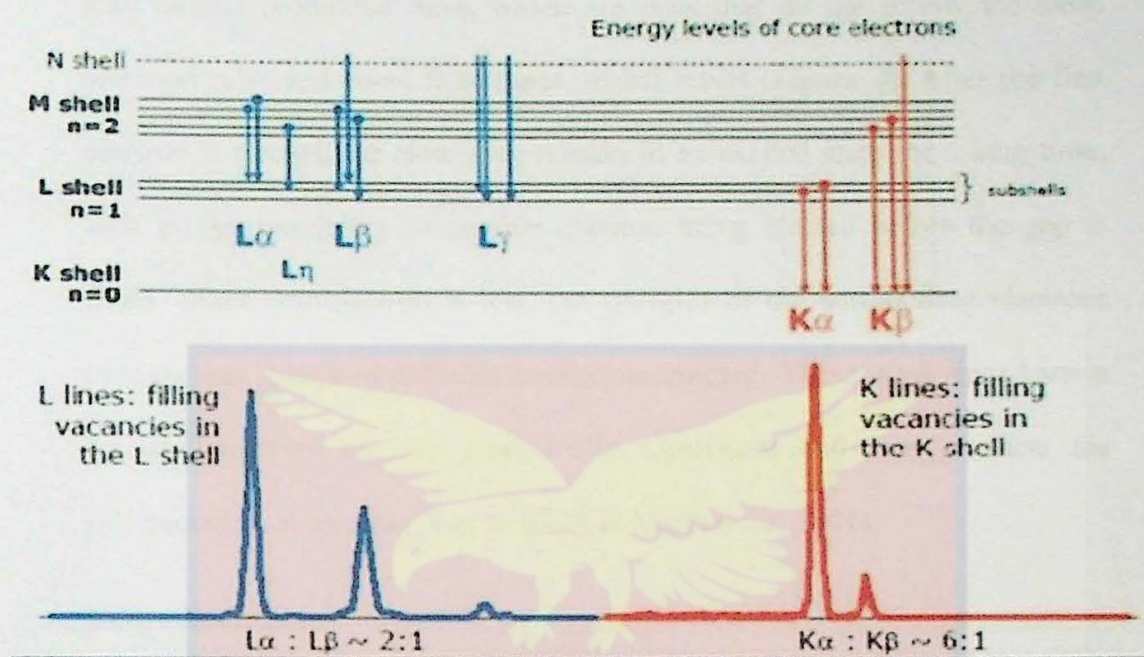


Figure 4: Observed characteristic line in K series for X-ray fluorescence

Additional notions such as α , β , and γ indicate which higher energy sub-shell the electron originated from. For example, K α 1 and K α 2 indicate the transitions from L3 and L2 sub-shells, whereas, K β 1, K β 2, K β 3 lines are produced during the transitions from M3, N2 and M2 sub-shells (Vo-Dinh, 2006). Every electron is described by four quantum numbers: the principal quantum number n , which can take any integral value (for K level $n=1$, for L level $n=2$, and so on), the angular quantum number l , which can take any value between $(n-1)$ and 0, the magnetic quantum number (m), which can take any value between $+l$ and $-l$, and the spin quantum number s , which has a value of $1/2$. The vector sum of l + s gives the entire momentum J of an electron (Janssens et al., 2017). To form normal lines, the main quantum number must change by at least 1, the angular quantum number must change by only l , and total momentum must change by 0 or 1. (Beckhoff et al., 2007). X-ray spectra

may contain prohibited lines, which are lines that do not follow the basic selection rules and come from outer orbital levels (*Figure 4*). After the first electron is ejected, the atom may remain in an excited state for a long time, with a high possibility of another electron being ejected before the gap is filled. When one electron is lost, the energies of the surrounding electrons change, and X-rays of different energy are emitted. These weak lines known as satellite lines are not analytically significant and may confuse the interpretation of spectra (Van Grieken & Markowicz, 2001).

Instrumentation

The main components of the XRF spectrometer are:

Excitation source

The excitation energy is required more than the binding energy of the electrons of the atom for the production of X-ray fluorescence. The excitation is mostly produced by X-ray tubes in laboratory instruments whereas, radioactive sources like Am-241 as shown in *Figure 5*, rotating anodes, and synchrotrons (Janssens et al., 2017) are common in transportable instruments and for highly sophisticated investigations, respectively.

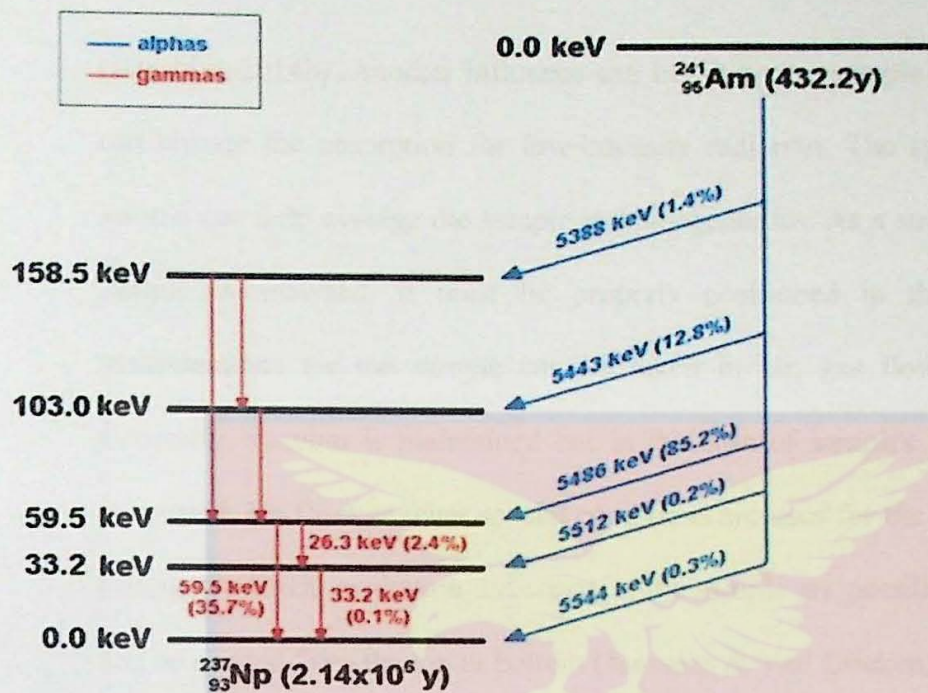


Figure 5: Diagram showing the Am-241 decay scheme with two major energies emitted at 59.5 keV and 26.3 keV.

Primary Optics

To bend the beam before it strikes the sample, primary optics is placed between the X-ray source and the sample. These are used to control the source radiation distribution. Secondary optics with similar optics can be employed to shape the secondary beam. Filters for absorption of specific sections of the spectrum, collimators and apertures for determining beam form, and monochromators for selecting a monochromatic beam are all possible primary optics (Haschke, 2014b).

Sample Positioning System

A manual or motor-driven positioning system can be used to position the sample if it is in a tray or on a stage, but the position needs to be reproducible with the source and spectrometer. D stands for the distance between the source and the sample influences the measured intensity by $\frac{1}{D^2}$.

(Haschke, 2014b). Another influence can be tilting the sample surface which can change the absorption for low-intensity radiation. The spinning of the sample can help average the sample in homogeneities. As a small area of the sample is analysed, it must be properly positioned in the beam. The measurements for the sample can be taken in air, gas flow, or vacuum. Generally, vacuum is maintained but in the case of samples that cannot be evacuated, He-flush or other special conditions are used for the analysis of the sample. Different excitation directions of the sample are possible. The sample can be excited from the top or bottom (Janssens & Van Grieken, 2004).

Secondary Optics

As a beam shaper, secondary optics may be required to improve resolution but can also be a dispersive optic that is used as a monochromator (Haschke, 2014b).

Detector

There are two types of detectors as follow:

Wavelength Dispersive X-ray Fluorescence Spectrometer (WDXRF)

The sample emits X-rays, which are directed to the crystal, which diffracts them in different directions depending on their wavelengths. The detector is fixed in place, but the crystal is rotated to allow the detector to take up different wavelengths (Beckhoff et al., 2007). The resolution of WDXRF lies between 5 eV to 20 eV. Higher-resolution reduces spectral overlaps and allows the analysis of complex samples with higher accuracy. It also reduces background and enhances detection limits and sensitivity, but using more

optical components reduces efficiency and costs more (Janssens & Van Grieken, 2004).

Energy Dispersive X-ray Fluorescence Spectrometer (EDXRF)

In EDXRF, the complete spectrum is captured at the same time, allowing elements from most of the periodic table to be detected in a matter of seconds (Haschke, 2014b). As EDXRF takes less time for the generation of spectra, it is widely used in element mapping to build up detailed element images with a high spatial resolution for thousands of pixels (Beckhoff et al., 2007).

Sample Preparation

Accurate analysis by XRF requires adequate sample preparation. Samples must be prepared according to the method of analysis and should be representative of the bulk material being tested (Beckhoff et al., 2007). Samples should fit into the chamber of the XRF spectrometer. Therefore, the sample used for X-ray spectroscopy needs to be effectively homogenized and mostly in fine powder form, but may also be liquid (Janssens et al., 2017). Lack of sample homogeneity is the most important factor which can cause inaccuracy in X-ray assessment-based element quantification methods larger than matrix effects (Beckhoff et al., 2007), as only a small amount, as well as the area of the sample, is analysed (Haschke, 2014b).

Solid Samples

A solid sample could be analysed as a bulk sample without any preparation, fused with glass, as a loose powder or powder pressed in pellets (Jenkins, 1995). However, most solid samples require pre-treatment such as cutting, grinding, or polishing before analysis to meet the requirement of homogeneity and ensure accurate and quality analysis (Margui & Van Grieken, 2013). Direct measurement is used when any type of sample preparation may damage its structure. This method of analysis is used for characterizing cultural heritage material that is usually fragile and in the study of gems and jewelry (Margui & Van Grieken, 2013). Direct measurement is also used for the analysis of layer systems, corrosion layers, contamination, and non-homogeneities of valuable samples (Haschke, 2014b). Fusion of samples with glass minimizes matrix and surface effects, but not all samples fuse with glass without prior treatment (Jenkins, 1995).

The most common method of analysis is powder preparation. The sample is finely powdered, combined with the binder/matrix, and pressed into pellets or tablets resulting in a homogenous sample with a flat surface (Haschke, 2014b). Pellets must be compacted and ideally presented as a pellet so that the angle of incidence of the X-rays is uniform and the emitted fluorescence can be captured without bias from all parts of the sample.

Liquid samples

Liquid samples could be analysed directly, by taking a few milliliters placed in a cup made of polyethylene or polytetrafluoroethylene with a thin

film at the bottom to allow the penetration of X-rays (Margui & Van Grieken, 2013). A film is not required for top-down measurement, and measurements can be taken without any absorbing substance in between (Haschke, 2014b). In liquid samples, the light matrices generate a higher scatter background which reduces the sensitivity compared to solid samples (Margui & Van Grieken, 2013), but the sample is homogeneous, and negligible particle size effects are present (Jenkins, 1995). Sometimes, the powdered suspension of water-insoluble material is mixed with a few milliliters of water and filtered through cellulose, glass or plastic filters resulting in a thin layer on the filter which is directly measured by XRF (Margui & Van Grieken, 2013).

Factors Influencing XRF Measurements

Matrix Effect

The X-ray matrix effect is the most basic and key component in analytical accuracy. The accumulated counts of X-ray photons are always accompanied by statistical fluctuations. As the incident beam passes through the sample it is absorbed due to interaction with atoms and emits fluorescence in all directions (Beckhoff et al., 2007). Fluorescence radiation directed at the detector is captured directly, but it can also be absorbed by the matrix along the route (Haschke, 2014a). Only a small number of circumstances allow for a simple linear relationship between observed element counts and concentration. Beyond the sample's critical depth below the surface, any emitted photons are absorbed and will not contribute to the fluorescence intensity (Janssens et al., 2017). This critical depth varies according to the matrix composition and the energy of primary and secondary radiation. The samples thicker than critical

penetration depth are called infinitely thick or massive samples. Attenuation and enhancement phenomena affect the intensity of X-ray fluorescence, causing matrix effects. The reported XRF intensity will no longer be proportionate to the element concentration due to the matrix effect.

Atomic Number of Elements

It is difficult to detect elements with a low atomic number as compared to the elements with a high atomic number as their excitation probability is very low (Haschke, 2014b). If the fluorescence radiation emitted is of low energy, it may be absorbed in the sample itself.

Sample Particle Size and Homogeneity

The detected concentration of elements depends upon the exact position of measurement as X-rays can penetrate only a few mm into the sample (Hou et al., 2004). Sample inhomogeneity can drastically affect the results of quantification of elements and result in low accuracy of quantification (Haschke, 2014a). Particle size effects are generally classified as grain size effects, inter-element effects, or mineralogical effects (Krusberski, 2006). Within the powdered samples analyzed by XRF, particle size effects are a serious source of analytical errors contributing >30% deviation if the samples have highly heterogeneous particle size distributions (Mzyk et al., 2002).

Sample Moisture

The sample's moisture content is regarded as one of the most significant sources of error, particularly in soil analysis (Bastos et al., 2012). The primary radiation is absorbed as well as scattered by water, resulting in an exponential reduction of characteristic X-rays (Ge et al., 2005). The effect of moisture on XRF intensity can differ from one element to another and is known to influence light elements (K and below) more as compared to heavier elements (Schneider et al., 2016).

Quantitative Spectra Analysis

X-ray spectra evaluation is one of the most critical steps in XRF. It provides a means of mapping the measured XRF spectra to the actual chemical composition of the sample. When a sample that contains REE is irradiated by a primary X-ray source, fluorescent X-rays from REE are generated. The intensity of these fluorescent X-rays is proportional to the amount of REE present in the sample. The higher the amount of REE, the higher will be the count intensity in its corresponding energy channel. Thus, if the fluorescent X-ray intensity and concentration of an element contained in a standard sample are both known, then calibration can be established to determine the concentration of REE from its fluorescent X-ray count intensity. Obtaining this calibration function is the main objective of all quantitative XRF analysis methods.

The XRF analysis method involves the techniques for extracting the most accurate information possible about the characteristic lines (Jenkins, 1995). In general, amplitude noise, which arises from the statistical character of the counting process, can be distinguished from energy noise, which causes the X-ray lines in the spectra to seem considerably broader than their natural widths (Janssens et al., 2017). X-ray lines appear as small, well-defined peaks in XRF, and net and background intensities can be estimated with accuracy (Vo-Dinh, 2006). In both XRF and WDXRF, the net number of counts under a characteristic line is proportional to the analyte concentration which is also true for concentration and net peak height. Peak area as an analytical signal is chosen in XRF since the detector resolution is poor and peaks may be low in intensity. This results in decreased statistical uncertainty for small peaks (Haschke, 2014a). Since the late 1980s, several research studies have been published on automated XRF spectrum analysis algorithms. The intent has been to develop software to assist technicians in XRF quantitative analysis. For example, the International Atomic Energy Agency's (IAEA) QXAS software uses an Analytical X-ray Analysis by Iterative Least-squares (AXIL) method, in which the net peak information is obtained by fitting measured spectra with mathematical functions tailored to specific elements using a nonlinear least-squares strategy (IAEA, 2005).

The significant information is included in the characteristic spectral peaks in XRF quantitative analysis, and the background continuum is regarded a nuisance. Eliminating the continuum can improve the accuracy of the net peak area determination. There are generally two methods to eliminate the

background continuum in XRF spectra. The first method directly eliminates the background using a heuristic approach while the second method estimates the background using a set of analytical functions (Jenkins, 1999b). The continuous is eliminated from spectra in the first technique by using an appropriate filter with minimal or no knowledge of the actual XRF background which makes it more suitable for real-time analysis because it is computationally less demanding. In the second method, the continuum is modelled using various analytical functions which are least-squares fitted to segments of background spectrums. Modelling the continuum involves using analytical functions tailored to represent the various excitation conditions and widths of regions in the XRF spectrum (Van Grieken & Markowicz, 2002). This method, as applied to this research, is further described below.

Background Estimation

For determining detection limits, repeatability, and reproducibility, background radiation is a limiting factor (Li et al., 2020). Electron beam excited samples are not perfectly flat, the background shape is not fully predictable, so questions arise concerning how much of the available spectrum should be used to measure the peak area (Statham, 1977). In spectra in which severe peak overlap is not encountered, and well-defined background regions are detected on both sides of the peak, simple background subtraction methods can be used. If the neighbouring peaks lie too close to the peak of interest, the background is estimated through the least square fitting of background or quantitative regression analysis models (Jenkins, 1995). The background is estimated using least-squares polynomial fitting on user-defined subsets of

points that should belong to the backdrop. The fitting produces satisfactory results for background estimation if those spots are correctly picked (Mazet et al., 2005). When utilizing calibration curves to create regression models, the spectrum background might be added to account for the sample's lack of precise background removal (Jenkins, 1995).

Linear Least Squares Fitting

If we have a large number of experimental data points (x_i, y_i) to fit, by this best straight line:

$$f(x_i, a) = f(x_i, a_1, a_2) = a_1 + a_2 x_i \quad (2.18)$$

We acquire values a_1 and a_2 in a manner that the total of the square differences between the observed data y_i and the estimated $f(x_i, a)$ is lowest using least-squares fitting. The goal is to discover (a_1, a_2) in such a way that

$$X^2(a_1, a_2) = \sum_{i=1} (y_i - f(x_i, a_1, a_2))^2 w_i \quad (2.19)$$

By the connection, the weighted w_1 are related to the counting statistics error in y_i .

$$w_i = \frac{1}{y_i} \quad (2.20)$$

X^2 is the chi-square function of the two variable a_1 and a_2

The minimum of X^2 is obtained by setting the partial derivatives of X^2 with respect to a_1 , and a_2 to zero and calculating the values of a_1 , and a_2

$$\frac{\partial X}{\partial a_1} = 0 \quad \text{and} \quad \frac{\partial X}{\partial a_2} = 0 \quad (2.21)$$

This results in a two-equation system with two unknowns.

$$\sum_{i=1}^n (y_i - a_1 - a_2 x_i) w_i = 0 \quad (2.22)$$

$$\sum_{i=1}^n (y_i - a_1 - a_2 x_i) x_i w_i = 0 \quad (2.23)$$

The values of a_1 and a_2 are obtained by solving these two linear equations.

This linear system of order 2 could be represented in matrix form as:

$$\begin{bmatrix} \sum_{i=1}^n w_i & \sum_{i=1}^n x_i w_i \\ \sum_{i=1}^n x_i w_i & \sum_{i=1}^n x_i^2 w_i \end{bmatrix} \begin{bmatrix} a_1 \\ a_2 \end{bmatrix} = \begin{bmatrix} \sum_{i=1}^n y_i w_i \\ \sum_{i=1}^n y_i x_i w_i \end{bmatrix} \quad (2.24)$$

$$[\alpha \quad a] = \beta \quad (2.25)$$

The general term for any linear fitting function with linear parameters a_j :

$$f(x, a_1, a_2, \dots, a_n) = a_1 f_1(x) + a_2 f_2(x) + \dots + a_n f_n(x) \quad (2.26)$$

Solving the linear system yields the ideal parameters for the fitting function that best suit the experimental data y_i

$$[\alpha \quad a] = \beta \quad (2.27)$$

$$a = \alpha^{-1} \beta \quad (2.28)$$

where

$$\beta_k = \sum_{i=1}^n y_i f_k(x_i) w_i \quad (j, k = 1, \dots, n) \quad (2.29)$$

and

$$\alpha_{j,k} = \sum_{i=1}^n f_j(x_i) f_k(x_i) w_i \quad (j, k = 1, \dots, n) \quad (2.30)$$

Non-linear Least-Squares Fitting

If we take the case of fitting a different set of points with a Gaussian plus a background, was observed as,

$$f(x_i a_i, \dots, a_5) = a_1 + a_2 x_i + a_3 \exp\left[-\frac{1}{2} \left(\frac{x_i - a_4}{a_5}\right)^2\right] \quad (2.31)$$

where

a_1 and a_2 are the background parameters

a_3 is the height of the peak

a_5 is the width of the Gaussian peak

then the set of equations resulting from setting the X^2 partial derivatives to zero with respect to its parameters is non-linear.

As a result, for a non-linear function, X^2 must be reduced iteratively, that is, by intelligently altering the parameters at each iteration and reducing X^2 until it reaches the lowest.

AXILQXAS uses the Marquardt algorithm to implement its iterative technique. To assure convergence, this method combines the function's linearization with a gradient search

Function Linearization Method

When it comes to function linearization, $f(x_i, a) = f(x_i a_i, \dots, a_n)$ at the k th iteration is expanded to first-order Taylor expansion as a function of the parameters a_j :

$$f(x_i a_1, \dots, a_n) = f(x, a^k_1, \dots, a^k_n) + \sum_{i=1}^n \frac{\partial f(x, a^k_1, \dots, a^k_n)}{\partial a_j} (a_j - a^k_j) \quad (2.32)$$

Setting $(a_j - a^k_j) = \sigma a_j$

where a^k is the parameter vector's value at iteration k

The result is a linear function with parameter increments $\sigma a_j (1, \dots, n)$ such that

$$X^2 = \sum_{i=1} [(y_i - f(x_i, a^k)) - \frac{\partial f(x_i, a^k)}{\partial a_1} \sigma a_1 - \dots - \frac{\partial f(x_i, a^k)}{\partial a_n} \sigma a_n]^2 w_i \quad (2.33)$$

The X^2 can be minimized for each parameter σa_j by using the traditional method of linear least squares

At the k th iteration, this yields a set of n simultaneous linear equations in matrix form:

$$\begin{bmatrix} \sum_{i=1} \frac{\partial f}{\partial a_1} \frac{\partial f}{\partial a_1} w_i & \sum_{i=1} \frac{\partial f}{\partial a_1} \frac{\partial f}{\partial a_n} w_i \\ \sum_{i=1} \frac{\partial f}{\partial a_n} \frac{\partial f}{\partial a_1} w_i & \sum_{i=1} \frac{\partial f}{\partial a_n} \frac{\partial f}{\partial a_n} w_i \end{bmatrix} \begin{bmatrix} \sigma a_1 \\ \sigma a_n \end{bmatrix} = \begin{bmatrix} \sum_{i=1} (y_i - f(x_i, a^k)) \frac{\partial f}{\partial a_1} w_i \\ \sum_{i=1} (y_i - f(x_i, a^k)) \frac{\partial f}{\partial a_n} w_i \end{bmatrix} \quad (2.34)$$

$$a^k \qquad \sigma a^k = \beta^k \quad (2.35)$$

At iteration $k+1$, the increments in each parameter σa_j are added to the previous estimation a^k to produce a new one a^{k+1}

$$a^{k+1}_j = a_j^k + \sigma a_j^k \quad (2.36)$$

The process above is repeated until the last iteration yields a tiny X^2 or until a different stopping criterion is met.

While this analytical method based on extending the fitting function $f(x, a)$ for its parameters a_j converges quickly to the minimum X^2 , it cannot be depended on to approach the minimum with precision from an initial guess outside the range where the fitting function can be accurately represented. As a result, if the initial guess of the fitting parameters is far from the minimum, this method is known to diverge

Gradient Method

In this method, there is a step off from the current trial value in the direction of the negative gradient of X^2 controlling the step size carefully in order to assure the decreasing behaviour in the X^2 and thus achieving convergence.

$$-\nabla X^2 = -\left(\frac{\partial X^2}{\partial a_1}, \dots, \frac{\partial X^2}{\partial a_n}\right)^T \quad (2.37)$$

$$-\nabla X^2 = \begin{bmatrix} \sum_{i=1} (y_i - f(x_i, a^k)) \frac{\partial f}{\partial a_1} \\ \sum_{i=1} (y_i - f(x_i, a^k)) \frac{\partial f}{\partial a_n} \end{bmatrix} \quad (2.38)$$

The new trial a^{k+1} is obtained from the previous trial using

$$a_j^{k+1} = a_j^k + \frac{1}{\lambda} \sum_{i=1} (y_i - f(x_i, a^k)) \frac{\partial f}{\partial a_j} \quad j = (1, \dots, n) \quad (2.39)$$

This method has a slow convergence property, and when the search approaches the minimum, it suffers greatly.

Marquardt Algorithm

The best aspects of both the gradient search technique and the approach of linearizing the fitting function are combined in this algorithm. The algorithm's main outline is that during the k th iteration, the matrix α and vector β described below are formed, and the system is created:

$$\alpha' \sigma a = \beta \quad (2.40)$$

where

$$\alpha' = \alpha(1 + \lambda) \quad (2.41)$$

This algorithm lowers the difficulty of function linearization by solving if λ is small ($\alpha' \cong \alpha$). When is λ big, the diagonal terms of the matrix' dominate, and the equation degenerates into n distinct equations.

$$\sigma a_j = \left(\frac{\lambda}{\alpha_{jj}}\right) \beta_j \quad j=1, \dots, n \quad (2.42)$$

The factor λ in the Marquardt algorithm is thus used to perform an optimum interpolation between function linearization as the X^2 parameter is decreased and gradient search direction as the parameter is increased: the new X^2 is tested at each iteration; if it is reduced, the iteration is said to be successful; otherwise, the same iteration is repeated while increasing the parameter V until the new X^2 is decreased. After each successful iteration λ is decreased in order to speed up convergence.

Treatment of Peak overlaps

Overlapping of peaks occur when the energies of two or more elements are close to each other. Peak overlap can significantly reduce the accuracy of X-ray spectrum quantification (Jalas et al., 2002). To determine the accurate net area under each peak, the overlap must be addressed (Jenkins, 1995). Deconvolution refers to assigning the areas to peaks of interest (Brouwer, 2006).

Interpolate the background under the peak and add the net channel contents in a window containing the peak to calculate the net area of an isolated, non-overlapped peak in an EDXRF spectrum. As a result, we can calculate the net peak area N as follows:

$$N = \sum_j [y_j - y_{B(j)}] = \sum_j y_j - \sum_j y_{B(j)} = T - B \quad (2.43)$$

where the summation is applied to the spectral window (which contains n_T channels) in question. As a result, the uncertainty s_N can be expressed as:

$$S^2_N = S^2_T + S^2_B = T + B \quad (2.44)$$

The average background height left and right of the peak (respectively, $y_{B,L} = BL/nL$ and $y_{B,R} = BR/nR$, where BL and BR are the integrals of the left and right background windows and nL , nR their channel widths) can be interpolated between the background height $y_{B(j)}$ in channel j of the peak window

$$y_{B(j)} = y_{B,L} + \frac{y_{B,R} - y_{B,L}}{j_{B,R} - j_{B,L}} \chi(j - j_{B,L}) \quad (2.45)$$

The channels between which the background is linearly interpolated are $j_{B,L}$ and $j_{B,R}$. The uncertainty on N is provided by: where both background windows around the peak have equal width (i.e., $nL = nR = nB/2$ channels) and are symmetrically positioned around the maximum:

$$S^2_N = T + (n^2_T/n^2_B)(BL + BR) \quad (2.46)$$

Peak overlap is common in energy-dispersive X-ray spectra, and the background intensity below the peak, particularly for peaks corresponding to trace elements, can be on par with or even greater than the net peak intensity. To minimize the weighted difference Π^2 between experimental data y_i and a mathematical fitting function y_{fit} , a non-linear least-squares technique is widely used.

$$\Pi^2 = \frac{1}{t-n} \sum_i \left(\frac{y_i - y_{fit,i}^{(i)}}{y_i} \right)^2 \quad (2.47)$$

In the investigated spectrum, y_i is the observed content of channel i , and y_{fit} denotes the estimated fitting function. The total number of channels in the fitting window is t , and n is the fitting function parameter number. The latter is split into two sections, one for the background spectral and the other for the photo peaks.

$$y_{fit}(i) = y_{back}(i) + y_{peak}(i) = y_{back}(i) + \sum y_j(i) \quad (2.48)$$

where the index j refers to all of the spectrum's characteristic line groups. For each line group j (e.g., Fe-K, Pb-L3), the contribution $y_j(i)$ to the i th channel is determined as follows.:

$$y_j(i) = A_j [\sum_{k=1}^{N_j} r_{jk} G(E_{jk}, i) t(E_{jk})] \quad (2.49)$$

The total area of all picture peaks in line group j is A_j (comprising, for example, the $Fe - K_\alpha$ and $-K_\beta$ lines); these are parameters that can be optimized during the least-squares fitting procedure. Each line in group j has a relative abundance r_{jk} (with $\sum_k r_{jk} = 1$), and the index k runs over all of them. G_{jk} is a Gaussian function centered on E_{jk} , and $t(E_{jk})$ is the overall attenuation factor for X-rays with energy E_{jk} , as specified by radiation absorption in the detector, absorbers between the sample and the detector, and the sample itself.

Methods and models for quantitative analysis

The standard curve created by standard samples is used in quantitative analysis. The measured intensity value of the unknown element in an actual measurement is fed into the standard curve to derive the elemental concentrations. Standard samples, as well as unknown elements, should be measured in similar settings (Bandhu et al., 2000).

Statistical Theory for Method Validation

Accuracy

Accuracy refers to the degree of agreement of a measurement made from a sample being analysed with the 'true result' obtained from an accepted reference standard.

Precision

Precision refers to the degree of agreement between the repeated individual measurements made on the same sample. The precision of a method may be excellent, but its accuracy may be very poor. The terms accuracy and precision are often misused and frequently interchanged.

True Value

The true value is the value of a characteristic obtained from an accepted reference standard.

Chapter Summary

This chapter reviewed literature related to rare earth elements and the various methods employed for their analysis. Lanthanides (atomic numbers 57–71) and yttrium, which have a chemical behaviour similar to the heavier lanthanides, are examples of rare earth elements (REEs). REEs are classified into two categories: light (from La to Sm) and heavy (from Eu to Lu). They have chemical and physical properties that are similar. Physical procedures have largely replaced many of the existing classical methods for determining REEs. These spectrometric techniques, particularly XRF, have advanced with

the use of several major radiation sources, such as radioactive sources, X-ray tubes, or synchrotron light.

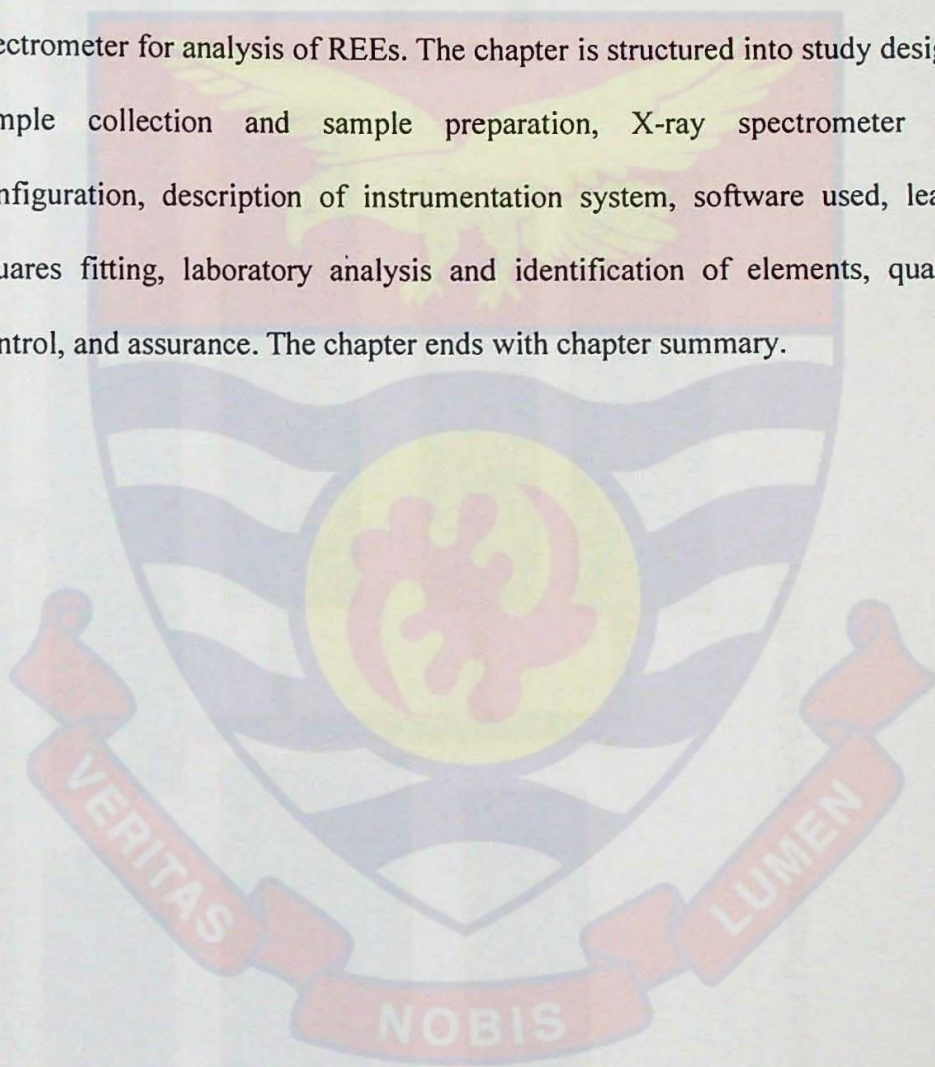


CHAPTER THREE

RESEARCH METHODS

Introduction

This chapter presents the research method employed to extend the capability of the EDXRF spectrometer system at GAEC with the optimised attached Am-241 excitation-based system to the existing Ag-anode X-ray tube spectrometer for analysis of REEs. The chapter is structured into study design, sample collection and sample preparation, X-ray spectrometer re-configuration, description of instrumentation system, software used, least-squares fitting, laboratory analysis and identification of elements, quality control, and assurance. The chapter ends with chapter summary.



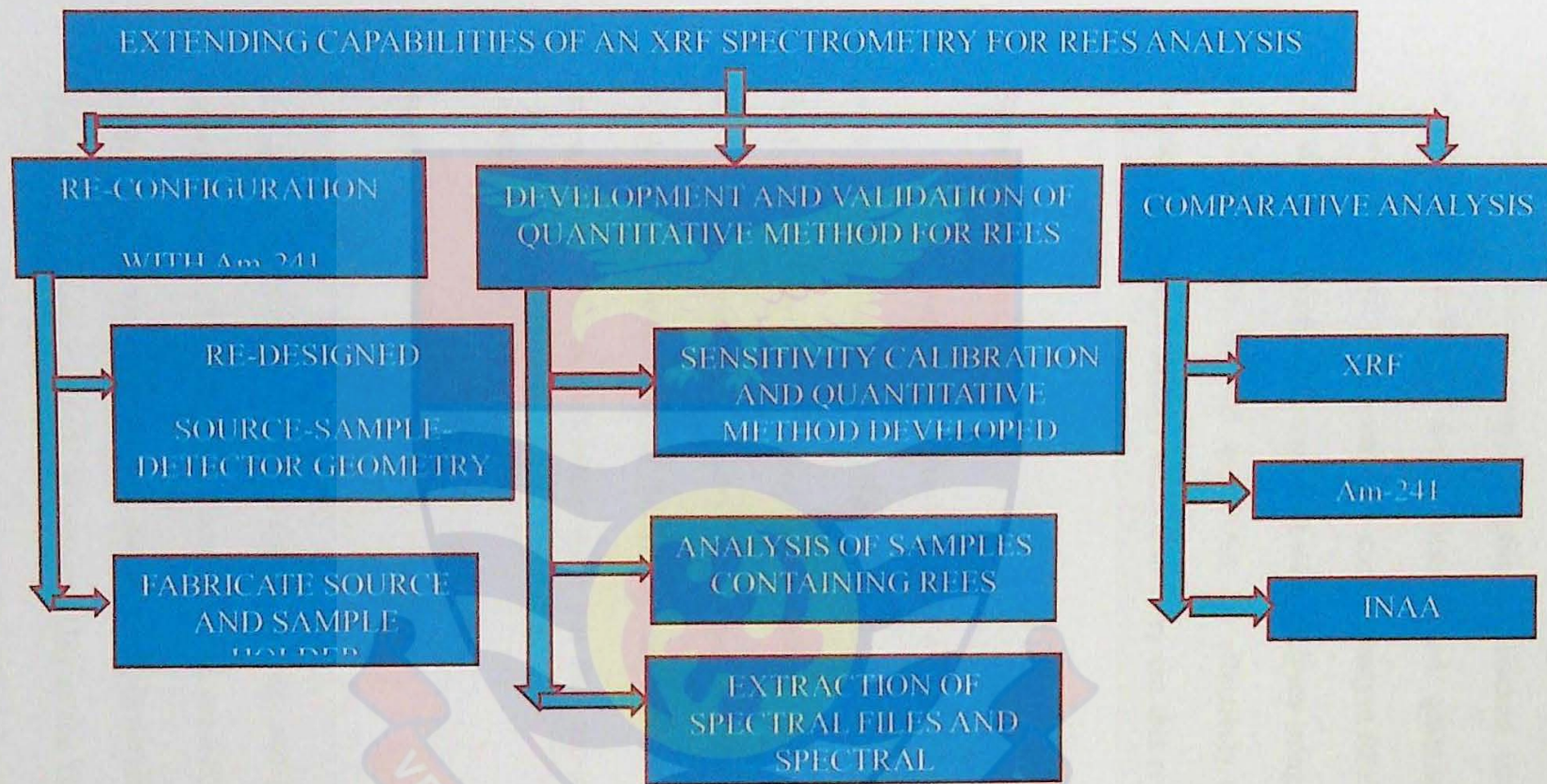


Figure 6: Project Framework (Field Data,2021)

To expand the scope of the analysis of the existing XRF system for REEs, it was necessary to reconfigure the current spectrometer by attaching an Am-241 excited system. Subsequently, the optimised attached Am-241 excited system settings were calibrated for qualitative and quantitative analysis. The calibrated attached system was then used to analyse REE-containing samples and results were obtained compared with analyses using conventional X-ray tube XRF system, ICP-MS and INAA. To effectively address the research problem, the overall strategy utilised to carry out this research is outlined in Figure 6

Sample Collection

Twenty standard samples and three rock samples that contain REEs were collected. The standard samples collected were based on their K and L-lines which fall within the energy range of the REEs. The standard samples were collected from the Chemistry department and the rock samples from the Earth Science department of University of Ghana. The samples before transportation into the laboratory were put into zip-lock bags to prevent contamination and labeled.

Sample Preparation

Twenty-five standard samples (*S, Cl, K, Ca, Ti, Cr, Mn, Fe, Co, Ni, Cu, Zn, As, Br, Sr, Mo, Ag, Cd, Sn, I, Cs, Ba, W, Hg, and Pb*) were obtained in powdered form. The rock samples were crushed, ground, and sieved through a 100 μ mesh sieve. Pellets were made with hydraulic pelletizer (Carver Technologies, Auto-CrushIR, Wisconsin, US) at the Ghana Atomic Energy Commission (GAEC) using a stainless steel pellet die with a diameter of 2.5 cm .

To make a pellet (see Figure 8), the pellet die compresses sample powders between two flat polished discs at a rate of 20 tons per square inch. Ten grams of each sample were compressed into 2.5 cm diameter pellets with a 0.5 cm thickness. No binder was added to the samples because the pellets were strong and did not desegregate. After each sample preparation, the pelletizing die was cleaned with ethanol. Before being used, the pellets were placed in the 150 mm desiccator (AS ONE, 240, Vietnam) overnight.



Figure 7: Assembly of the Pressing die.

Procedure in Assembly of the Pressing Die

(See Figure 7) shows the assembly of the pressing die where the press housing is initially positioned on the base plate.

- 1) the first pressing plate is inserted into the housing.
- 2) the sample material is added, and the second pressing plate is placed on top.
- 3) The polishing surfaces are facing the sample.
- 4) Prior to pelletizing, both pressing plates were covered with unique thin coatings to prevent contamination.



Figure 8: Prepared Pellets in a petri dish.

X-Ray Spectrometer Re-configuration

The benchtop XRF spectrometer at GAEC was attached to a developed Am-241 excitation-based system. The design and the construction of the excitation system focus on three main parts, namely:

- (i) An excitation source.
- (ii) A sample
- (iii) A detection system

Excitation Source

The first step in X-ray spectrometry analysis is the selection of a primary radiation source. This is usually determined by the sample element of interest, which in this work are REES (like *Sc, La, Ce, Sm, Eu, Nd, Gd, Tb, Yb, and Lu*) in geological material. The XRF spectrometer at GAEC is based on a commercially available benchtop X-ray spectrometer (EXP-1) manufactured by Amptek Technologies. The spectrometer uses Ag-anode X-ray tube as its excitation source. To expand the scope of elements that can be analysed, an Am-241 excitation-based system was designed, constructed, and attached to the existing XRF spectrometer. The attached Am-241 excitation-based system has been effectively used in the analysis of materials from geological source (Funtua, 2004). The X-ray tube and the attached Am-241 excitation-based system were linked to the data acquisition software (DPPMCA) for the acquisition of the spectra. The source-sample-detector geometry was subsequently optimised.

Samples

The developed Am-241 excitation-based system was constructed to be able to hold and analyse the different types of samples (solid, liquid, and filters) not limited by their dimensions. The chamber is shielded with lead blocks to protect the operator of the system.

Detection Systems

One of the main functions of the spectrometer is to detect K- X-rays of REEs.

The determination of the K-X-rays improved detection limits and efficiency for REEs. The detector used for the developed Am-241 excitation-

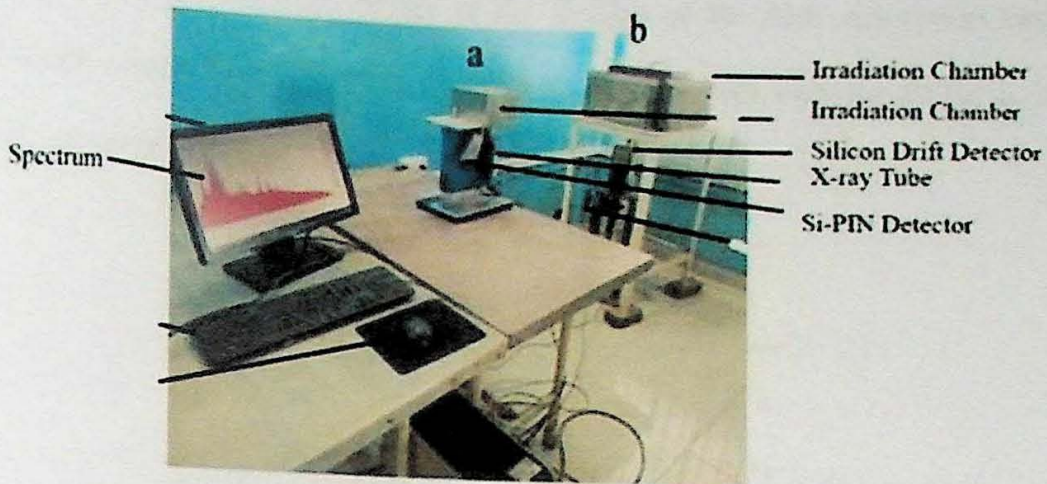
based system was the Si-PIN detector (Amptek, Bedford, MA, USA). The Si-PIN detector has an area of 60 mm^2 , active depth of 500 mm , and resolution of 160 eV at 5.9 keV . The X-123 Silicon Drift Detector (Amptek Technologies) with a thickness of $500 \text{ microns } (\mu)$ and resolution of 125 eV full width at half maximum resolution at 5.9 keV (^{55}Fe) at $11.2 \text{ microseconds}$ peaking time was used for Ag-anode X-ray tube spectrometer.

To acquire X-ray spectra, DPPMCA software was used on a personal computer.

X-ray Spectrometer Chamber and Sample Holder Construction

The Am-241 excitation-based system chamber was designed and built with cast iron. The dimension of the chamber is $30 \text{ cm} \times 40 \text{ cm}$. *Figure 12* displays the chamber and the setup. The *Figure 9* including photographs of the EXP-1 with the attached Am-241 excitation-based system. The chamber housed the Am-241 excitation source sample holder. The aluminium plate in different dimension serve as a space between the source and the detector window and the same time as the sample holder (see *Figure 10*). The aluminium plate with dimensions of

$10 \text{ cm} \times 2 \text{ cm}$, $12 \text{ cm} \times 2 \text{ cm}$, $12.5 \text{ cm} \times 2 \text{ cm}$, $13 \text{ cm} \times 2 \text{ cm}$, $14 \text{ cm} \times 2 \text{ cm}$,
 $15 \text{ cm} \times 2 \text{ cm}$



a) EXP-1 Setup b) Am-241 excitation based system Setup

Figure 9: Photograph of EXP-1 (a) with the attached Am-241 excitation based system (b), connected to the monitor to display the spectra.



Figure 10: Aluminium plate that serves as the spacer and the sample holder

Description of Instrumentation Systems

X-ray Fluorescence Spectrometer

The EXP-1 has a silver anode X-ray tube used to excite the REE-containing samples, a silicon drift detector (SDD) was used to collect the fluorescent X-rays, and associated electronics were employed to analyse the spectrum (see *Figure 11*). The silver tube's average energy is 22.1 keV,

which is lower than the energy of the K-edge of the REE absorption band (which ranges from 33.440 to 54.063 keV). As a result, only the REEs' L-X-ray could be excited.

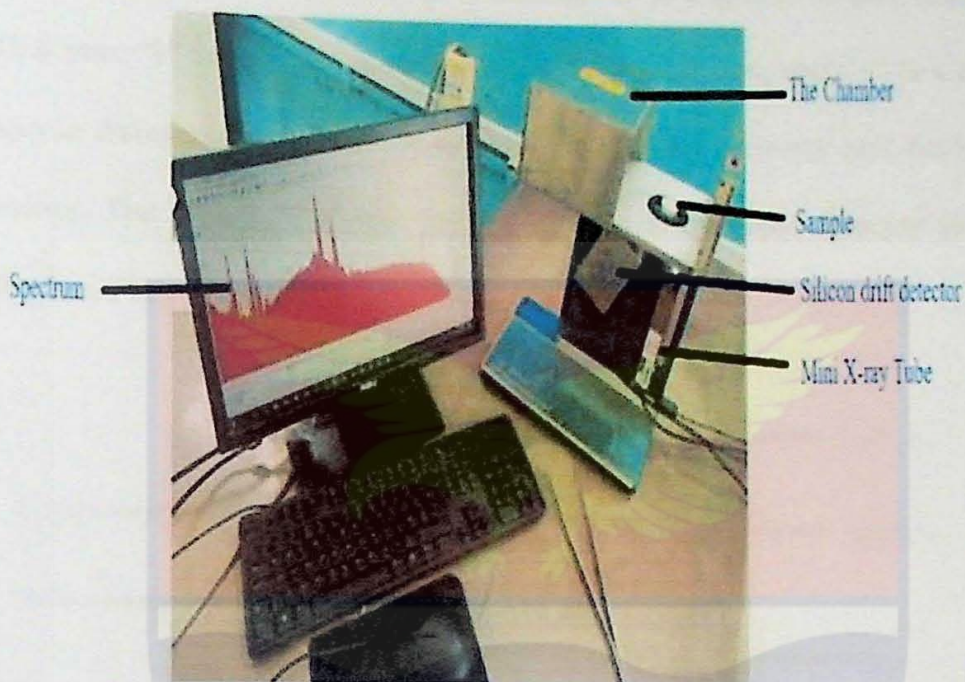


Figure 11: Labeled EXP-1, anode X-ray Tube Spectrometer Experimental Setup at the laboratory.

Am-241 Excitation based System

The instrumentation for Am-241 excitation-based system in this study included Am-241 source for excitation of REE-containing samples, a SI-PIN detector for collecting fluorescent X-rays, and associated electronics for spectrum analysis (see Figure 12). The Am-241 excitation source was chosen for continuous and monochromatic beam because of its stability and modest size. The Am-241 emits radiation at 26.4 keV and 59.5 keV, making it helpful for detecting high-atomic-number elements like REEs. Furthermore, because the energy of the K-edge of the REE absorption band is 33.440-54.063 keV, attached Am-241 excitation-based system could detect the characteristic K-

line of most REEs. The optimization of the geometric arrangement was evaluated with a barium oxides (BaO) pellet weighing about 10 g and 25 mm in diameter, which was positioned at a different distance from the source. The Table 3 in chapter four shows the distances, “a” is a sample-source distance of 10.0 mm; “b” is the sample-source distance of 12.0 mm, and “c” is a sample-source distance of 12.5 mm. Also shows measured intensity and background values. The *Figure 13* shows the optimum source-sample-detector geometry for Am-241 excitation-based system.

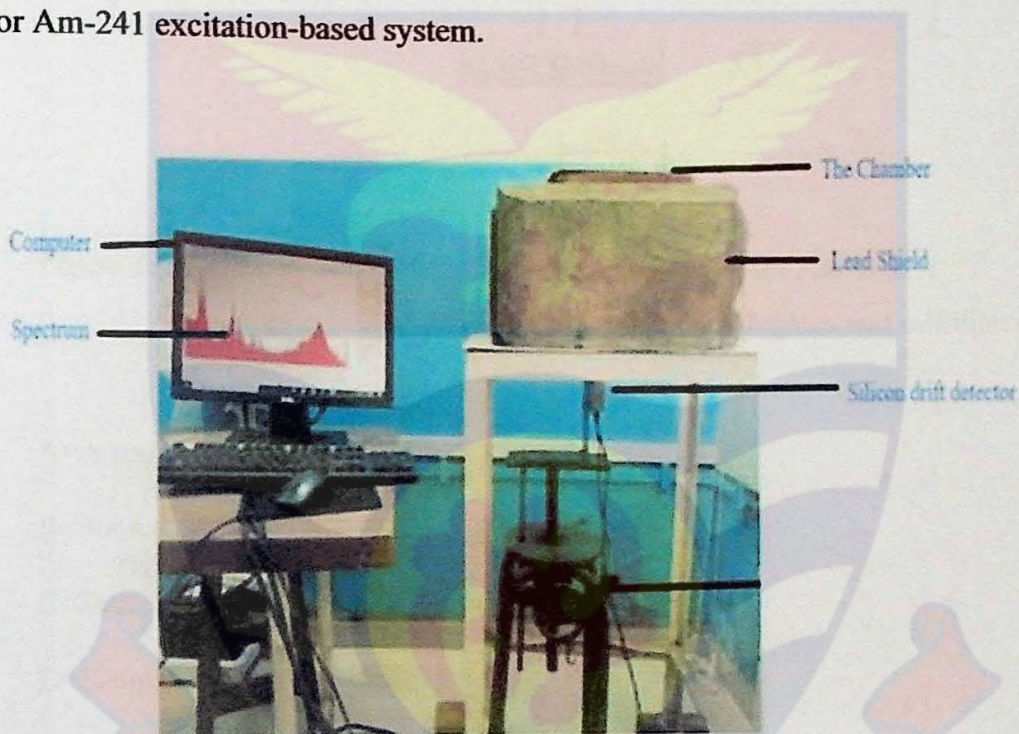


Figure 12: Am-241 excited-based system experimental setup.

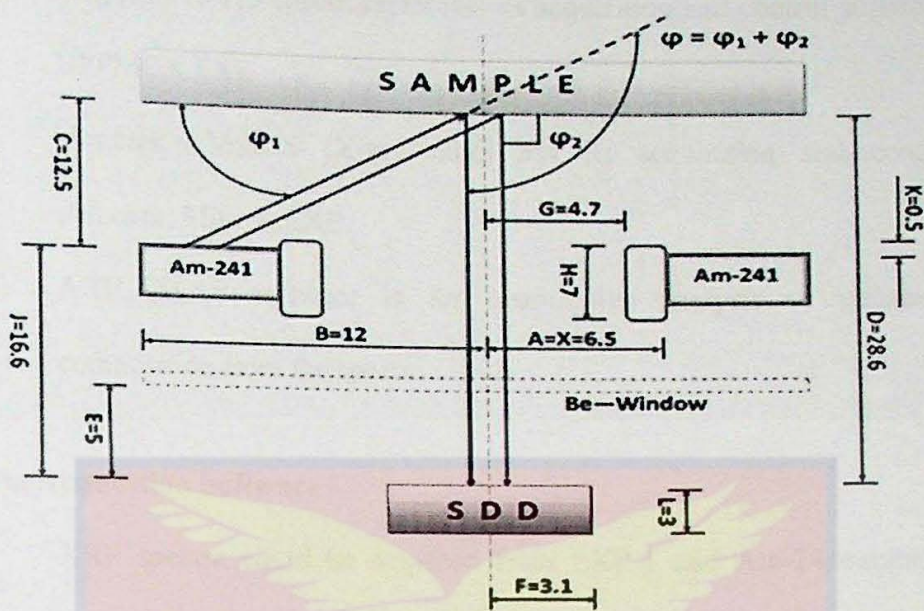


Figure 13: Optimum Source-Sample-detector geometry for Am-241
Excitation based System (measurements in degrees and millimeters)

- A=A source inside radius (6.5 mm)
- B=Source outside radius (12.0 mm)
- C=Source sample distance (12.5 mm)
- D=Sample-detector distance (28.6 mm)
- E=Detector-Be window distance (5.0 mm)
- F=Detector radius (3.1 mm)
- G=Collimator radius (4.7 mm)
- H=Collimator height (7.0 mm)
- J=Source-detector distance (16.6 mm)
- K=collimator source distance (0.5 mm)

Software

Three suites of software utilized in this study for XRF were:

- (i) Amptek's X-123 spectrometer has its acquisition and control software, DPPMCA.EXE.
- (ii) Amptek's Mini-X (X-ray tube) has its acquisition and control software, Mini-X.EXE.
- (iii) AXIL/QXAS software is for quantitative analysis of elemental composition from the spectra.

Data Acquisition Software

XRF spectra could be acquired from EXP-1 and Am-241 excitation source XRF instruments through Amptek supplied acquisition software, DPPMCA.EXE platform. Mini-X.EXE platform control Amptek Mini-X X-ray tube. The software from the DPPMCA platform is capable of recording XRF count data in a data format (*.MCA files). These specially formatted files contain valid count rates and raw counts for each energy channel along with all instruments and XRF measurement parameters including instrument and ambient temperatures. Mini-X X.EXE software displays the voltage and the current inputs that generate the X-ray. The DPPMCA-based software supplied by Amptek contains databases. These databases enabled the software to automatically identify elements present in samples through proper calibration. The DPPMCA-based software is capable of creating custom XRF views, one of which is an overlay comparison of any two or more XRF spectra which were used extensively in this research. The DPPMCA-based software may be used to store data in a generic XRF data file. The DPPMCA-based software was utilized as the primary data acquisition software for this research to collect XRF measurements in a generic spreadsheet file format (*.MCA).

Signal Processing Software

The International Atomic Energy Agency's *QXAS – AXIL* (*Analysis of X – ray spectra by iterative least – squares fitting*) software was utilized for signal processing in this study (Bernasconi, 1993).

The AXIL program works by fitting a mathematical function (described by photo peaks and spectral background) to experimental data in both linear and non-linear ways. It includes many utility programs for converting MCA (multi-channel analyzer) spectrum files to a common format. During the spectrum evaluation process, the AXIL software converted the net peak intensities into concentration (He & Van Espen, 1991). *Figure 14* depicts an overview of the AXIL package's many modules and their interdependencies.

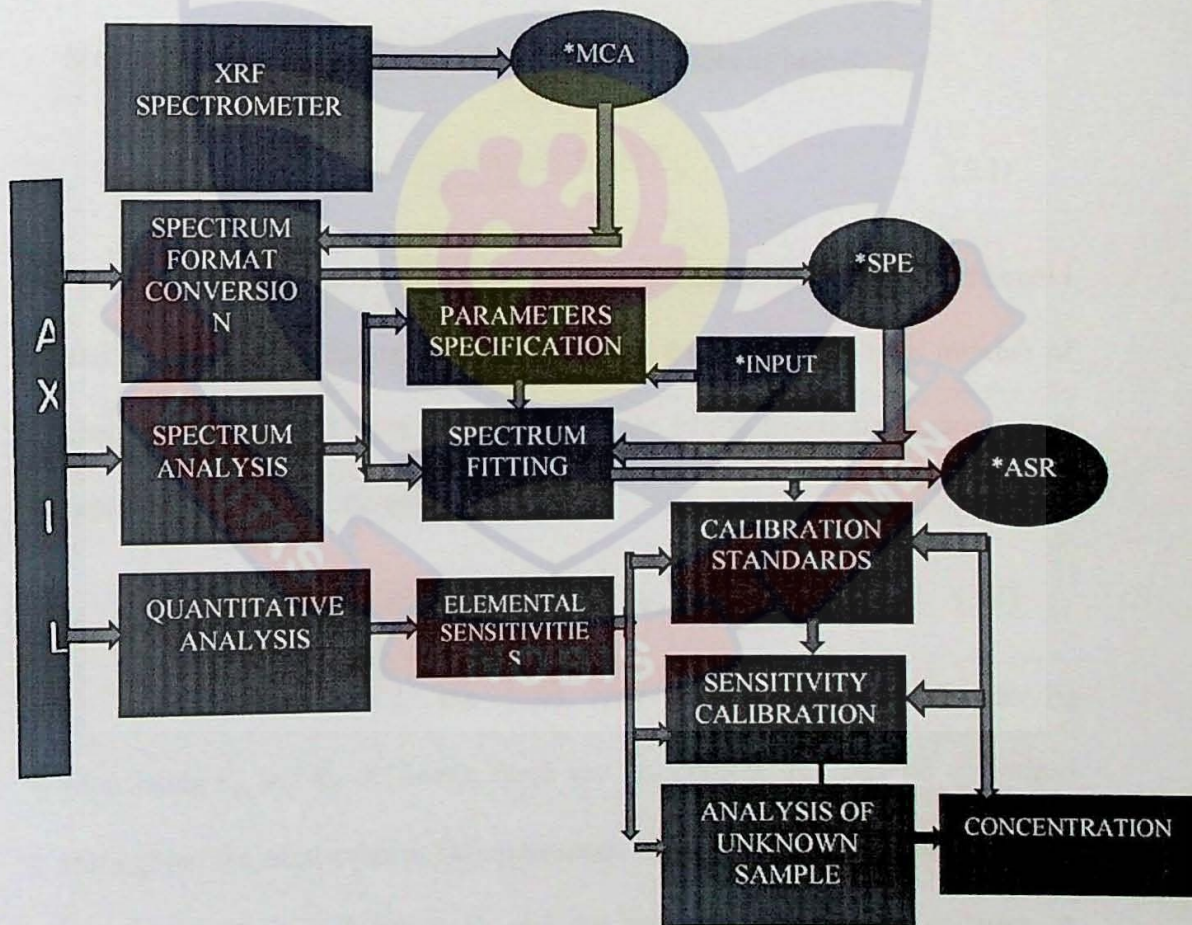


Figure 14: An overview of the AXIL package's various components and their interdependencies

Non-Linear Least-Squares Fitting

The spectrum evaluation in AXIL is based on the analyst selecting the appropriate input to the mathematical model to represent the experimental data. This is accomplished by defining the spectral region that needs to be fitted [Region of interest (ROI)], selecting appropriate background compensation technique, selecting several X-ray line groups to be included in the model (Fe-K α , Mo-K α , Pb-L1), and calculating the spectrometer's energy and resolution parameters. Using a non-linear least-squares technique, the weighted sum of differences Π^2 between the experimental data y_i and the mathematical fitting function y_{fit} is then minimized using a modified Marquardt algorithm to change the model parameters as below:

$$\Pi^2 = \frac{1}{n-m} \sum_i \left(\frac{[y_i - y_{fit,i(i)}]^2}{y_i} \right) \quad (3.1)$$

In the processed spectrum, y_i denotes the observed content of channel i and the determined fitting function is $y_{fit}(i)$, the fitting ROI total number of channels is indicated by n and the size of the fitting function's parameters is represented by m , as shown below:

$$y_{fit}(i) = y_{cont}(i) + \sum_j \text{Element } A_j [\sum_{K \text{ Line}} R_{jk} p(i, E_{jk})] \quad (3.2)$$

In line group j , the total area of all photo peaks is A_j (consisting K_α and K_β -K lines); these are parameters that can be optimized throughout the least-squares fitting process. Each line in group j has a relative abundance r_{jk} (with $\sum_k r_{jk} = 1$), and the index k runs over all of them. A

Gaussian function is denoted by the letter P. The Continuum function is $y_{cont}(i)$, R_{jk} line ratio, peak shape is E_{jk}

$$P = G(i, E_{jk}) \frac{Gain}{\delta_{jk} \sqrt{2\pi}} \exp[-\frac{1}{2}(\frac{E_i - E_{jk}}{\delta_{jk}})^2] \quad (3.3)$$

where E denotes the line's typical energy (eV). The spectrum GAIN in (eV/channel) for the energy E_i of channel i and the energy ZERO in (eV) at channel 0 are used to calibrate the energy.

$$\text{Energy Calibration} \quad E_i = ZERO + GAIN \times i \quad (3.4)$$

$$\text{Resolution Calibration} \quad \delta_{jk} = [(\frac{NOISE}{\sqrt{2 \ln 2}})^2 + \epsilon Fano E_{jk}]^{1/2} \quad (3.5)$$

The contribution of the electronic component to the peak width (usually 120 eV), the Fano factor (normally 0.114), and the average energy required in silicon to create an electron-hole pair are all represented by NOISE, FANO, and 3.85 (Paropkari et al., 2010; Van Grieken & Markowicz, 2001).

A nonlinear least-squares technique is necessary since the fitting function is linear in the net peak area parameters A_j but nonlinear in the parameters Zero, Gain, Noise, and Fano. The parameters' values are changed in a series of approximations until a minimum in Π^2 is obtained (Van Espen & Lemberge, 2000).

Neutron Activation Analysis

Low Enriched Uranium Miniature Neutron Source Reactor (LEU-MNSR) usually refer to as the Ghana Research Reactor-1 (GHARR-1), a 34 kW tank-in-pool Miniature Neutron Source reactor is installed at GAEC. It produces a maximum thermal neutron flux of $1 \times 10^{12} \text{ ncm}^{-2}\text{s}^{-1}$ at full power.

The five basic components of the MNSR are the concentrically structured uranium pin core, the bottom and side cylindrical beryllium reflectors, the top adjustable beryllium shims, the center single control rod, and the light water moderator and coolant (Baidoo et al., 2018; Osei et al., 2021).

Ten irradiation locations are available: five inside the beryllium reflector (inner sites) and five outside the beryllium reflector (outer sites). The assembly is placed in an Al-vessel and submerged in a stainless-steel-lined concrete pool. The GHARR-1 has been in service since 1995. The location has been used for reactor physics research, nuclear data, nuclear engineer training, and other nuclear-related human resource development. Neutron activation analysis is the most prevalent use, which is used to promote national research in geology, archaeology, food science, and other domains (Adazabra et al., 2014; Nyarko et al., 2003)

Laboratory Analysis and Identification of Elements

X-ray Fluorescence Analysis

The measurements of XRF were carried out at the GAEC XRF facility (see *Figure 9*). Both the Am-241 radioisotope excitation-based system and EXP-1 Ag-anode X-ray tube spectrometer use the same software for data acquisition (DPPMCA) and the concentration calculations (QXAS_AXIL software). The schematic of the experimental set-up for EXP-1, Ag-anode X-ray tube spectrometer is shown (see *Figure 11*) and that of Am-241 excited-based system (see *Figure 12*). EXP-1, Ag-anode X-ray tube spectrometer uses a SDD while the Am-241 radioisotope excited based system uses a SI-PIN detector. Both system (see *Figure 9*) are linked to a computer with DPPMCA spectroscopy software. The voltage and current supply to the tube are 45 keV

and 5 μA , respectively. The incidence angle and take-off angle for the EXP-1, Ag-anode X-ray tube spectrometer were both 67.50 degrees. The angle of incidence and take-off for the attached Am-241 excitation-based system were 52.5° and 90°, respectively.

Forceps and gloves were used to insert the sample into the sample chamber to avoid contamination during measurement. To obtain trustworthy results, the detection geometry for both methods was kept the same during counting measures, and each sample was counted for 120 seconds for the EXP-1 Ag anode X-ray tube spectrometer and 3000 seconds for the attached Am-241 excited-based system. The elements and their concentrations were discovered using the characteristic spectra lines emitted by the elements. The K_{α} and K_{β} -X-ray emissions were chosen as the focus. (Pemmer et al., 2013).

Furthermore, the QXAS-AXIL software was used to analyse the data (Alvarez et al., 2007). Fitting configuration functions were used to fit the curves. A number of parameters were calculated, optimized and used based on the specific detecting geometry to execute the program quickly. The elemental concentrations and mass fractions were then calculated using the fitted curve (see *Figure 15*).

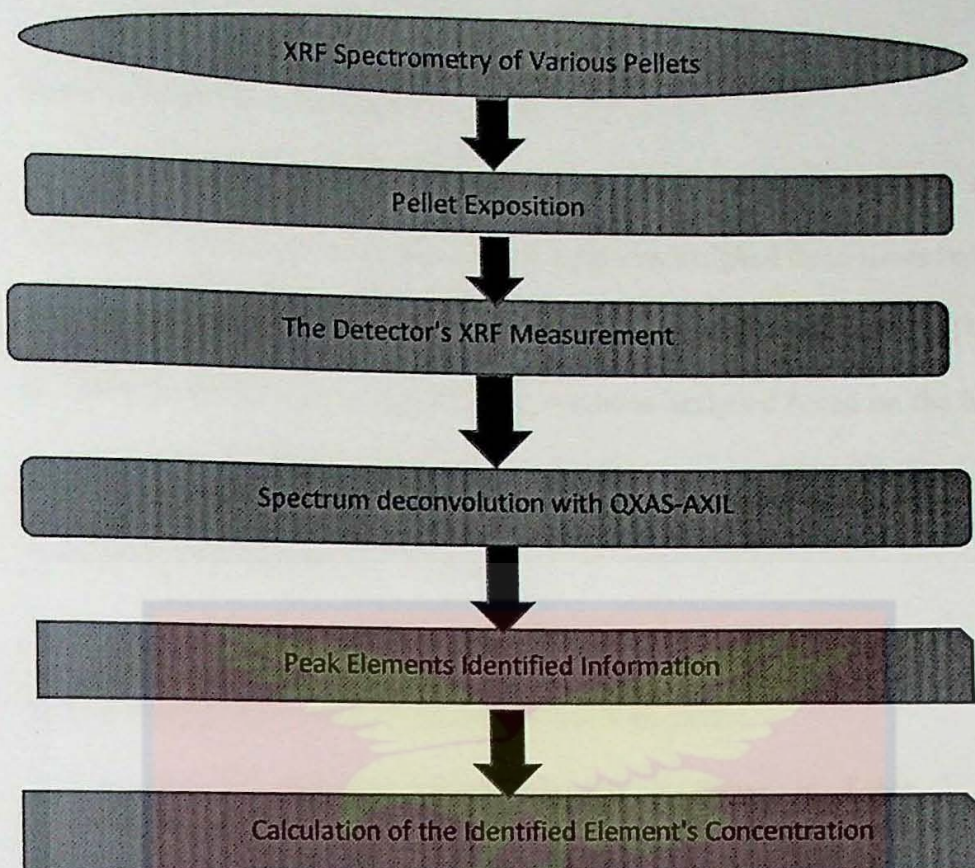


Figure 15: The XRF method for determining the concentrations of elements in a sample is described

Calculation for XRF Measurements

For each spectra line, the equation (2.17) describes the connection between intensity and mass concentration.

$$I_i = G \times \varepsilon(E_i) \times K_i(E_o) \times C_i \cdot A_i(E) \times (1 + F_i^{Enh}) \quad (3.6)$$

where

I_i is intensity, G is system geometry, $\varepsilon(E_i)$ is the efficiency of the detector, $K_i(E_o)$ is the fundamental parameters, C_i is the concentration, $A_i(E)$ is the absorption factor, and

$(1 + F_i^{Enh})$ is the enhancement factor

Neutron Activation Analysis

The GHARR-1 was used to irradiate REE containing samples and IAEA-soil 7 (reference material). Each sample was weighed three times before being wrapped in a thin polyethylene sheet and heat-sealed into pellets. There are three different types of irradiation procedures designed based on the half-lives of the components of interest:

- 1) short (nuclide half-life $t_{1/2}$ 2.5 hours);
- 2) medium (nuclide half-life $t_{1/2}$ 12 hours); and
- 3) long (nuclide half-life $t_{1/2} > 3$ days) (Osei et al, 2021).

The scheme for analysing certain elements is shown in *Table 2*. The irradiations were all done at a reactor thermal output of 17 kW, resulting in a thermal neutron flux of 5.0×10^{11} n/cm²s⁻¹.

Figure 16 depicts the analytical workflow, which begins with sample preparation and packaging and finishes with quantitative analysis and reporting.

Table 2: For Reference Materials, an Irradiation Scheme has been Devised

Irradiation time	Delay time	Counting time	Elements determined
1 min	5 min	10 min	Na, Mg, Al, Cl, K, Ca, Ti, V, Mn, Cu, I
1 hr	24 hrs	10 min	K, Zn, Ga, As, Br, Cd, La, Sm, Eu, U
5 hrs	7 days	5 hrs	Sc, Cr, Fe, Co, Zn, Rb, Sb, Cs, Ba, Ce, Nd, Sm, Eu, Tb, Yb, Lu, Hf, Ta, Th, U

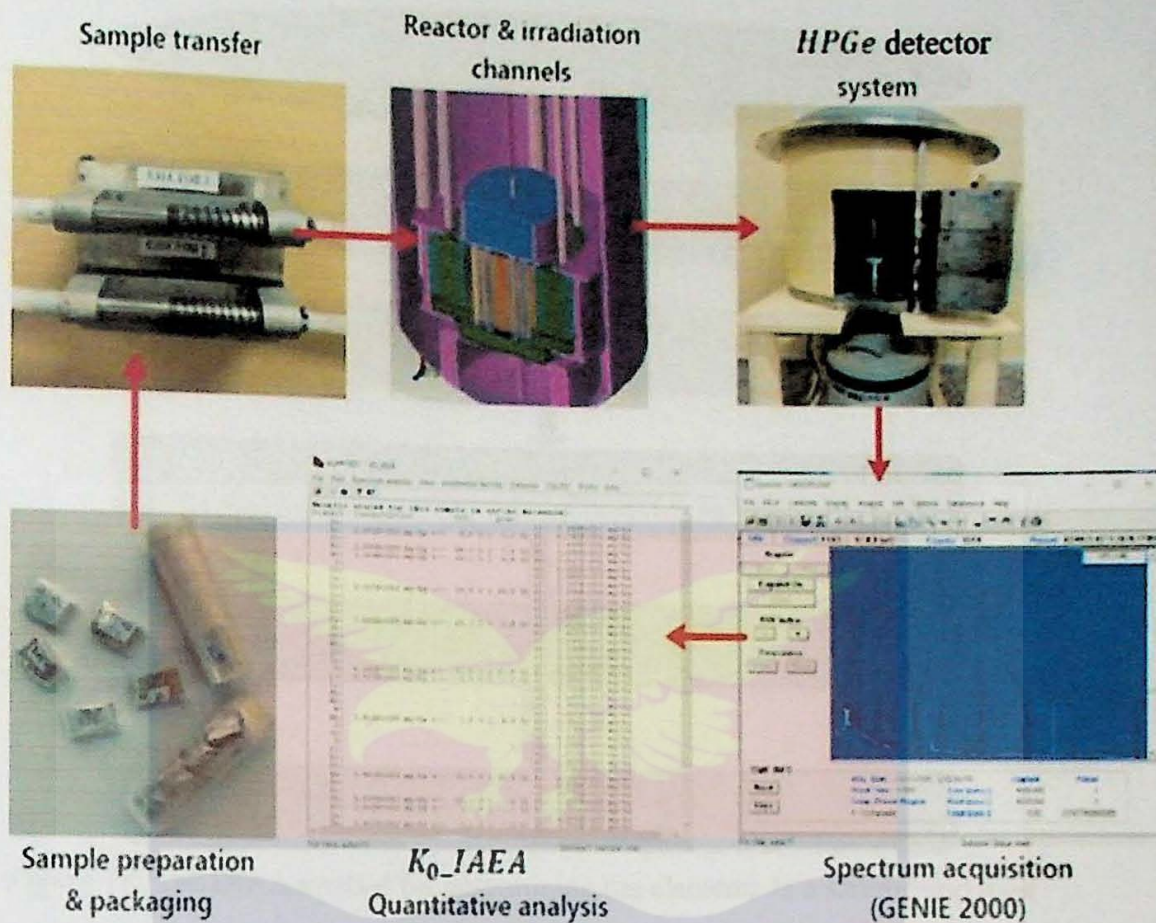


Figure 16: The GHARR-1 facility's INAA analytical workflow.

The REE samples were sent to the reactor using a pneumatic transfer mechanism during INAA operations at GHARR-1. After 22 hours of decay time, for 3 hours, samples were irradiated at half power and counted on the HPGe detector. The sample was sufficiently cooled for an appropriate activity with a decay time of 22 hours. After 96 hours of decay time, the sample was counted again to obtain a medium half-life element. The REE samples were then counted on the HPGe detector for three hours to provide better statistics and accurate data. For all counting experiments, the detecting geometry remained the same. The energy peaks for their associated. The mass of each element identified in each REE was calculated using the area value under each peak elements were found in the resulting energy spectrum (see Figure 17.).

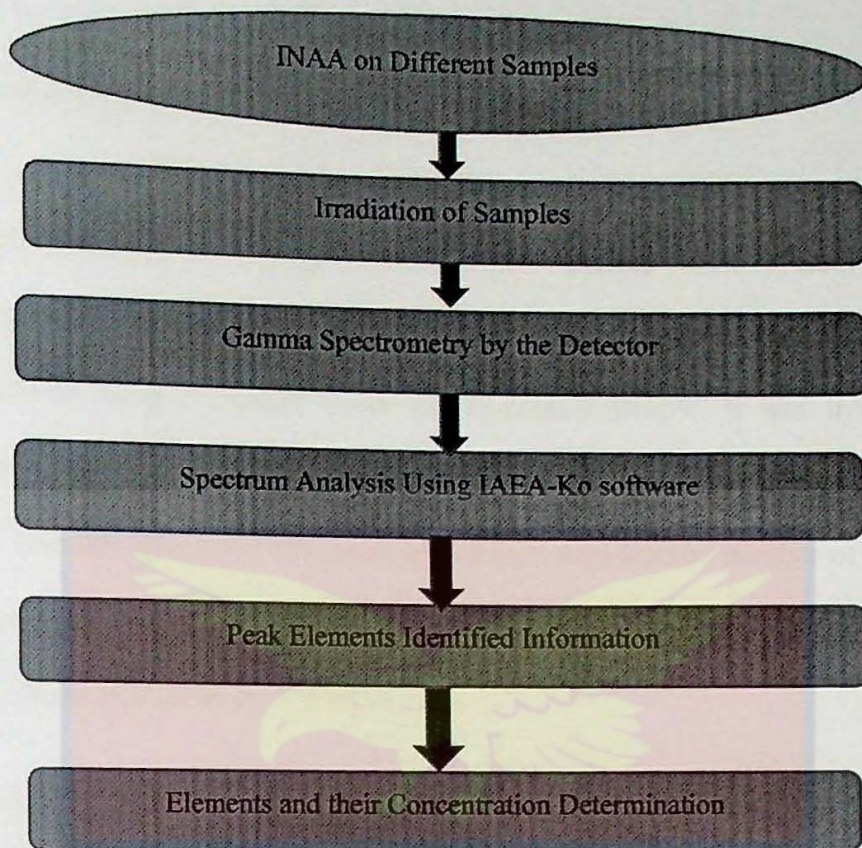


Figure 17: The INAA method for determining the elements in a sample and their Concentrations is described above.

INAA Measurement Concentration Calculation

The equation (3.7) could be used to relate the mass of REEs to the concentration of each element identified in the energy spectrum:

$$M = \frac{(\text{Peak area})(A_{rel})}{\phi_{th}\sigma_{th}N_AVe^{-\lambda t}} \quad (3.7)$$

Where M is the radioisotope's mass, The area beneath the energy peak corresponding to the radioisotope is known as the peak area, A_{rel} is the radioisotope's molecular weight, ϕ_{th} is the flux value of 4.3×10^{12} n/cm² s, σ_{th} is the radioisotope's thermal cross-section, Avogadro's Number is N_A , λ is the radioisotope's decay constant, and the radioisotope's decay time is t.

Quality Control

Control Chart

Control charts establish the precision of an analytical technique. To find out whether the attached Am-241 excited-based system XRF spectrometer at the GAEC was in statistical control, a control chart was generated using a Barium Oxide (BaO) control sample. It was irradiated before, during and after any batch of sample irradiation. This process was repeated throughout the analytical period until an adequate number of results were obtained. From twenty-one (21) results, the control chart was generated and interpreted using the Shewhart rules.

Method Validation

All outcomes must be traceable to a recognized standard in order to be comparable. The measurand (usually mass fraction) is indirectly linked to the measurement technique, which must be described as a function of the measurement parameter, by developing a working equation that models the experimental measurement and conditions and assigns results to the measurand (fluorescence characteristic radiation count rate). The validity and uncertainty evaluations are then used to see if the working equation (method specification) is accurate in describing the real situation (Alvarez et al., 2007)

The IAEA Soil 7 reference material was used to validate the method. The samples were examined under the same experimental conditions as the reference materials. Using the sensitivity curve of EDXRF for both EXP-1 and the attached Am-241 excitation-based system, the purpose of validation was to assess the precision and accuracy of the analytical results. The degree of

accuracy was calculated using the formula (Ventura et al., 2014) in equation (3.8) below:

$$\frac{\text{Observed value}}{\text{Expected Value}} \times 100\% \quad (3.8)$$

An average of nine results of the observed values was used to measure the degree of accuracy. In the meantime, the precision was assessed using the Shewhart rules (Durivage, 2021).

Comparison Method

To guarantee that the attached Am-241 excitation-based EDXRF developed meets expectations, it was compared to the INAA and ICP-MS on the same samples, in addition to technique validation using IAEA Soil 7 reference material. A samples (DK6, Dk7 and DK8) which were measured at Canada with ICP-MS, collected from the University of Ghana's Earth Science Department (Nude et al., 2015). The same samples were analysed using INAA and the newly designed attached Am-241 excited-based EDXRF equipment at the GAEC.

Instrumental Neutron Activation Analysis

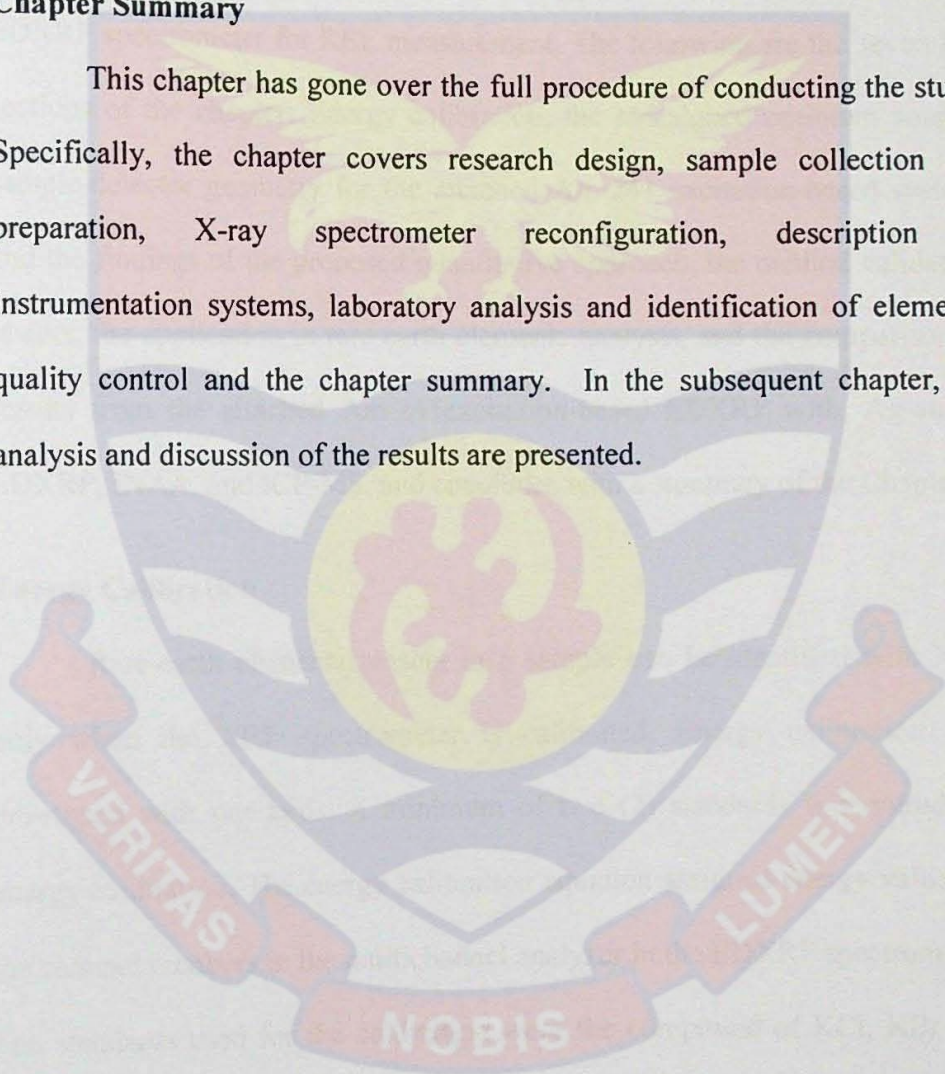
GHARR-1 is a 34 kW Miniature Neutron Source reactor with a tank-in-pool design installed in Ghana. At full power, it produces a maximum thermal neutron flux of 1×10^{12} n/cm² (Osei et al., 2021). The samples were exposed to half-power radiation. The HPGe detector picked up the outgoing gamma (γ)-rays. Ko-IAEA software was used to analyse the γ -ray spectra. Irradiating the Carbonate rock GBW07108 reference sample was used to calibrate the apparatus (Osei et al., 2021)

Inductively couple Plasma- Mass Spectrometry (ICP-MS)

Due of the inaccessibility of an ICP-MS in the Country, Ghana, the researcher unable to measure with one. A sample which was measured with ICP-MS from Canada was found at the University of Ghana's Earth Science department (Nude et al., 2015). The developed Am-241 excited-based EDXRF system was used to analyse these samples.

Chapter Summary

This chapter has gone over the full procedure of conducting the study. Specifically, the chapter covers research design, sample collection and preparation, X-ray spectrometer reconfiguration, description of instrumentation systems, laboratory analysis and identification of elements, quality control and the chapter summary. In the subsequent chapter, the analysis and discussion of the results are presented.



CHAPTER FOUR

RESULTS AND DISCUSSIONS

Introduction

This chapter summarizes the findings and discussions of the study to extend the capabilities of the EDXRF spectrometer at GAEC with the optimized attached Am-241 excitation-based system to the existing Ag-anode EDXRF spectrometer for REE measurement. The following are the seven key sections of the chapter: Energy calibration, the redesigned optimum source-sample-detector geometry for the attached Am-241 excitation-based system, and the findings of the proposed quantitative approach, the method validation results, the application in rare earth elements analysis, and the comparison of results from the attached Am-241 excitation-based EDXRF with, Ag-anode EDXRF, INAA, and ICP-MS, and concludes with a summary of the Chapter.

Energy Calibration

Rare-earth elements present in a sample can be identified with XRF only when the XRF spectrometer is calibrated. Energy calibration was developed with standards. A minimum of two (2) standards is required for energy calibration. The energy calibration equation assigned energy values to the channel numbers in the multichannel analyzer in the EDXRF spectrometer. The standards used for the calibration were the compound of KCl, KBr and MoO₃. The calibration was done with the Potassium at energy 3.312 keV, Bromine at energy 11.907 keV and Molybdenum at energy 17.478 keV peaks.

The energy calibration plot generated is presented in *Figure 18*. The equation generated was what the model used to assign the energies to the channels of the multichannel analyzer in the EDXRF spectrometer system.

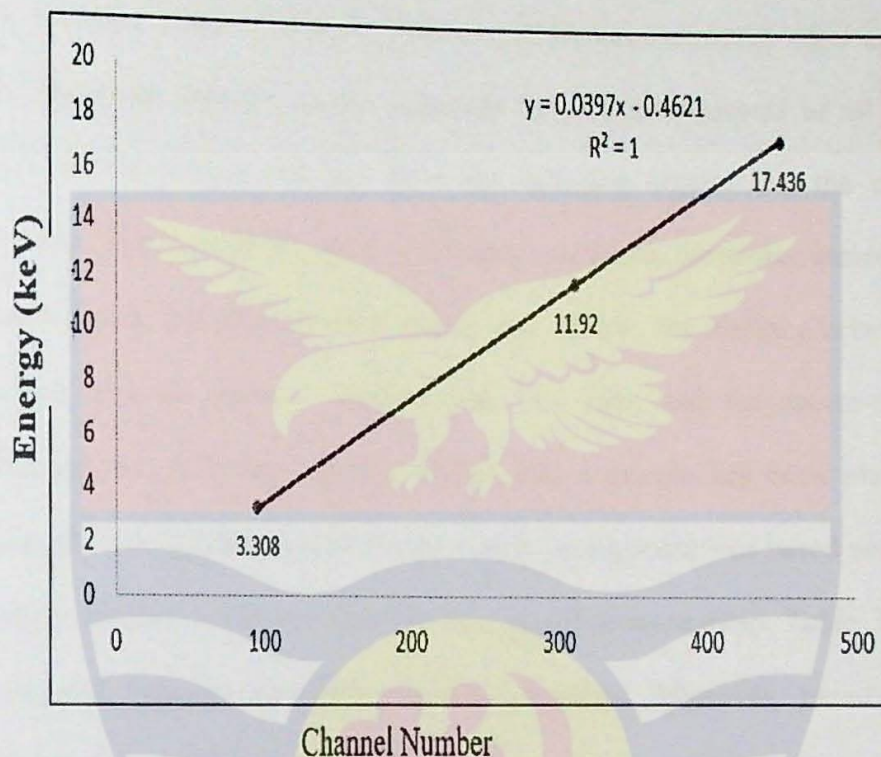


Figure 18: A graph of energy calibration showing the regression equation and the R^2 value.

Redesigned Optimum Source-Sample-Detector Geometry for the Am-241 Excited-based System

To extend the capabilities of the existing EDXRF spectrometer for REE analysis, an Am-241 excitation-based system was integrated into the existing Ag-anode EDXRF spectrometer (EXP-1). There was therefore a need to reconfigure the source-sample-detector arrangement by determining the optimise parameters for analysis. The Am-241 excitation-based source was of annular geometry. To reduce the interfering background signal while obtaining

the most analytical signal, the best sample-detector distance was evaluated. This arrangement ensures optimum fluorescence radiation detection efficiency. Therefore, a thick BaO sample pellet weighing 10 g and measuring 25 mm in diameter was put at various distances from the detector window and the radiation source. The X-ray intensity of *Ba* was measured. After analysis, the maximum detected counts represent the best arrangement of all factors such as the sample distance from the radiation source and the detector window. The detector Be-window distance was 5 mm, the source inside radius was 6.5 mm, the source outside radius was 12 mm, the distance between the sample and the detector window was 28.6 mm, and the source-detector distance was 16.6 mm. On the Myllar foil, a sample has been placed for analysis. The optimisation of the geometric arrangement was based not on the only maximum count but also the best signal-to-noise ratio. *Table 3* shows measured intensity and background/noise values. However, based on the signal-to-noise ratio optimal source-sample distance outcome is to be "c". Therefore, all of the samples in the specified sizes were arranged at the determined optimum distance of 12.5 mm. With the drawing of all measurements to scale, the optimal geometric configuration for the setting was found to be 52.5° for incident angle and 90° for take-off angle. This geometry has produced results that are comparable to INAA and ICP-MS results (see *Table 8*).

Table 3: Intensity and the Background Produced from the Various Distance from the Am-241 Source

	Distance (mm)	Intensity	Background/noise	Signal-to-noise ratio
a	10.0	61684.0	1156.0	53.4
b	12.0	53266.0	939.0	56.7
c	12.5	56456.0	932.0	60.6
d	13.0	30642.0	642.0	47.7
e	14.0	17945.0	602.0	29.8
f	15.0	14682.0	543.0	27.0

Development of Quantitative Method

Elements could be quantified using XRF with the equation (2.16).

$$I_i = G \times \varepsilon(E_i) \times K_i(E_o) \times C_i \cdot A_i(E) \times (1 + F_i^{Enh})$$

where

I_i is Intensity, G is system geometry, $\varepsilon(E_i)$ is the efficiency of the detector, $K_i(E_o)$ is the fundamental parameters, C_i is the concentration, $A_i(E)$ is the absorption factor, and

$(1 + F_i^{Enh})$ is the enhancement factor

There are three ways by which this equation can be applied. The fundamental parameter approach, the Elemental sensitivity approach and the direct comparison of count rates (Criss & Birks, 1968). The Elemental sensitivity approach was adopted, which involves sensitivity calibration using selected standards.

Sensitivity Calibration

The spectrometer sensitivity must be measured to be able to achieve quantitative results using the elemental sensitivity method in XRF (Greaves et al., 1992). Excitation of thick homogenous pellets of the standard sample of the several elements or compounds can be used to achieve this. The sensitivity, S_i was calculated using the equation (3.16)

$$S_i = \frac{I_i(E)a(E)}{C_i}$$

$I_i(E)$ is evaluated fitted X-ray intensity, $a(E)$ is absorption factor of the standard, C_i is the concentration of the standards

The $a(E)$ and C_i were calculated using values in Table 4 and X-ray intensity in the standard was evaluated using the AXIL spectrum deconvolution.

Sensitivity curves were developed with standards. Twenty-five (25) standards were used. These elements were selected to cover the maximum range of energy of REEs. K_α -lines and L_α -lines are treated separately for Ag- anode X-ray tubes spectrometer.

The sensitivity calibration (Figure 20 and Figure 21) was done for both the EXP-1 and Am-241 excitation-based system using *S, Cl, K, Ca, Ti, Cr, Mn, Fe, Co, Ni, Cu, Zn, As, Br, Sr, Mo, Ag, Cd, Sn, I, Cs, Ba, W, Hg, and Pb*

The respective concentrations of the various standards are shown in Table 4. The "Elemental sensitivities method" determines the sensitivity of characteristic lines from standards, taking self-absorption in the standards into account.

Table 4: Standards with Their Respective Concentrations for Sensitivity Calibration

COMPOUND	ELEMENT	CONCENTRATION (%)	CONCENTRATION OF OTHER ELEMENTS (%)
$CaCO_3$	Ca	39.643	C = 11.880, O = 47.476
$CoCO_3$	Co	49.301	C = 10.048, O = 40.152
$NiCO_3$	Ni	49.396	C = 10.108, O = 40.394
ZnO	Zn	79.536	O = 19.463
AS_2O_3	As	75.588	O = 24.212
Cr_2O_3	Cr	68.414	O = 31.576
$FeCO_3$	Fe	47.720	C = 10.263, O = 41.015
$MnCO_3$	Mn	47.316	C = 10.344, O = 41.338
MoO_3	Mo	66.654	O = 33.346
$Sr(NO_3)_2$	Sr	40.988	N = 13.104 O = 44.906
$CuCO_3$	Cu	50.919	C = 9.624, O = 38.460
KBr	Br	66.474	K = 32.523
$KHCO_3$	K	38.663	H = 0.100, C = 11.877, O = 47.462
-	S	32.06	-
-	Ti	47.8	-
$NaCl$	Cl	60.059	Na = 38.946
$AgNO_3$	Ag	63.373	N = 8.229, O = 28.199
BaO	Ba	87.772	O = 10.226
$CsNO_3$	Cs	66.142	N = 6.971, O = 23.886
CdO	Cd	87.540	O = 12.460
$HgCl_2$	Hg	73.138	Cl = 25.853
HIO_3	I	71.781	H = 0.57, O = 27.149
PbO	Pb	91.903	O = 7.096
-	Sn	99.00	--
WO_3	W	79.297	O = 20.703

Am-241 $K\alpha$ -Sensitivity Curve

The standard samples used to calculate $K\alpha$ - sensitivity curve and their fitted intensity values of the respective elements are shown in *Table 5* below:

Table 5: Standards used in the $K\alpha$ -Sensitivity Curve and Their Fitted Intensity Values

Atomic Number (Z)	Elements	$K\alpha$ -Energy keV	Intensity Values (cps)
20	Ca	3.691	5.69E+07
22	Ti	4.510	8.89E+07
24	Cr	5.414	1.25E+08
26	Fe	6.403	1.57E+08
28	Ni	7.477	1.90E+08
29	Cu	8.047	2.23E+08
30	Zn	8.638	2.59E+08
33	As	10.543	2.92E+08
35	Br	11.923	3.10E+08
42	Mo	17.478	2.12E+08
47	Ag	22.162	2.11E+08
48	Cd	23.172	2.23E+08
50	Sn	25.270	2.37E+08
53	I	28.610	2.54E+08
55	Cs	30.970	2.60E+08
56	Ba	32.191	2.50E+08

A typical plot of sensitivity fitted standard (Fe) is shown *Figure 19*

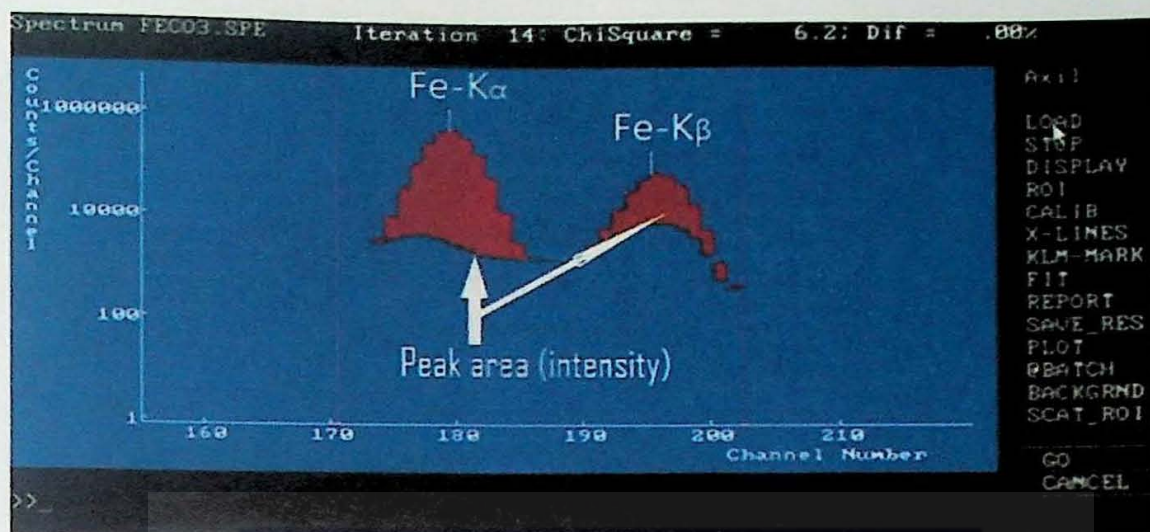


Figure 19: A plot of fitted Fe-standard for sensitivity calculation showing the peak area

The plot of the calculated $K\alpha$ -sensitivities are shown in Figure 20. The polynomial fit of the calculated $K\alpha$ -sensitivities generated the sensitivity (Y) is equation (4.1)

$$Y = A_0 + A_1 * Z + A_2 * Z^2 \quad (4.1)$$

$$A_1 = 2.5690E+003 \pm 2.6389E+002$$

$$A_2 = -4.0484E+002 \pm 3.6936E+002$$

where Z is the atomic number

Equation (4.1) was used for the calculation of the various concentration in the unknown samples

It was observed that there was an increase in the $K\alpha$ -sensitivity values of the attached Am-241 excitation-based system with X-ray energy from calcium ($Z=20$) to molybdenum ($Z=42$) and drops sharply before it continues with further increase in sensitivity with energy. This sharp decline in sensitivity can be attributed to the two major energies emitted by Am-241 excitation-based source at 26.4 keV and 59.5 keV. Figure 2.5 shown the Am-241 decay scheme. The 26.4 keV is the prominent irradiation energy for the low-Z and

Mid-Z elements and 59.5 keV for the irradiation of the high-Z elements. This account for the two different trends shown in the $K\alpha$ -sensitivity curve of the attached Am-241 excitation-based system in (Figure 20)

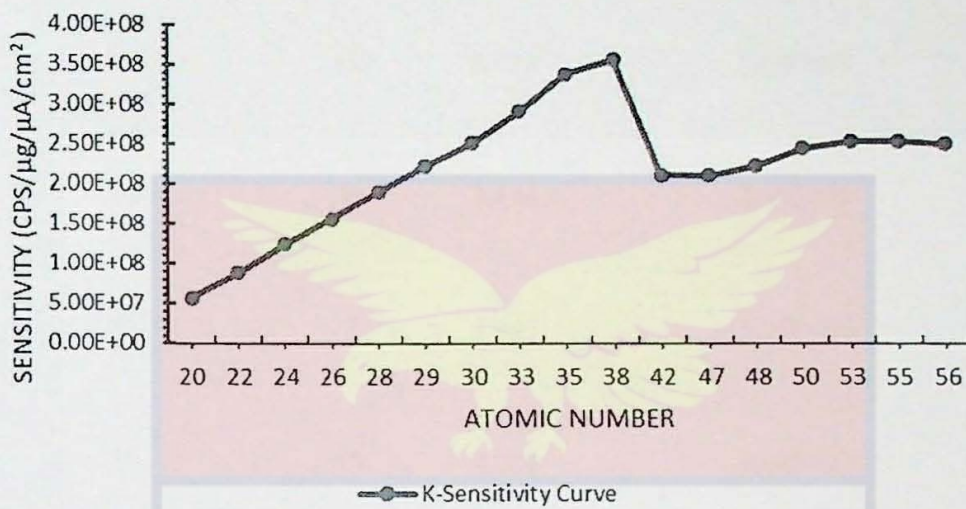


Figure 20: Am-241 $K\alpha$ -Sensitivity Curve.

X-ray Tube $L\alpha$ -Sensitivity curve

The standard samples used to calculate $L\alpha$ - sensitivity curve for the EXP-1 and their fitted intensity values of the respective element are shown in Table 6

Table 6: Standards used in the L α -Sensitivity Curve and their Fitted Intensity Values

Atomic Number (Z)	Elements	L α -Energy keV	Intensity Values (cps)
47	Ag	2.984	6.33E+06
48	Cd	3.133	7.12E+06
50	Sn	3.444	8.02E+06
53	I	3.937	2.26E+07
55	Cs	4.286	4.64E+07
56	Ba	4.467	6.67E+07
80	Hg	9.987	8.64E+07
82	Pb	10.549	1.06E+08

The calculated sensitivities were plotted and the graph are shown in Figure 21.

The polynomial fit of the calculated L α - sensitivities generated sensitivity (Y)

is equation (4.2)

$$Y = A_0 + A_1 * Z + A_2 * Z^2 \tag{4.2}$$

$$A_1 = 2.0629E^{+005} \pm 7.6907E^{+004}$$

$$A_2 = -2.1250E^{+004} \pm 8.1071E^{+003}$$

where Z is the atomic number

Equation (4.2) was used for the calculation of the various concentration in the unknown sample

For heavier elements, the L-line depicts an increase in sensitivity function, as shown in *Figure 21*. The sensitivity curve trends are comparable to those seen in Ivošević's study (Ivošević et al., 2014).

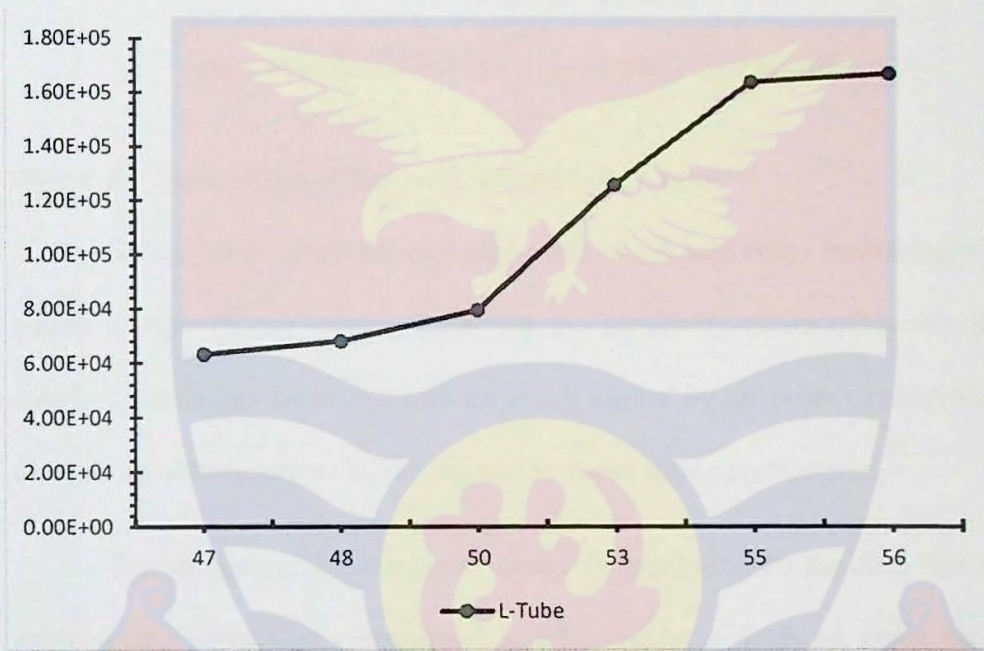


Figure 21: Ag-anode X-ray Tube $L\alpha$ -sensitivity curve.

Comparison of the Sensitivities of Am-241 excited based system with Ag_X-ray tube excited spectrometer

The sensitivity plot for the attached Am-241 excited-based system and Ag-anode X-ray tube spectrometer is shown in *Figure 22*.

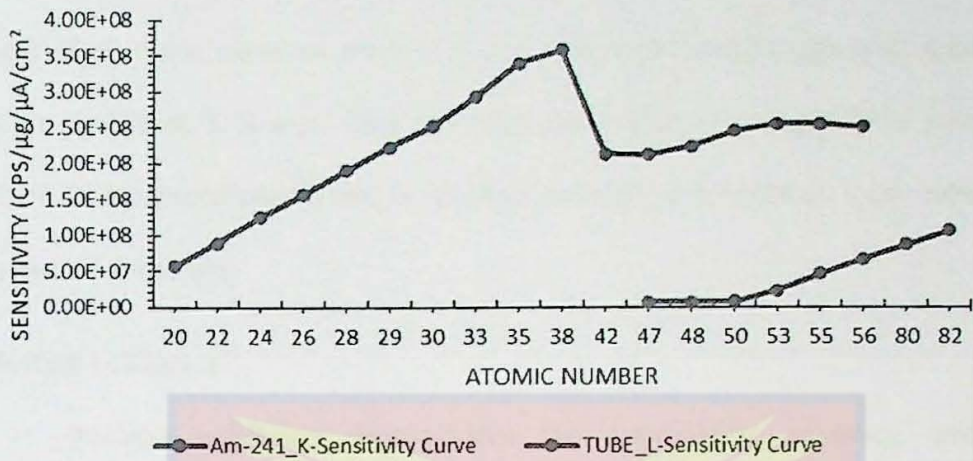


Figure 22: Comparison of $K\alpha$ and $L\alpha$ Sensitivity Curve.

Both systems show the expected trend of the sensitivity increasing with atomic number (X-ray energy). However, the sensitivity values of the attached Am-241 excitation-based systems are much higher by an order of magnitude than the sensitivity values of the Ag-anode X-ray tube spectrometer.

The difference in sensitivity could be attributed to the fact that the photoelectric absorption probabilities and fluorescence yields are much higher for K-X-rays as compared to L-X-rays. Therefore, X-ray fluorescence intensity for $K\alpha$ X-rays is consequently higher than the $L\alpha$ X-rays. The attached Am-241 excitation-based system can analyse a wider range of elements (From Ca at energy of 3.691 keV to Gd at energy of 42.983 keV) than the Ag-anode X-ray tube spectrometer (K at energy 3.313keV to Mo at energy 17.478 keV). This limitation with the X-ray tube spectrometers is due to the fact that the Ag- anode X-rays of 22.1 keV cannot excite the K-X-ray of the REE when one is using the X-ray tube excitation system. Then REE can only be analysed with their L-X-ray spading from 4.650 to 7.654 keV.

Unfortunately, this range of energies falls within the K-x-rays for the elements from Ti to Cu. Consequently, in the addition to the much lower sensitivity of the L-X-rays, the elements from Ti to Cu will cause interference with their much prominent K-X-rays. This will have an impact on the precision with which REE concentrations can be determined using a traditional X-ray tube excitation technique.

Method validation

Method validation demonstrates the consistency, accuracy, and precision of the data obtained with the attached Am-241 excitation-based system and the EXP-1 at GAEC's XRF laboratory.

Repeatability/Precision of the attached Am-241 excitation-based system and EXP-1, was measured using BaO standard which was irradiated before, during and after sample irradiations. A reasonable amount of data was generated and presented in *Table 7* below.

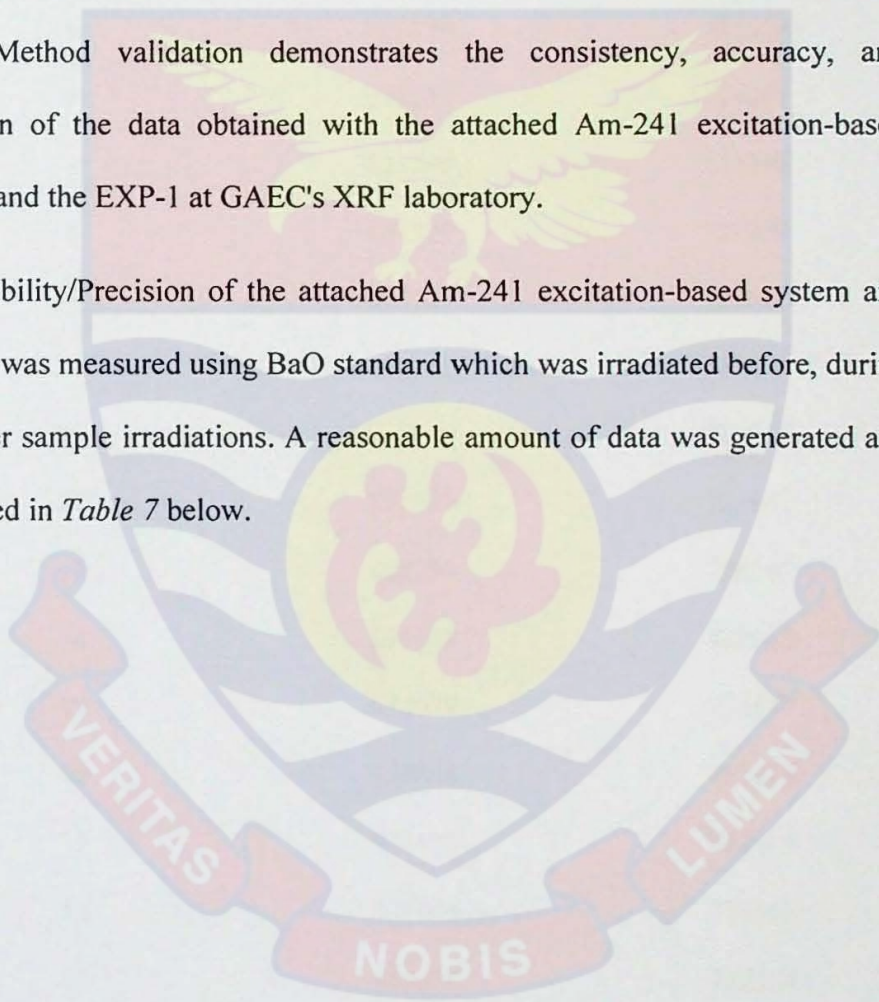


Table 7: Testing the Repeatability/Precision of Am-241 and Ag-X-ray Tube EDXRF Spectrometer

Number of irradiations	Intensities	
	Am-241 EDXRF	Ag-X-ray tube EDXRF
1	827390	827390
2	827296	727296
3	827863	727863
4	820560	720560
5	822379	722379
6	821215	721215
7	821396	721396
8	827329	727329
9	811683	711683
10	825572	725572
11	827116	727116
12	822685	722685
13	828299	728299
14	829143	729143
15	832577	732577
16	835838	735838
17	832428	732428
18	836666	736666
19	832234	732234
20	833413	733413
21	835571	735571

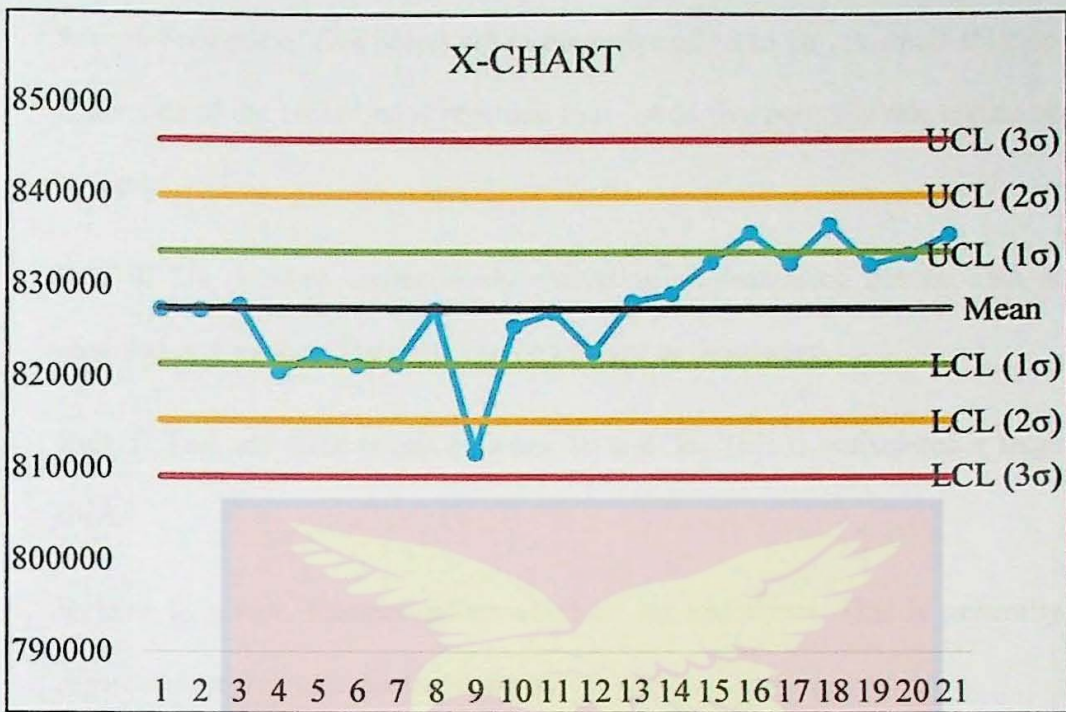


Figure 23: The control chart that shows the mean, standard deviation, lower and upper control limit for the Am-241 EDXRF system.

The control chart (see Figure 23) establishes the precision of an analytical technique (Durivage, 2021). To find out whether the attached Am-241 excited-based system at the GAEC was in statistical control, a control chart was generated using a Barium Oxide (BaO) as a control sample. The interpretation of the control chart based on the Shewhart rules suggests that the spectrometer was under statistical control (variation is consistent).

The seven (7) rules of the Shewhart control chart are;

Rule 1: One point is beyond the 3σ limit. This aims to find points that are outliers or random.

Rule 2: There must be at least eight points on one side of the centerline without crossing it. This is a significant shift that can occur on either side of the centerline.

Rule 3: Four out of five points are in the range of 1σ to 2σ . A small shift on either side of the centerline is regarded four out of five points in this region or beyond.

Rule 4: Six or more consecutively ascending or decreasing points. This is regarded as a pattern. The trend can be upward or downward.

Rule 5: Two out three points between 2σ and 3σ . This is considered a large shift.

Rule 6: In a row, fourteen points alternate up and down. This is generally regarded as a case of excessive control.

Rule 7: Any pattern, cycle, or trend that is visible or predictable. Such points are regarded as uncontrollable.

The outcome of these rules may be attributed to;

- (i) Proper setup of the equipment
- (ii) Environmental conditions among others.

IAEA Soil 7 (reference material) was used to test the accuracy of the attached Am-241 excitation-based system. *Figures 24 and 25* show the results of the XRF study, whereas *Figure 26* shows the results of the INAA analysis. The concentrations of these reference materials were recalculated using equations from the sensitivity curve.

When compared to the certified values, the calculated findings indicated a high level of consistency (see *Table 8*). The accuracy of the developed method was further confirmed by an INAA (validated primary method) study of the same standard (see *Table 8*).

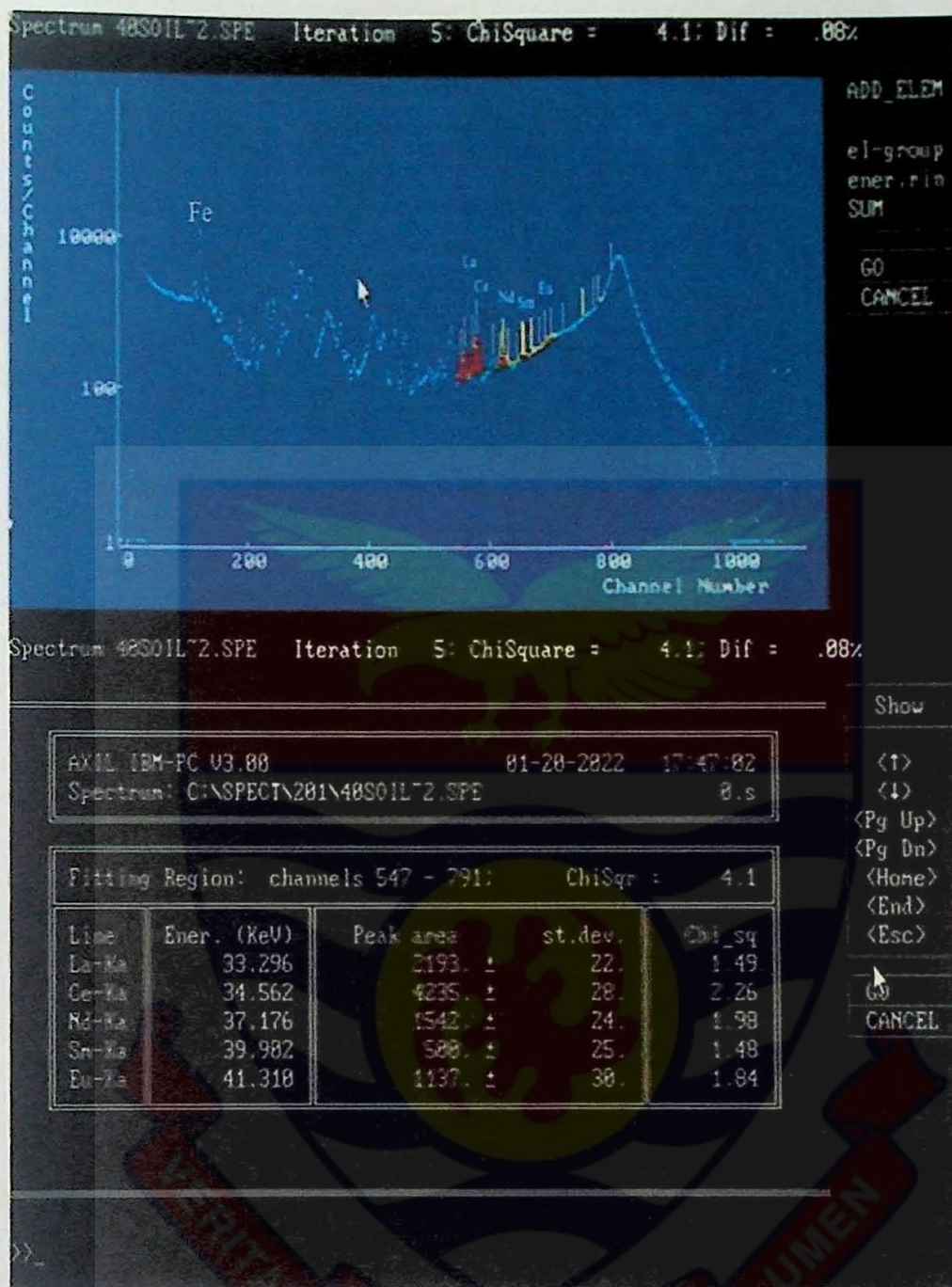


Figure 24: Fluorescence Spectrum of the various REEs in IAEA-Soil 7 with Am-241 EDXRF and their Peak areas.

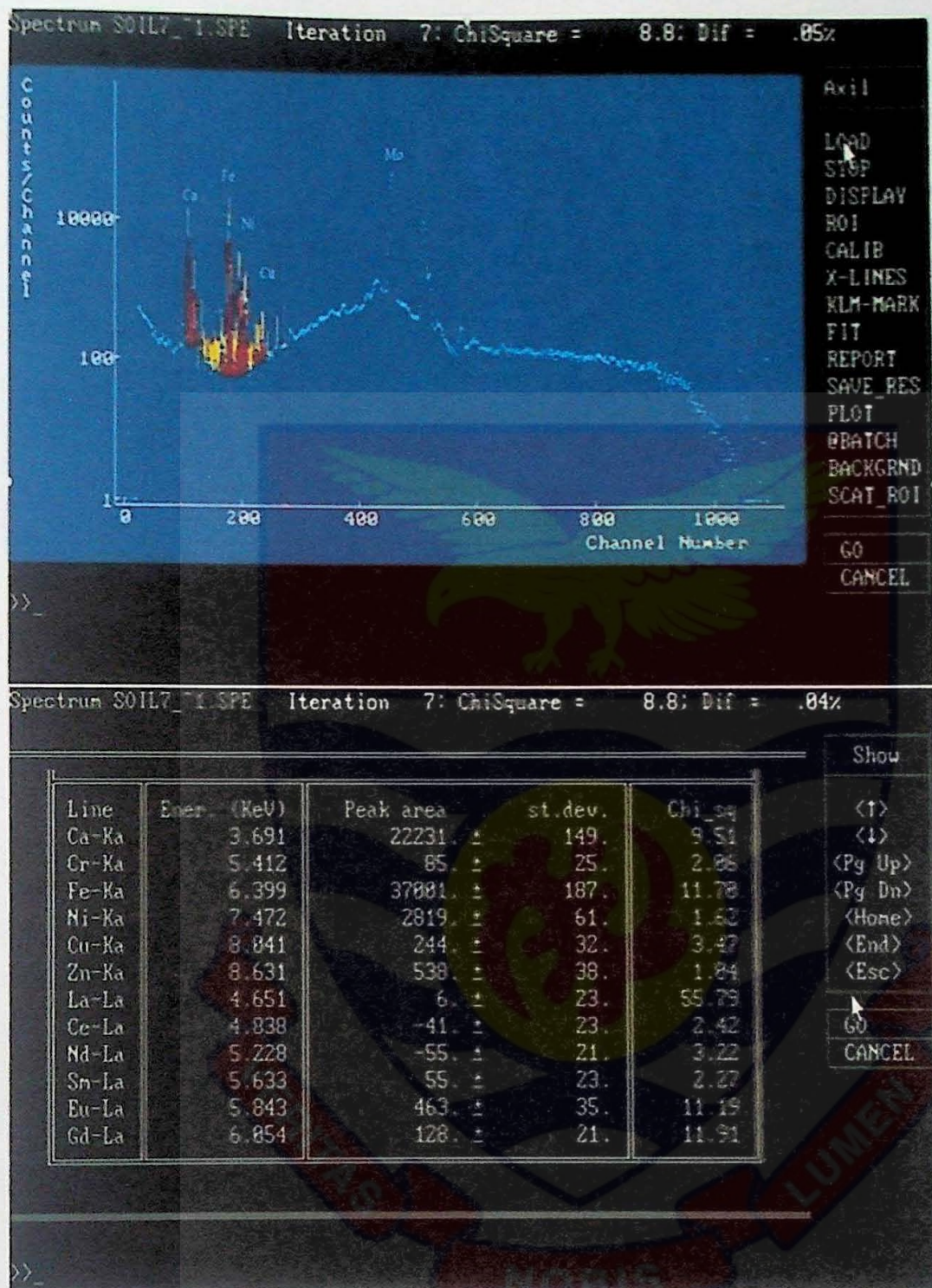


Figure 25: Fluorescence Spectrum of the various REEs in IAEA-Soil 7 with Ag-tube EDXRF and their Peak areas.

The IAEA-Soil 7 sample were measured with EXP-1(without the attached Am-241 excitation-based source) and the attached Am-241 excitation-based system using the elemental sensitivity method. Energy peaks for each element were found in the resulting energy spectrum (see Figures 24 and 25). Using

the QXAS-AXIL program, using equation 3.16, the area under each peak was processed to calculate the concentration of each element identified in each sample. The elements identified with EXP-1 were Scandium (Sc), yttrium (Y) and Europium (Eu) also elements identified with attached Am-241 excited-based system are Lanthanum (La), Cerium (Ce), Neodymium (Nd) and Europium (Eu)

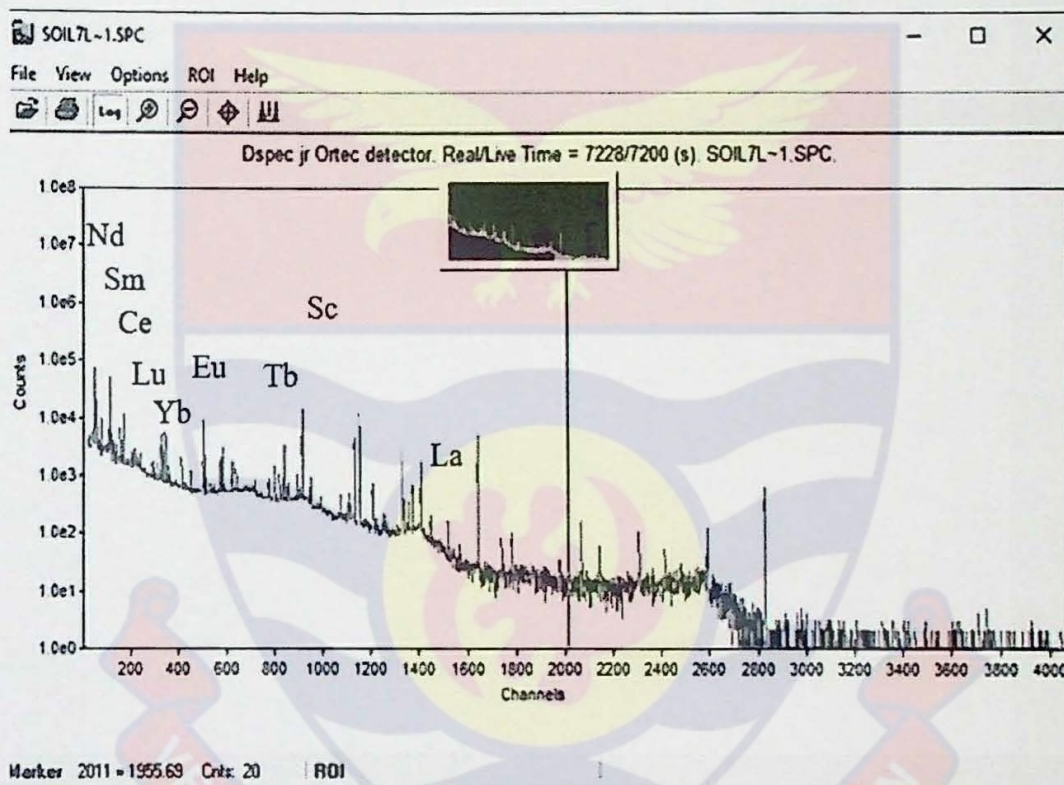


Figure 26: Analysis of REEs in Sample Soil7 with INAA.

The IAEA-Soil 7 sample has been measured using INAA method. The energy peaks for each element was found in the resulting energy spectrum (see Figure 26). Using the Ko-IAEA program, using equation (4.2), the concentration of each element seen in each sample was calculated using the area value under each peak (intensities). The elements which were identified from the INAA technique were Scandium (Sc), Lanthanum (La), Cerium (Ce),

Neodymium (*Nd*), Samarium (*Sm*), Europium (*Eu*), Terbium (*Yb*) and Lutetium (*Lu*).



Table 8: Accuracy and Standard Deviations

Elements	Soil 7 (REEs Elements) Expected value (mg/kg)	Ag-Tube XRF measurements			Am-241 XRF Measurement			INAA Measurements		
		Observed value	Accuracy	SD	Observed value	Accuracy	SD	Observed value	Accuracy	SD
		(mg/kg)	(%)	(mg/kg)	(mg/kg)	(%)	(mg/kg)	(mg/kg)	(%)	(mg/kg)
Sc	8.3±5.2	8.3± 5.2	100.0	5.2	8.1 ± 2.5	98.0	2.5	9.44 ±1.3	114	1.3
La	28.0±1				27.5±3.8	98.2	3.8	27.2±1.1	97	1.1
Ce	61.0±6.5				60.5 ±2.5	99.2	2.5	60.4±2.3	99	2.3
Nd	30.0±6				30.4 ±3.0	101.3	3.0	30.7±1.2	102	1.2
Sm	5.1±0.35				4.6±2.0	90.2	2.0	4.38 ±0.25	86	0.25
Eu	1.0±0.2	1.2± 3.8	120	3.8	0.9 ±2.7	110.0	2.7	0.88±0.05	88	0.05
Tb	0.6±0.2							0.74 ±0.03	117	0.03
Yb	2.4±0.35	5.1 ±13.4	87	13.4				2.34±0.09	96	0.09
Lu	0.3±0.1	-			-			0.34 ±1.3	113	1.3

Source: Field Data, 2021

N=triplicate sample

SD= standard deviation

Application in Rare Earth Elements Analysis

The developed quantitative methods were applied to the analysis of REEs in volcanic rocks (DK6, DK7 and DK8) in the Dahomeyide orogenic belt, southeastern Ghana, West Africa (Nude et al., 2015). These rock samples were obtained from the Earth Science department of the University of Ghana which had already been measured using ICP-MS from Canada (Nude et al., 2015). The same rock samples were processed through the stages of crushing, grinding, sieving, pressing, and finally forming the pellet. Three replicate each of these samples were analysed using the attached Am-241 excitation-based EDXRF system, Ag-anode X-ray tube spectrometer and INAA at GAEC. The energy peaks for the elements represented in the obtained energy spectrum were analysed (see *Figures 27-29*). The fluorescence X-ray intensity of the identified elements was evaluated using the spectrum deconvolution methods of the IAEA-AXIL software. The concentration values of the elements were calculated using the elemental sensitivities methods as shown in equation (3.16).

The three samples have been measured using the elemental sensitivity method for Ag-anode X-ray tube spectrometer. The energy spectrum that resulted was examined for energy peaks for the elements it represented (see *Figures 27-29*). Using the QXAS-AXIL software and equation (3.16), the area value under each peak was used to calculate the concentration of each element observed in each sample.

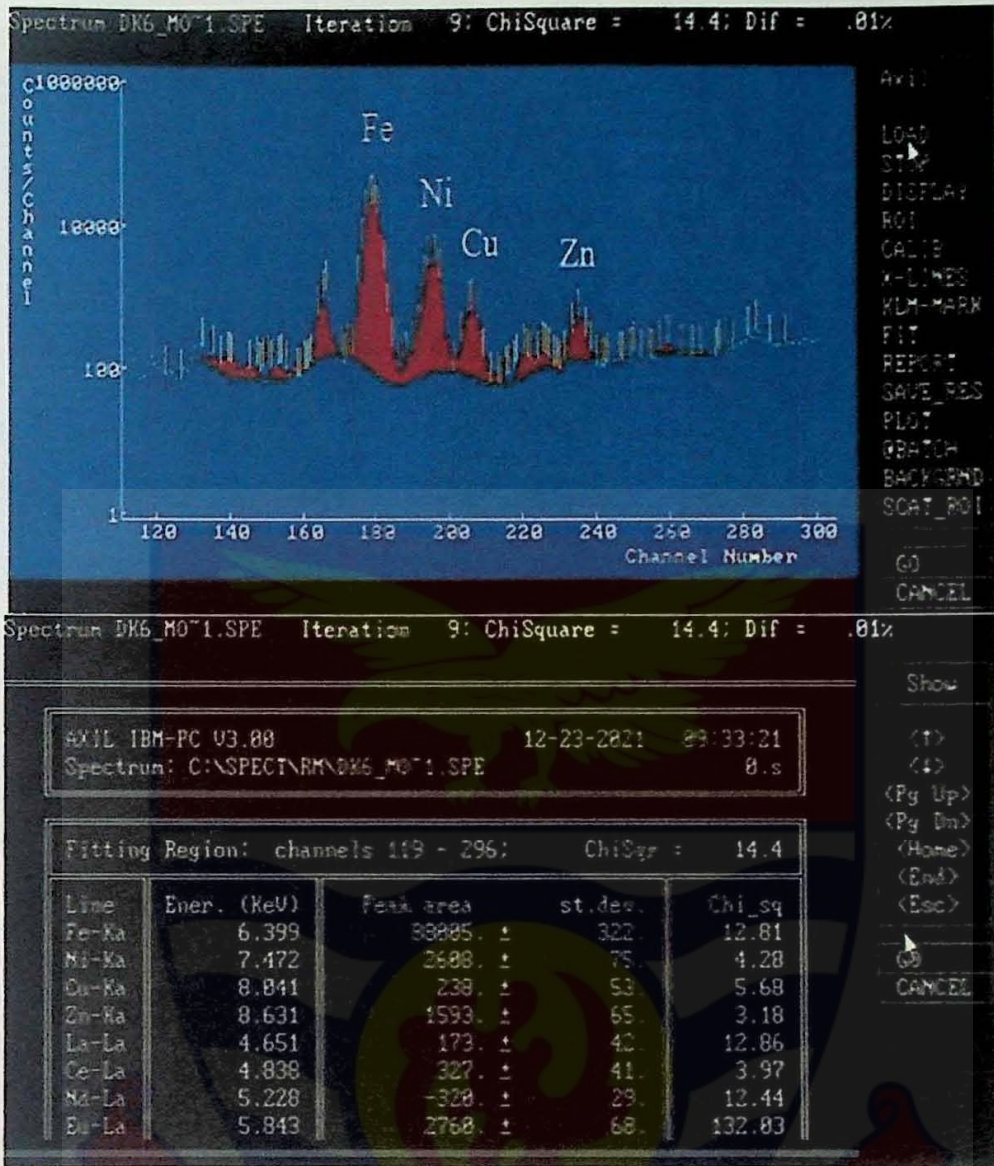


Figure 27: Fluorescence Spectrum of the various REEs in sample DK6 with Ag-tube EDXRF and their Peak areas.

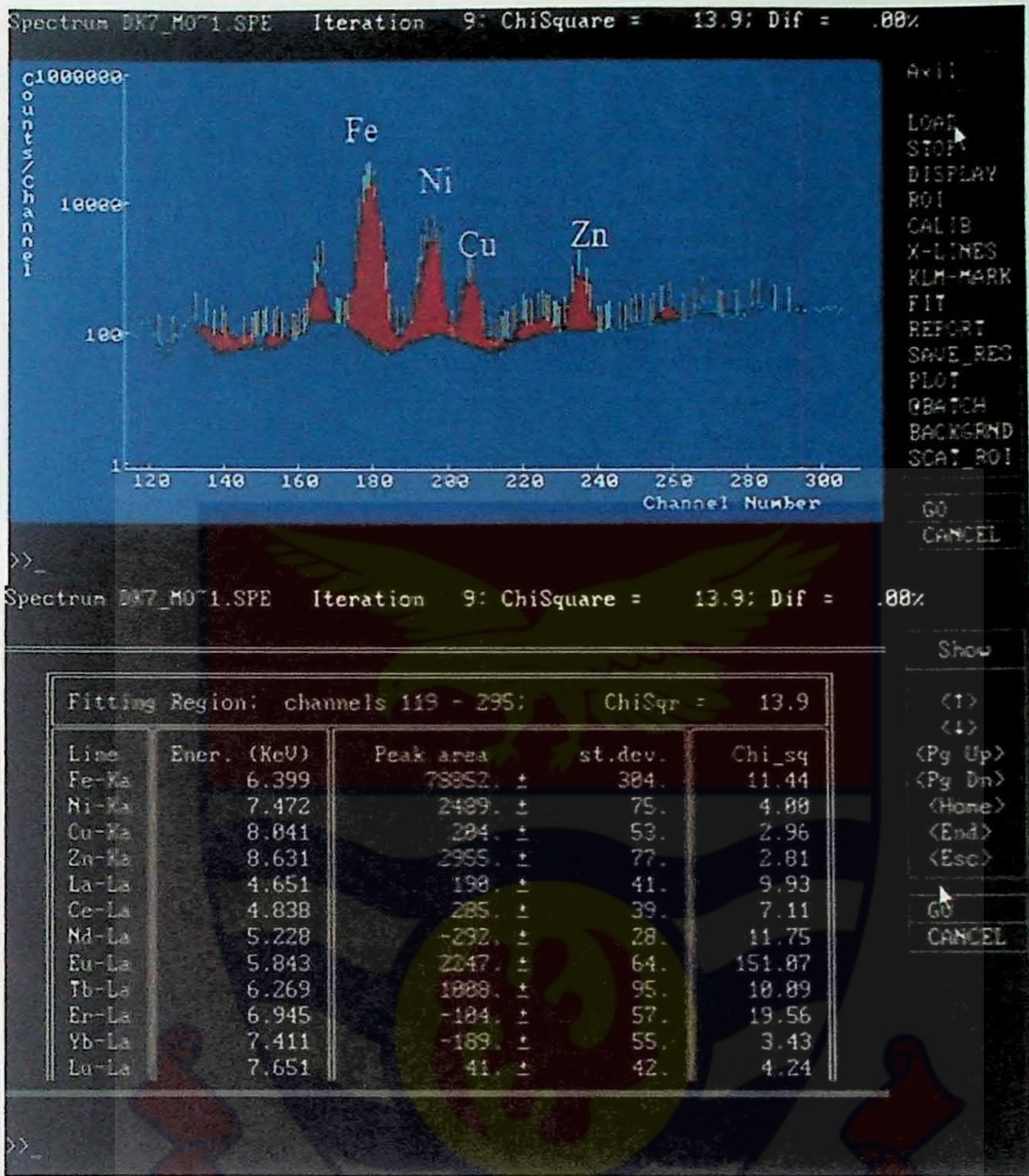


Figure 28: Fluorescence Spectrum of the various REEs in sample DK7 with Ag-tube EDXRF and their Peak areas.

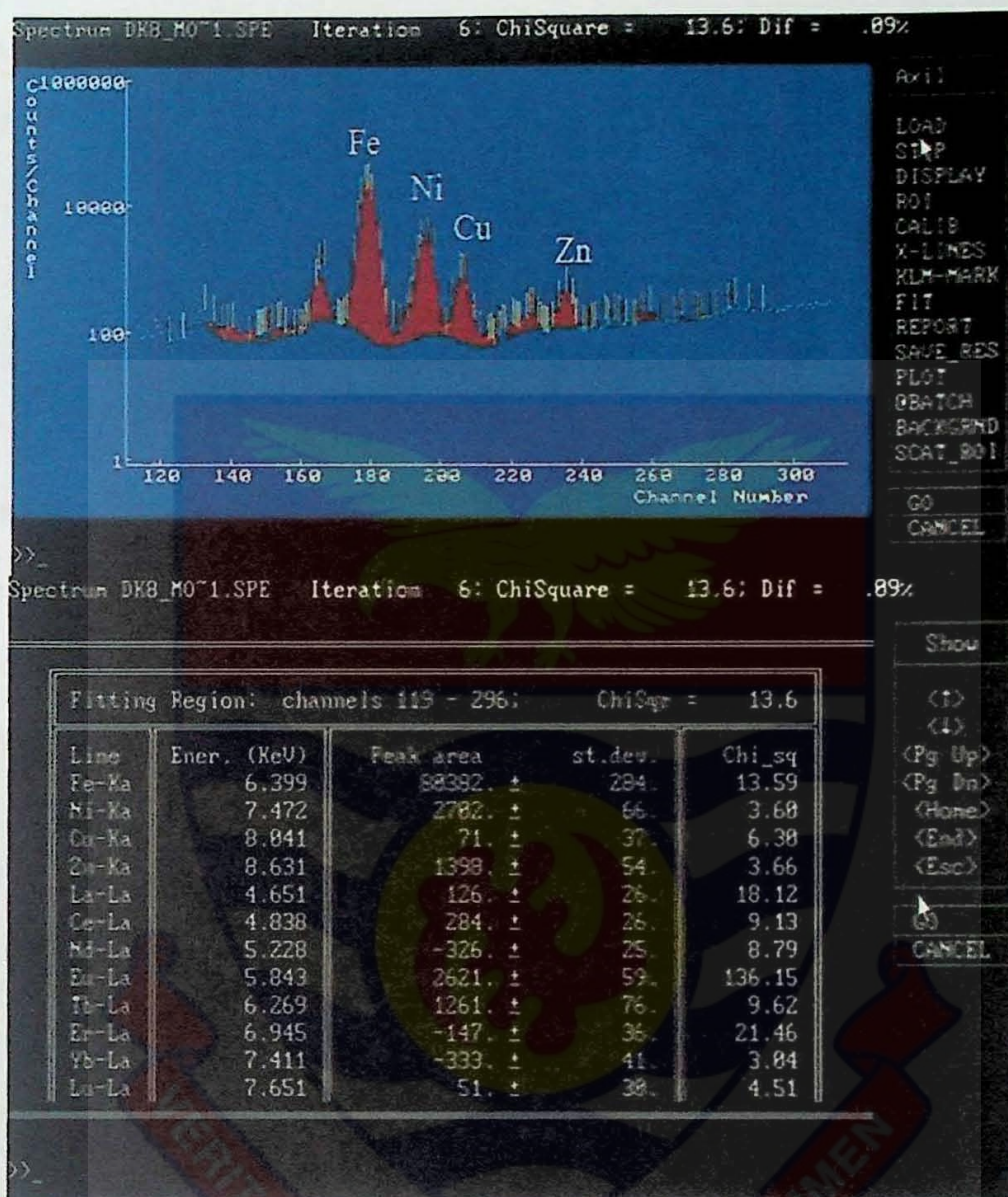


Figure 29: Fluorescence Spectrum of the various REEs in sample DK8 with Ag-tube EDXRF and their Peak areas.

The mass concentration of the REE was calculated using equation (3.16). The photoexcitation was carried out using the incident source energy of the Ag anode, which was 22.1 keV. For each element, the description of the recognized elements peaks (see Figures 30-32). Lanthanum (La), Cerium (Ce), and Europium (Eu) were discovered using this Ag anode X-ray tube

spectrometer technique for a Sample DK6: Lanthanum (*La*), Cerium (*Ce*), Europium (*Eu*), and Terbium (*Tb*) are the elements used in sample DK7: Lanthanum (*La*), Cerium (*Ce*), Europium (*Eu*), and Terbium (*Tb*) are the elements used in sample DK8

The same three samples each have also been measured using the elemental sensitivity method for the attached Am-241 excitation-based system. The resulting energy spectral were analysed for energy peaks for their corresponding elements (see *Figure 30-32*). Using the QXAS-AXIL software to calculate the concentration of each element found in each samples based on equation (3.17).



Figure 30: Fluorescence Spectrum of the various REEs in sample DK6 with Am-241 EDXRF and thier Peak areas.

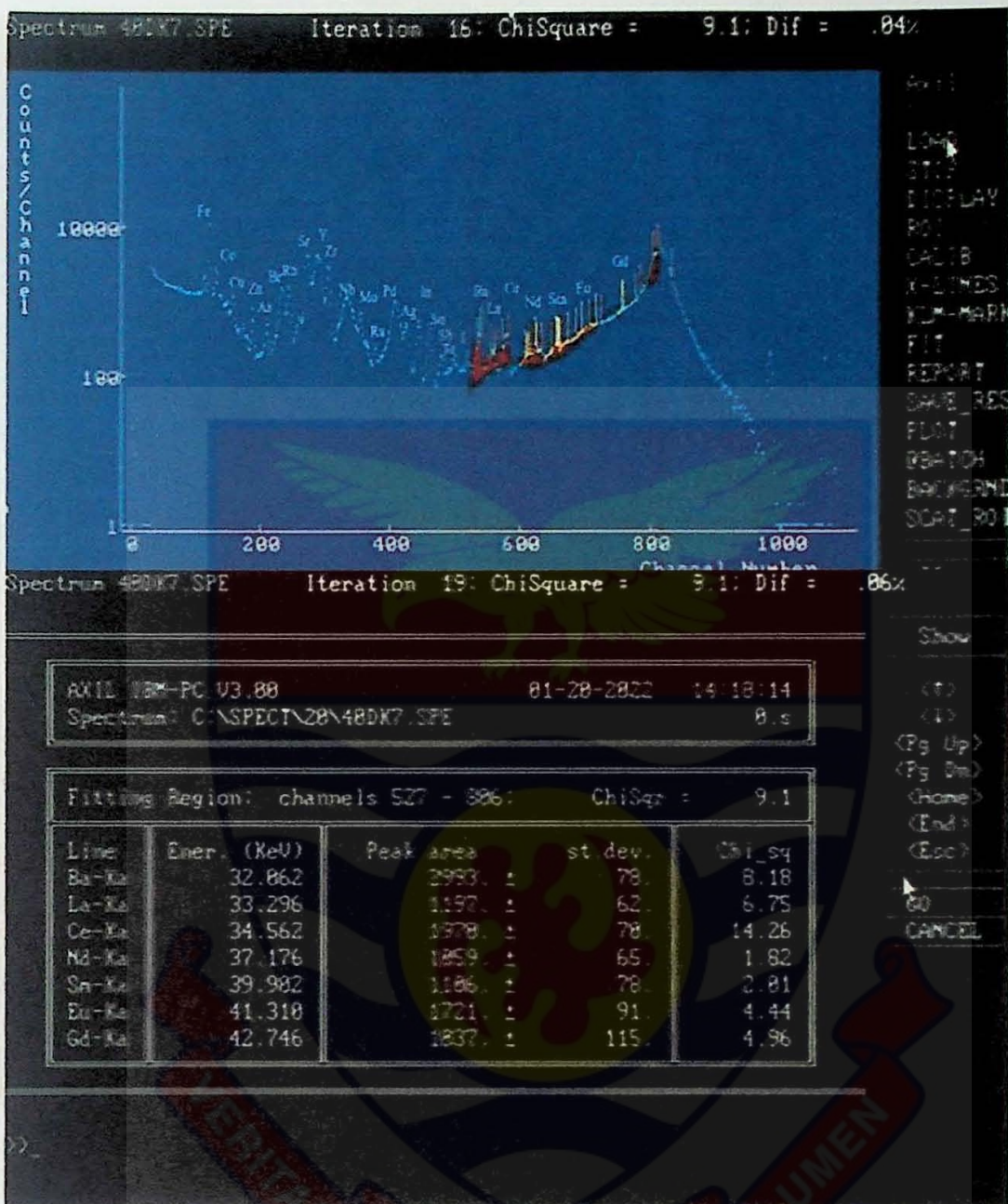


Figure 31: Fluorescence Spectrum of the various REEs in sample DK7 with Am-241 EDXRF and their Peak areas.

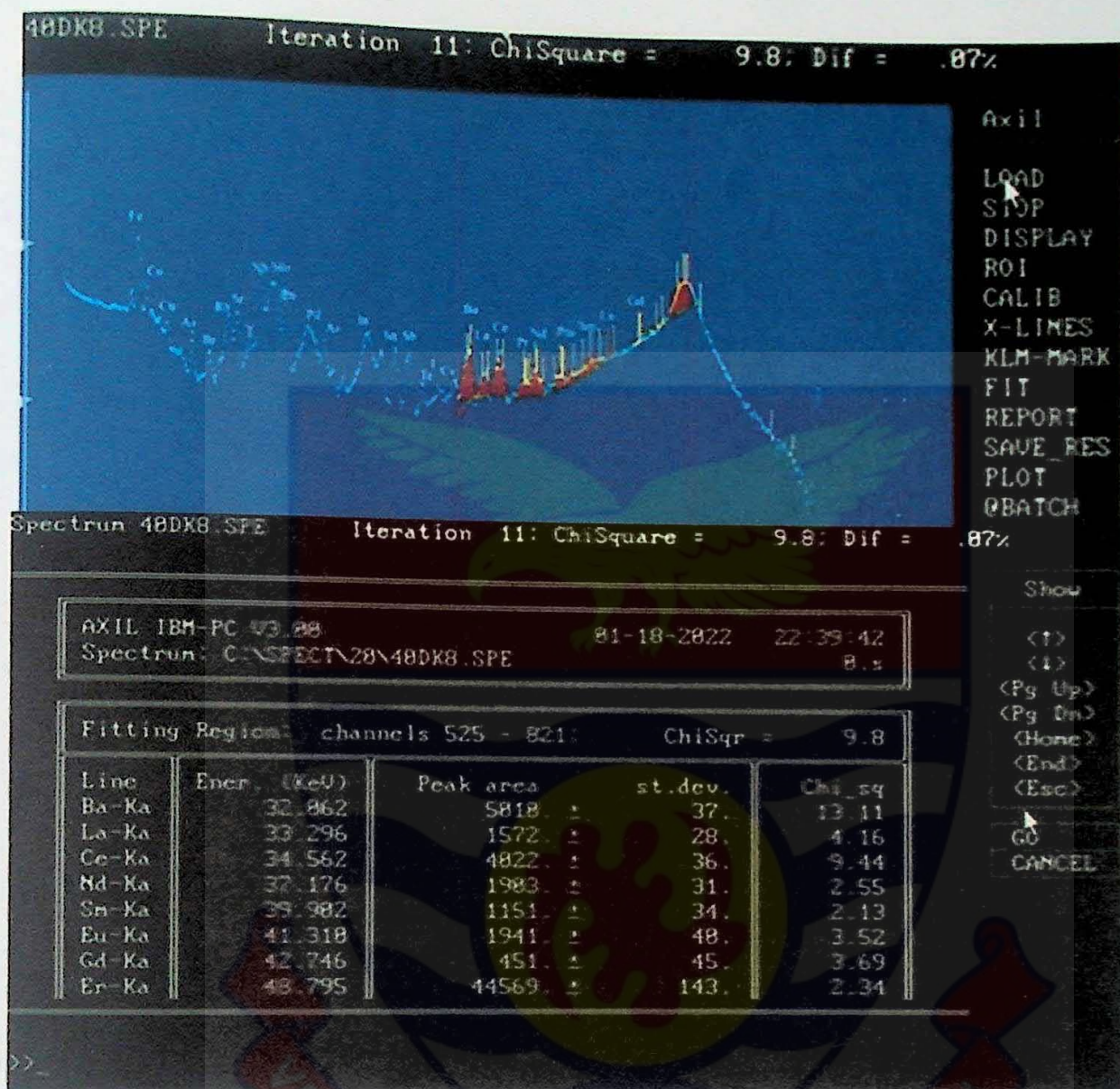


Figure 32: Fluorescence Spectrum of the various REEs in sample DK8 with Am-241 EDXRF and their Peak areas.

The REE concentrations were determined using equation (3.17)

The mass concentration of the REE was calculated using equation (3.16). The photoexcitation was carried out using incident source energies of 59.5 keV and 26.4 keV for Am-241. For each element, the description of the recognized elements peaks (see Table 3.1). Scandium (*Sc*), Lanthanum (*La*), Cerium (*Ce*), Europium (*Eu*), Neodymium (*Nd*), Samarium (*Sm*), and Gadolinium (*Gd*)

were discovered in DK6, DK7, and DK8 samples using the Am-241 EDXRF technique. Only DK8 has an extra Erbium (*Er*) atom.

The same samples had previously been subjected to ICP-MS analysis at the Analytical Facility System (ALT) laboratory in Vancouver, Canada (Nude et al., 2015). The Ghana Atomic Energy Commission used the Low Enriched Uranium Miniature Neutron Source Reactor to analyze the identical samples with INAA (LEU-MNSR). The energy peaks for their associated elements were found in the resulting energy spectrum (see *Figures 33-35*). The Ko-IAEA software was used to calculate the concentration of each element found in each sample based on the area value under each peak, used to calculate the concentration of each element identified in each sample.

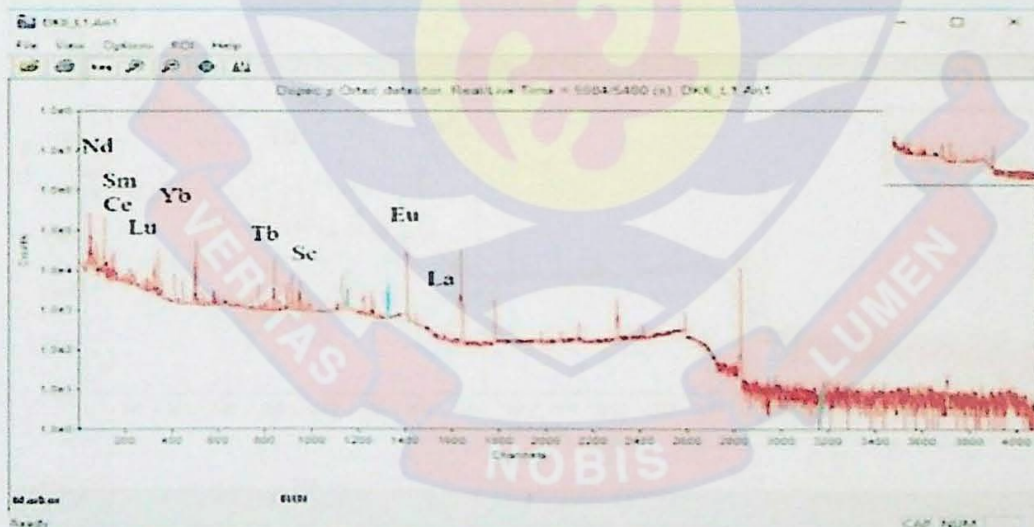


Figure 33: Graph that shows INAA analysis results of REEs in sample DK6.

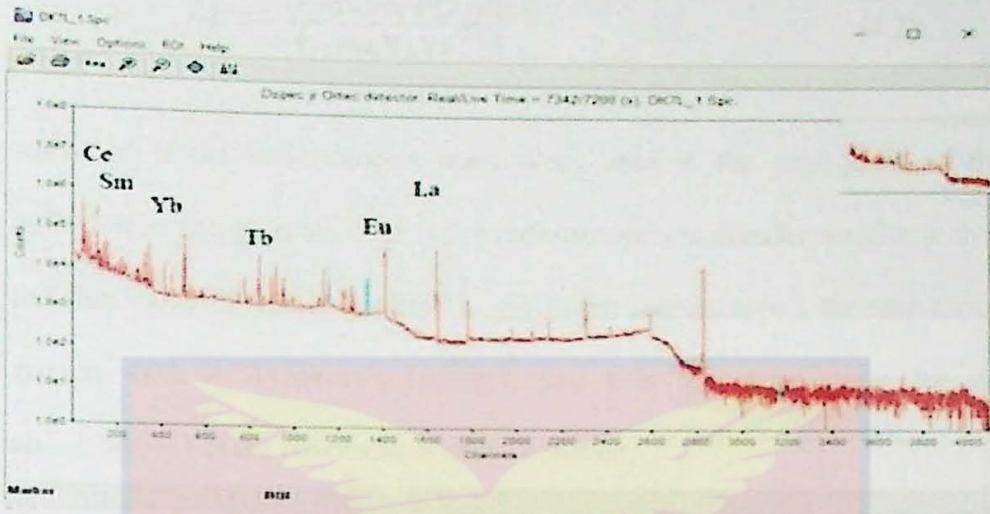


Figure 34: Graph that shows INAA analysis results of REEs in sample DK7.

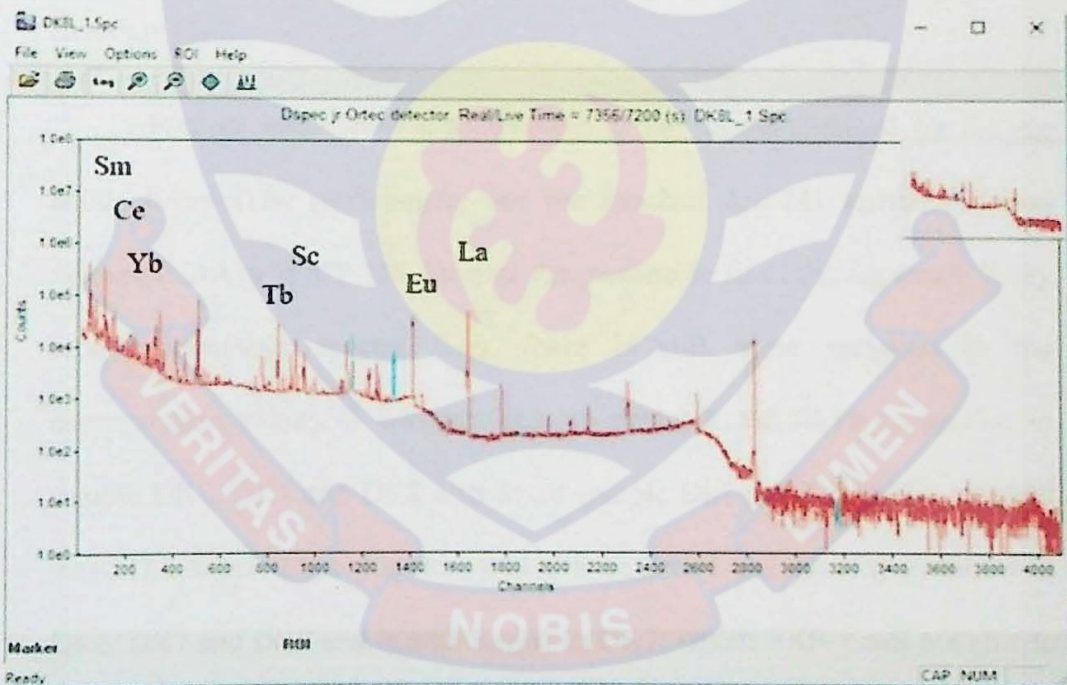


Figure 35: Graph that shows INAA analysis results of REEs in sample DK8.

The equation (4.2) could be used to connect the mass of REEs to the concentration of each element identified in the energy spectrum (see Figures 33-35).

$$M = \frac{(\text{Peak area})(A_{rel})}{\phi_{th} \sigma_{th} N_A V e^{-\lambda t}} \quad (4.2)$$

where M is the radioisotope's mass, Peak area is the peak area of the radioisotope energy peak, A_{rel} is the radioisotope's molecular weight, ϕ_{th} is the flux value of 4.3×10^{12} n/cm² s, σ_{th} is the radioisotope's thermal cross-section, N_A is Avogadro's Number, and t is the decay time for the radioisotope, λ is the radioisotope decay constant,

For samples DK6, DK7, and DK8, the elements found using the INAA approach are Scandium (*Sc*), Lanthanum (*La*), Cerium (*Ce*), Neodymium (*Nd*), Samarium (*Sm*), Europium (*Eu*), Terbium (*Tb*), and DK6 has a new element, Lutetium (*Lu*).

Figures 36-38 show a comparison of the results obtained for the Ag anode X-ray Tube spectrometer and the attached Am-241 excitation-based system, INAA, and ICP-MS. Despite the reasonable fit of the Ag anode X-ray tube spectrometer spectra lines, there is still some variation in the concentration values. It was not able to detect *Y, Nd, Gd, Tb, Yb, and Lu* in sample DK6, DK7 and DK8 also *Er* in sample Dk7 and DK8. The attached Am-241 excitation-based system was able to detect and quantify *Y, Nd, Gd* in DK6, DK7 and DK8 and in addition *Er* in DK7, which EXP-1 was not able to quantify in DK6, DK7 and DK8.

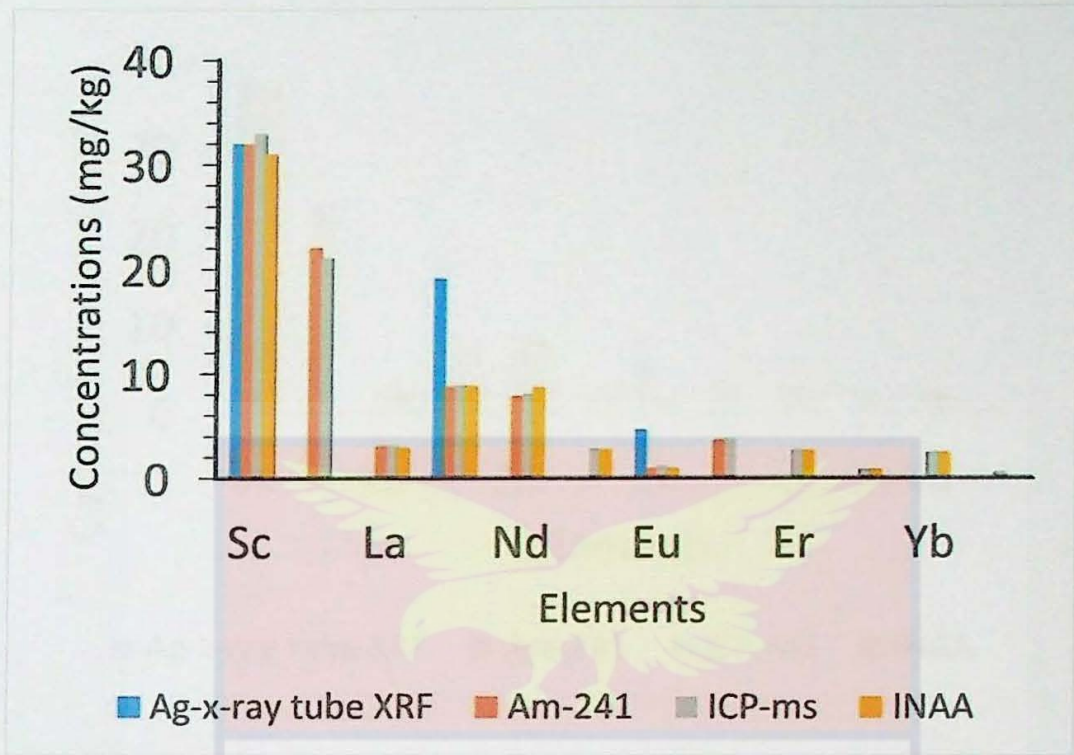


Figure 36: Graph that shows the concentrations of the REE in sample DK6.

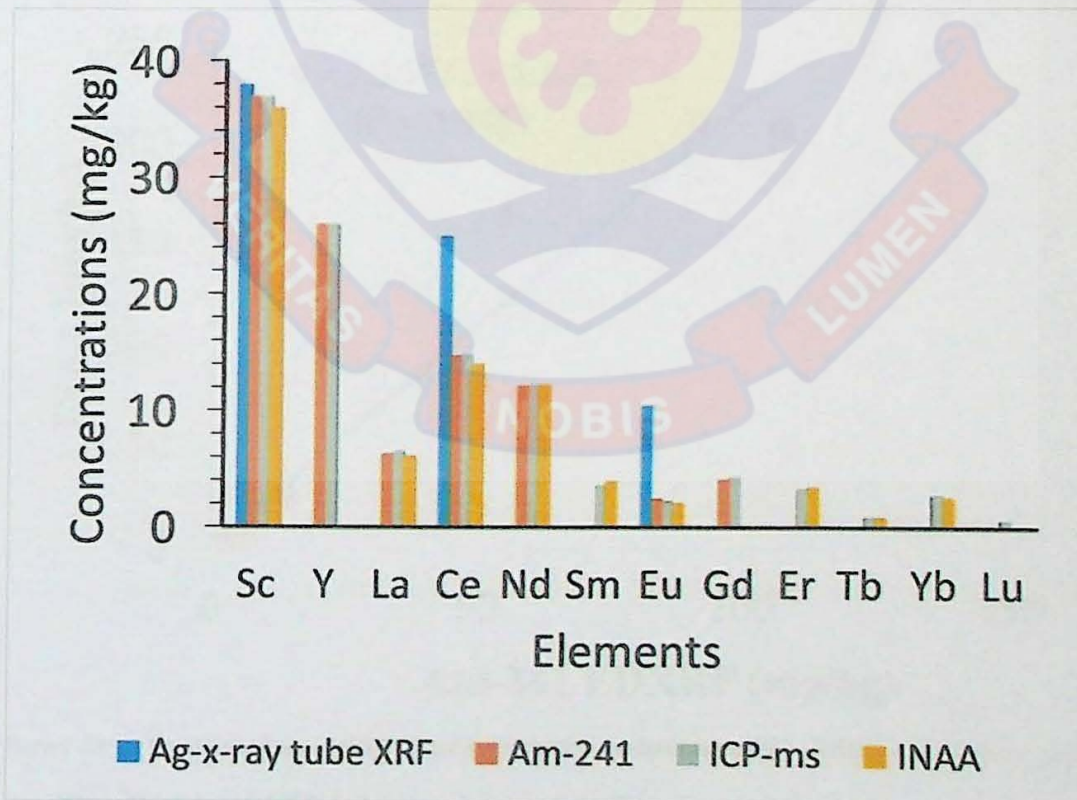


Figure 37: Graph that shows the concentrations of the REE in sample DK7.

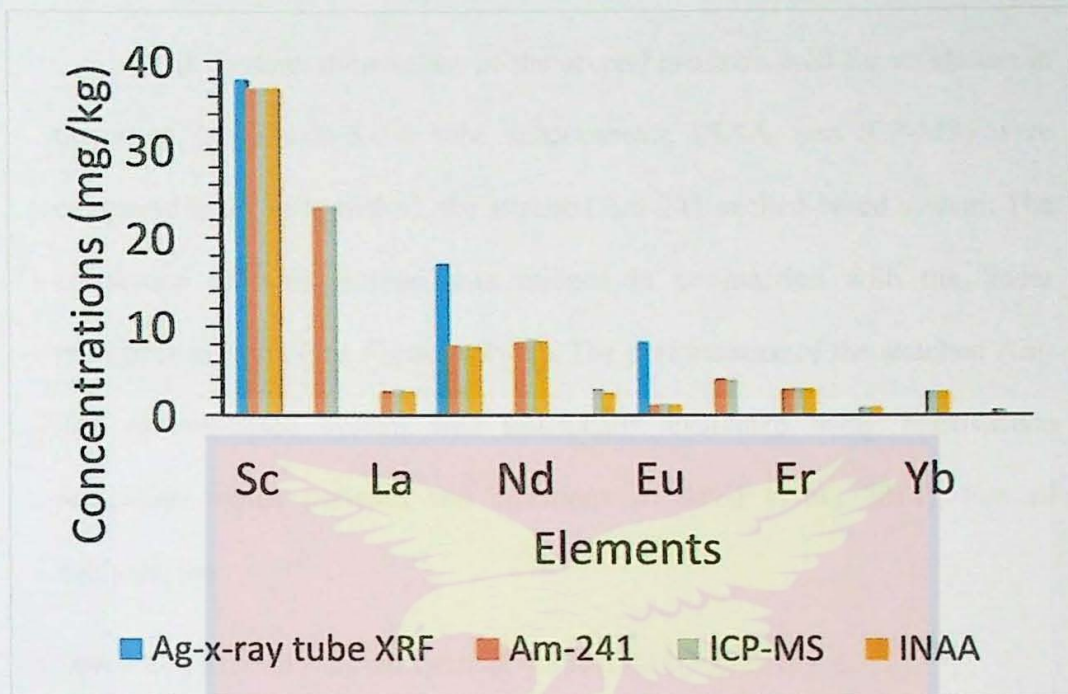


Figure 38: Graph that shows the concentrations of REE in sample DK8.

Comparison of Results from Am-241 EDXRF, Ag-Tube EDXRF, INAA and ICP-MS

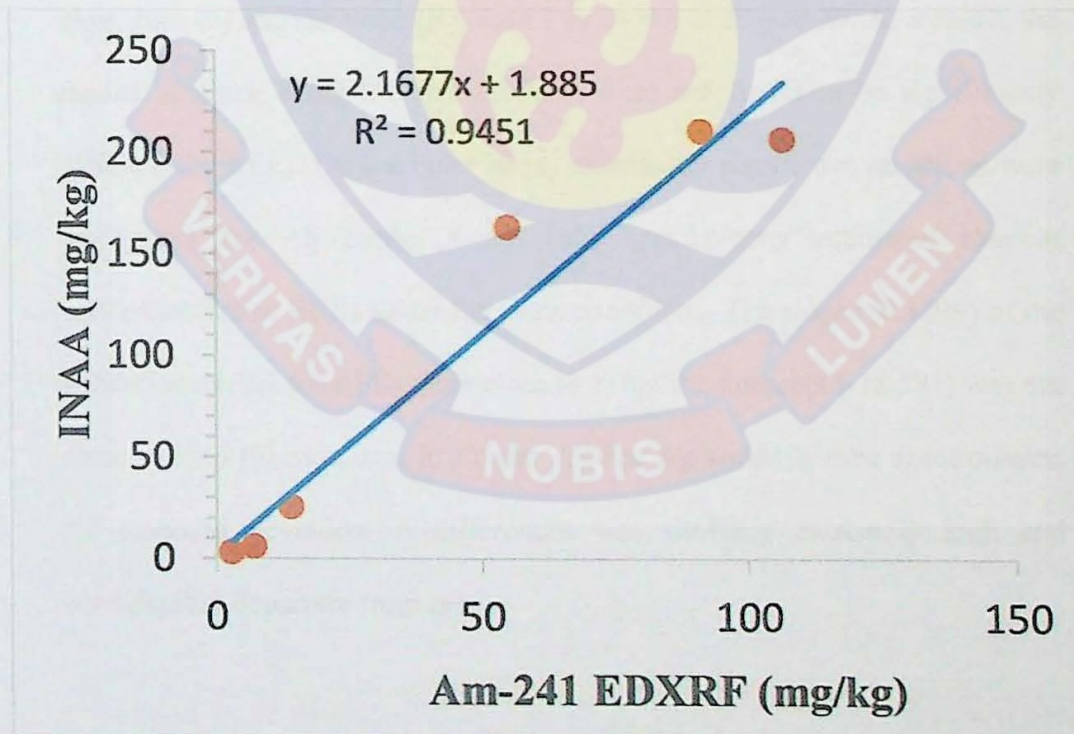


Figure 39: The graph shows a comparison between the results obtained for REEs with INAA and Am-241 excitation-based EDXRF, the correlation and R^2 values.

The concentration values of the several methods used for validation in this work (Ag anode-X-ray tube spectrometer, INAA, and ICP-MS) were compared to the new method, the attached Am-241 excited-based system. The correlation analysis method was utilized in conjunction with the linear regression method (see *Figures 39-42*). The performance of the attached Am-241 excited-based system was statistically evaluated using multivariate regression robust statistics and equations (Ivošević et al., 2014). For all analytes, the

$$\text{Am} - 241 \text{ excited} - \text{based system} = B \times [\text{INAA}(\text{mg/kg})] + A,$$

when the intercept (A) and slope (B) were calculated. $B = 1$ and $A = 0$ if the attached Am-241 excited-based system concentrations and the INAA concentrations of elements are consistent for REEs, the intercept (A) should be close zero (0) and the slope (B) close 1 as shown in *Figure 39*. As a result, the results obtained using the two methods were not found to be significantly different for REEs. On the other hand, statistically significant variations were discovered for Ag anode X-ray Tube spectrometer estimated element concentrations of REEs under the same conditions. The slopes (0.8399) of the validation curves for REEs were close to 1, but the intercept (-18.581) was not close to zero (0) as shown in *Figure 40*. For Ag anode X-tube spectrometer, the standard deviation of differences was similarly extremely high and considerably departure from zero.

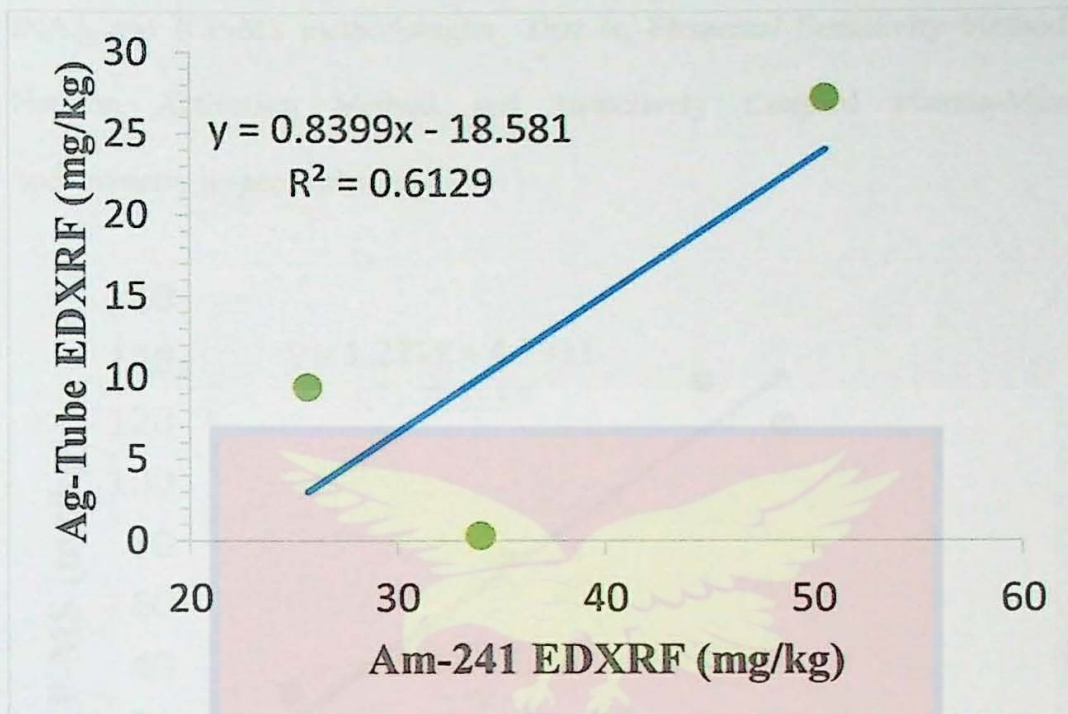


Figure 40: The graph shows a comparison between the results obtained for REEs with Ag anode X-tube spectrometer and Am-241 excitation based system, the correlation equation and the R^2 value of 0.6129.

This shows the limitation of the tube-based XRF excitation system for REE analysis due predominantly to the interference of L X-ray of the REE by the relatively high intensities of K X-ray from the transition metals. This leads to higher inaccuracies in concentration values and a reduction in the scope of the REE that could be analyzed.

The slope of the attached Am-241 excitation-based system and INAA, as well as ICP-MS, was close to 1 in all cases, as well as the intercept close to zero (0) and the linear correlation coefficient (R^2) values was higher than 0.95 in all cases, as shown in *Figures 41* and *42*, respectively. These results showed an excellent match between the attached Am-241 excitation-based system,

INAA and ICP-MS methodologies. That is, Elemental Sensitivity Method, Neutron Activation Method and Inductively Coupled Plasma-Mass Spectrometry respectively.

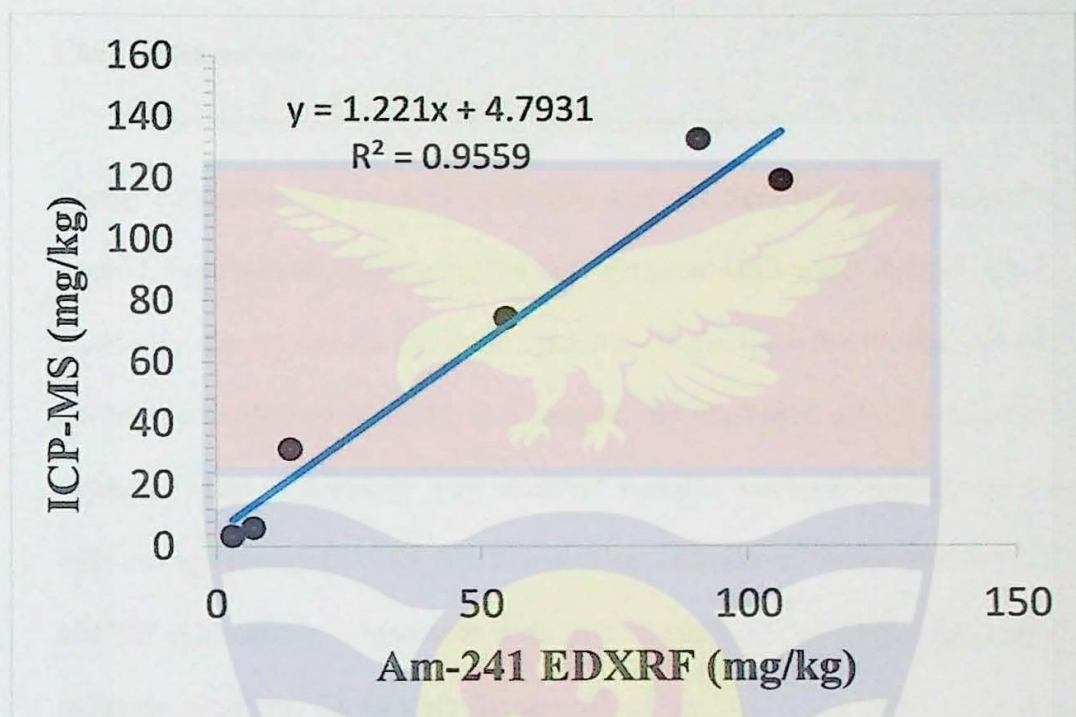


Figure 41: The graph shows a comparison between the results obtained for REEs in sample DK6 using ICP-MS and the attached Am-241 excitation-based EDXRF system, the correlation equation and the R^2 values.

In this study, as it can be observed from Table 8, standard deviation (SD) values were in the range of 3.8-20.7 mg/kg for the elemental sensitivity method for Ag-anode X-Tube spectrometer and 2.0-3.8 mg/kg for the attached Am-241 excitation-based system, also INAA standard deviation values were in the range of 0.09-2.3 mg/kg. The SD values are low when the $SD \leq 10\%$ of the required X-ray fluorescence spectrometers and sometimes $SD > 10\%$ for the constrains of elements of a certain concentration (Syahfitri et al.,

2013). The results show that the attached Am-241 excitation-based system elemental sensitivity method is a reliable and comparable method for the determination of REEs.

Chapter Summary

The results and discussion are summarised below:

Energy calibration has allowed qualitative analysis. Sensitivity calibration for K and L lines was achieved using the following standards using *S, Cl, K, Ca, Ti, Cr, Mn, Fe, Co, Ni, Cu, Zn, As, Br, Sr, Mo, Ag, Cd, Sn, I, Cs, Ba, W, Hg, and Pb*. To be able to determine REEs in a sample, the excitation and the detection geometry were re-designed with attached Am-241 excitation-based sources with average energy (59.54 keV). The incident and take-off angle used is 52.5° and 90° respectively. Measures were put in place to mitigate unnecessary radiation exposure. To validate the developed method, IAEA-SOIL 7, INAA and ICP-MS were used. The results were comparable. Analysing samples that contain REEs, here, are the results for Ag-anode EDXRF, the elements which were identified from this technique for IAEA-soil 7 were Scandium (*Sc*), Europium (*Eu*), Dysprosium (*Dy*) and Ytterbium (*Yb*). For Sample, DK6 are: Lanthanum (*La*), Cerium (*Ce*) and Europium (*Eu*). For Sample DK7 are: Lanthanum (*La*), Cerium (*Ce*), Europium (*Eu*), and Terbium (*Tb*). For sample DK8 are: Lanthanum (*La*), Cerium (*Ce*), Europium (*Eu*) and Terbium (*Tb*).

The elements which were identified from the attached Am-241 excitation-based EDXRF technique for IAEA-Soil 7 are Scandium (*Sc*), Lanthanum (*La*), Cerium (*Ce*), Neodymium (*Nd*), Europium (*Eu*), Erbium

(*Er*). Samarium (*Sm*) and Terbium (*Tb*). For sample DK6 are Scandium (*Sc*), Lanthanum (*La*), Cerium (*Ce*), Neodymium (*Nd*), Europium (*Eu*), Erbium (*Er*). Samarium (*Sm*) and Terbium (*Tb*). For sample DK7 are Scandium (*Sc*), Lanthanum (*La*), Cerium (*Ce*), Neodymium (*Nd*), Erbium (*Er*). For sample DK8 are Scandium (*Sc*), Lanthanum (*La*), Cerium (*Ce*), Neodymium (*Nd*), Europium (*Eu*)

The elements which were identified from this INAA technique for IAEA-Soil 7 were Scandium (*Sc*), Lanthanum (*La*), Cerium (*Ce*), Neodymium (*Nd*), Europium (*Eu*), Erbium (*Er*). Samarium (*Sm*) and Terbium (*Tb*). For sample DK6 are Scandium (*Sc*), Lanthanum (*La*), Cerium (*Ce*), Neodymium (*Nd*), Europium (*Eu*) and Erbium (*Er*). For sample DK7 are Scandium (*Sc*), Lanthanum (*La*), Cerium (*Ce*), Neodymium (*Nd*), Erbium (*Er*). For sample DK8 are Scandium (*Sc*), Lanthanum (*La*), Cerium (*Ce*), Neodymium (*Nd*), Europium (*Eu*)

Standards were used to create sensitivity calibration curves. These standards were chosen to span the range of energies to be determined in the study (33.44-54.06 kV). However, due to the unavailability of the other standards, energies of 33.44-44.47 kV were used in this study. As a result, energy above 44.47 kV cannot be accounted for. In this project, Annual Am-241 sources were used, which required precise determination of incident and take-off angles. The inability to precisely measure these angles may add error, resulting in the inability to acquire exact results, despite the accuracy of the results being good. Validation should have been done with a variety of

certified reference materials (CRM), but due to lack of funding, only IAEA-SOIL 7 was used.



CHAPTER FIVE

SUMMARY, CONCLUSIONS AND RECOMMENDATIONS

Introduction

This chapter summarizes the findings, conclusions, and recommendations for extending the EDXRF spectrometer capabilities at GAEC by optimizing the attached Am-241 excitation-based system to the current Ag- anode X-ray tube spectrometer for REE evaluation (analysis). The following are the four (4) main sections of the chapter: The summary of the research findings, conclusions, the recommendations, and the chapter summary.

Summary

Earlier studies in XRF laboratory unit of National Nuclear Research Institute (NNRI) of Ghana Atomic Energy Commission (GAEC) made use of a benchtop X-ray fluorescence machine (EXP-1) made by Amptek Technologies. EXP-1 spectrometer has Ag-anode X-ray tube (Ag-target) used to determine medium and moderate Z elements using their K-line energies. However, little data are available for rare earth elements. To address this situation, excitation and detection geometry has been developed to obtain results for photon scattering from REEs having their K-edges close to the exciting photon energies at 26.4 and 59.5 keV emitted by Am-241 excitation-based source. The sensitivity and accuracy of the XRF analysis could be considerably improved by properly designing the excitation and detection geometry. The incident and take-off angle used were 52.5° and 90°

respectively. Measures were put in place to mitigate unnecessary radiation exposure. In these measurements, attached Am-241 excitation-based source with a high-intensity output of 100 mCi was used. Irradiation time was 3000 sec. per sample for the REEs.

This study describes the attached Am-241 excitation-based system to the existing Ag-anode X-ray tube spectrometer at GAEC's XRF laboratory, which is primarily used for rare earth element analysis. Scandium (*Sc*), Lanthanum (*La*), Cerium (*Ce*), Neodymium (*Nd*), Samarium (*Sm*), Europium (*Eu*), and Terbium (*Tb*) were discovered using the attached Am-241 excitation-based system technique for IAEA-Soil 7. These results are based on the calibration standards that were available. When compared to the certified values, the Am-241 excitation-based system calculated findings demonstrated a good agreement (see Table 4.2). Based on the INAA and ICP-MS results, the accuracy value is fairly excellent and can be accepted. Our findings imply that EDXRF elemental sensitivity based on attached Am-241 excited-based system is a comparable method for determining REEs.

Conclusions

- i) Existing tube-excited XRF spectrometers can only measure few REEs with poor accuracy. It has however been possible to extend the scope of an existing tube-based spectrometer, with an Am-241 excitation-based system for REE analysis. This enabled the analysis of the following REEs; *Sc, Y, La, Ce, Nd, Sm, Eu, Gd* and *Er* with their K-X-rays

- ii) Development of the quantitative method using the “Elemental Sensitivities Method” of the QXAS Software, and K-X-ray improved accuracy in analysis of REEs using the XRF analytical technique
- iii) Comparative analysis results of the Am-241 excitation-based system with ICP-MS and INAA technique established the Am-241 excitation-based system as a reliable, accurate alternative for analysis of REEs. Am-241 excitation-based system offers possibilities for fast and accurate routine analysis of large number of samples, since sample preparation is minimal and analysis time shorter compared to the other techniques (INAA & ICP-MS)

Recommendations

Based on this thesis work, the following recommendations are proffered:

1. Currently, the system can only analyse one sample at a time; it is, therefore, recommended to the Ministry of Environment, Science, Technology & Innovation (MESTI) to provide funding to automate the system for routine analysis of multiple samples.
2. In order to cover the entire spectrum of REE analysis on the Periodic Table, it is recommended to UCC through the department of Physics to provide funding for purchasing REE standard elements to enable improved sensitivity calibration.
3. Due to inadequate funding for this thesis work, only IAEA-SOIL 7 reference material was used in the validation process. It is

recommended for future research to analyze certified reference materials that contain REE elements



REFERENCES

- Abaka-Wood, G. B., Addai-Mensah, J., & Skinner, W. (2017). A study of flotation characteristics of monazite, hematite, and quartz using anionic collectors. *International Journal of Mineral Processing*, 158, 55–62.
- Abaka-Wood, G. B., Quast, K., Zanin, M., Addai-Mensah, J., & Skinner, W. (2019). A study of the feasibility of upgrading rare earth elements minerals from iron-oxide-silicate rich tailings using Knelson concentrator and Wilfley shaking table. *Powder Technology*, 344, 897–913.
- Adazabra, A. N., Ntiforo, A., & Bamford, S. A. (2014). Analysis of essential elements in Pito—A cereal food drink and its brands by the single-comparator method of neutron activation analysis. *Food Science & Nutrition*, 2(3), 230–235.
- Alharbi, A., & El-Taher, A. (2016). Elemental analysis of basalt by instrumental neutron activation analysis and inductively coupled plasma mass spectrometer. *Journal of Environmental Science and Technology*, 9(4), 335.
- Alvarez, R. P., Markowicz, A., Wegrzynek, D., Cano, E. C., Bamford, S. A., & Torres, D. H. (2007). Quality management and method validation in EDXRF analysis. *X-Ray Spectrometry: An International Journal*, 36(1), 27–34.
- Amaral, C. D., Machado, R. C., Barros, J. A., Virgilio, A., Schiavo, D., Nogueira, A. R. A., & Nobrega, J. A. (2017). Determination of rare

earth elements in geological and agricultural samples by ICP-OES. *Spectroscopy*, 32(10), 32.

Anderson, C. R., & Pedersen, K. (2003). In situ growth of *Gallionella* biofilms and partitioning of lanthanides and actinides between biological material and ferric oxyhydroxides. *Geobiology*, 1(2), 169–178.

Baidoo, I. K., Li, B., Yang, Q., Song, J., & Hu, L. Q. (2018). Verification of SuperMC for MNSRs Core Analysis: The Case of Ghana Research Reactor-I. *Annals of Nuclear Energy*, 113, 48–54.

Baidya, T. K., Mondal, S. K., Balaram, V., Parthasarathy, R., Verma, R., & Mathur, P. K. (1999). PGE-Ag-Au mineralization in a Cu-Fe-Ni sulphide-rich breccia zone of the Precambrian Nuasahi ultramafic-mafic complex, Orissa, India. *Journal of Geological Society of India (Online Archive from Vol 1 to Vol 78)*, 54(5), 473–482.

Baker, J., Waight, T., & Ulfbeck, D. (2002). Rapid and highly reproducible analysis of rare earth elements by multiple collector inductively coupled plasma mass spectrometry. *Geochimica et Cosmochimica Acta*, 66(20), 3635–3646.

Balaram, V. (1995). Developments and trends in inductively coupled plasma mass spectrometry and its influence on the recent advances in trace element analysis. *Current Science*, 69(8), 640–649.

Balaram, V. (2016). Recent advances in the determination of elemental impurities in pharmaceuticals—Status, challenges and moving frontiers. *Trac Trends in Analytical Chemistry*, 80, 83–95.

- Balaram, V. (2017). Field-portable analytical instruments in mineral exploration: Past, present and future. *Journal of Applied Geochemistry*, 19(4), 382–399.
- Balaram, V. (2019). Rare earth elements: A review of applications, occurrence, exploration, analysis, recycling, and environmental impact. *Geoscience Frontiers*, 10(4), 1285–1303.
- Balaram, V. (2022). *Sources and applications of rare earth elements*.
- Balaram, V., Vummiti, D., Roy, P., Taylor, C., Kar, P., Raju, A. K., & Abburi, K. (2013). Determination of precious metals in rocks and ores by microwave plasma-atomic emission spectrometry for geochemical prospecting studies. *Current Science*, 1207–1215.
- Banakar, V. K., & Borole, D. V. (1991). Depth profiles of 230Th excess, transition metals and mineralogy of ferromanganese crusts of the Central Indian basin and implications for palaeoceanographic influence on crust genesis. *Chemical Geology*, 94(1), 33–44.
- Bandhu, H. K., Puri, S., Garg, M. L., Singh, B., Shahi, J. S., Mehta, D., Swietlicki, E., Dhawan, D. K., Mangal, P. C., & Singh, N. (2000). Elemental composition and sources of air pollution in the city of Chandigarh, India, using EDXRF and PIXE techniques. *Nuclear Instruments and Methods in Physics Research Section B: Beam Interactions with Materials and Atoms*, 160(1), 126–138.
- Bastos, R. O., Melquiades, F. L., & Biasi, G. E. V. (2012). Correction for the effect of soil moisture on in situ XRF analysis using low-energy background. *X-Ray Spectrometry*, 41(5), 304–307.

- Bayon, G., Barrat, J. A., Etoubleau, J., Benoit, M., Bollinger, C., & Révillon, S. (2009). Determination of rare earth elements, Sc, Y, Zr, Ba, Hf and Th in geological samples by ICP-MS after Tm addition and alkaline fusion. *Geostandards and Geoanalytical Research*, 33(1), 51–62.
- Becker, J. S., & Dietze, H.-J. (2003). State-of-the-art in inorganic mass spectrometry for analysis of high-purity materials. *International Journal of Mass Spectrometry*, 228(2–3), 127–150.
- Beckhoff, B., Kanngießler, B., Langhoff, N., Wedell, R., & Wolff, H. (2007). *Handbook of practical X-ray fluorescence analysis*. Springer Science & Business Media.
- Bentlin, F. R., & Pozebon, D. (2010). Direct determination of lanthanides in environmental samples using ultrasonic nebulization and ICP OES. *Journal of the Brazilian Chemical Society*, 21(4), 627–634.
- Bernasconi, G. B. (1993). IAEA AXIL–QXAS Version Reference Manual. IAEA, Vienna.
- Bhatt, B., Angeyo, K. H., & Dehayem-Kamadjeu, A. (2018). LIBS development methodology for forensic nuclear materials analysis. *Analytical Methods*, 10(7), 791–798.
- Bhushan, S. K., & Kumar, A. (2013). First carbonatite hosted REE deposit from India. *Journal of the Geological Society of India*, 81(1), 41–60.
- Bhushan, S. K., & Somani, O. P. (2019). Rare earth elements and yttrium potentials of Neoproterozoic peralkaline Siwana granite of Malani igneous suite, Barmer district, Rajasthan. *Journal of the Geological Society of India*, 94(1), 35–41.

- Bounouira, H., Choukri, A., Elmoursli, R. C., Hakam, O. K., & Chakiri, S. (2007). Distribution of the rare earth elements in the sediments of the Bouregreg river (Morocco) using the instrumental neutron activation analysis (INAA). *Journal of Applied Sciences and Environmental Management*, 11(1).
- Brouwer, P. (2006). Theory of XRF. *Almelo, Netherlands: PANalytical BV*.
- Castor, S. B., & Hedrick, J. B. (2006). Industrial minerals and rocks. *Society for Mining, Metallurgy, and Exploration, Inc*, 769–792.
- Chausseau, M., Stankova, A., Li, Z., Hunault, P., & Savadkouei, H. (2014). High-resolution ICP-OES for the determination of trace elements in a rare earth element matrix and in NdFeB magnetic materials. *Spectroscopy*, 29(11), 30–41.
- Cordier, D. J., & Hedrick, J. B. (2010). Minerals Yearbook RARE EARTHS [ADVANCE RELEASE]. *US Geological Survey*.
- Cremers, D. A., & Radziemski, L. J. (2006). Basics of the LIBS Plasma. *Handbook of Laser-Induced Breakdown Spectroscopy*, 23–52.
- Cremers, D. A., & Radziemski, L. J. (2013). *Handbook of laser-induced breakdown spectroscopy*. John Wiley & Sons.
- Criss, J. W., & Birks, L. S. (1968). Calculation methods for fluorescent x-ray spectrometry. Empirical coefficients versus fundamental parameters. *Analytical Chemistry*, 40(7), 1080–1086.
- Cruse, A. M., Lyons, T. W., & Kidder, D. L. (2000). *Rare-earth element behavior in phosphates and organic-rich host shales: An example from the Upper Carboniferous of Midcontinent North America*.

- Dai, S., Liu, J., Ward, C. R., Hower, J. C., French, D., Jia, S., Hood, M. M., & Garrison, T. M. (2016). Mineralogical and geochemical compositions of Late Permian coals and host rocks from the Guxu Coalfield, Sichuan Province, China, with emphasis on enrichment of rare metals. *International Journal of Coal Geology*, 166, 71–95.
- Dar, M. A., & El Saman, M. I. (2014). The interactions of some radioelements activity patterns with some hydrographic parameters at the petroleum and phosphate regions in the Red Sea, Egypt. *Journal of Radiation Research and Applied Sciences*, 7(3), 292–304.
- De Vito, I. E., Olsina, R. A., & Masi, A. N. (2000). Enrichment method for trace amounts of rare earth elements using chemofiltration and XRF determination. *Fresenius' Journal of Analytical Chemistry*, 368(4), 392–396.
- Diatloff, E., Smith, F. W., & Asher, C. J. (1995). Rare earth elements and plant growth: I. Effects of lanthanum and cerium on root elongation of corn and mungbean. *Journal of Plant Nutrition*, 18(10), 1963–1976.
- Doroshkevich, A. G., Viladkar, S. G., Ripp, G. S., & Burtseva, M. V. (2009). Hydrothermal REE mineralization in the Amba Dongar carbonatite complex, Gujarat, India. *The Canadian Mineralogist*, 47(5), 1105–1116.
- Dostal, J. (2017). Rare earth element deposits of alkaline igneous rocks. *Resources*, 6(3), 34.

- Durivage, M. (2021). *7 Rules For Properly Interpreting Control Charts*.
<https://www.pharmaceuticalonline.com/doc/rules-for-properly-interpreting-control-charts-0001>
- Dushyantha, N., Batapola, N., Ilankoon, I., Rohitha, S., Premasiri, R., Abeysinghe, B., Ratnayake, N., & Dissanayake, K. (2020). The story of rare earth elements (REEs): Occurrences, global distribution, genesis, geology, mineralogy and global production. *Ore Geology Reviews*, *122*, 103521.
- Eggert, R. (n.d.). *Critical Materials and the Critical Materials Institute*. 20.
- Emsbo, P., McLaughlin, P. I., Breit, G. N., du Bray, E. A., & Koenig, A. E. (2015). Rare earth elements in sedimentary phosphate deposits: Solution to the global REE crisis? *Gondwana Research*, *27*(2), 776–785.
- Eskenazy, G. M. (1987). Rare earth elements in a sampled coal from the Pirin deposit, Bulgaria. *International Journal of Coal Geology*, *7*(3), 301–314.
- Figuereido, A. M. G., & Marques, L. S. (1989). Determination of rare earth elements and other trace elements in Brazilian geological standards, BB-1 and GB-1 by neutron activation analysis. *Geochimica Brasiliensis*, *3*(1), 1–8.
- Franus, W., Wiatros-Motyka, M. M., & Wdowin, M. (2015). Coal fly ash as a resource for rare earth elements. *Environmental Science and Pollution Research*, *22*(12), 9464–9474.

- Fu, F., Akagi, T., Yabuki, S., & Iwaki, M. (2001). The variation of REE (rare earth elements) patterns in soil-grown plants: A new proxy for the source of rare earth elements and silicon in plants. *Plant and Soil*, 235(1), 53–64.
- Funtua, I. I. (2004). EDXRF analysis of pyrochlore ore from an albite-riebeckite granite in Nigeria. *Instrumentation Science & Technology*, 32(5), 529–536.
- Furie, B., Eastlake, A., Schechter, A. N., & Anfinsen, C. B. (1973). The interaction of the lanthanide ions with staphylococcal nuclease. *Journal of Biological Chemistry*, 248(16), 5821–5825.
- Gauglitz, G., & Moore, D. S. (2014a). *Handbook of spectroscopy* (Vol. 1). Wiley-Vch Weinheim.
- Gauglitz, G., & Moore, D. S. (2014b). *Handbook of spectroscopy* (Vol. 1). Wiley-Vch Weinheim.
- Ge, L., Lai, W., & Lin, Y. (2005). Influence of and correction for moisture in rocks, soils and sediments on in situ XRF analysis. *X-Ray Spectrometry: An International Journal*, 34(1), 28–34.
- Gibson, M., & Parkinson, I. (2011). Once Ignored on the Periodic Table, Don't Ignore Them Now. A Rare Earth Element Industry Overview. *Publication, CIBC World Markets, Toronto*.
- Golightly, D. W., & Simon, F. O. (1989). *Methods for sampling and inorganic analysis of coal*.

- Greaves, E. D., Bohus, L. S., Marco, L., & Alvarez, M. (1992). A Compton peak method for incident angle determination in XRF with annular excitation. *X-Ray Spectrometry*, 21(3), 127–131.
- Greenfield, S., Jones, I. L., & Berry, C. T. (1964). High-pressure plasmas as spectroscopic emission sources. *Analyst*, 89(1064), 713–720.
- Gromet, L. P., Haskin, L. A., Korotev, R. L., & Dymek, R. F. (1984). The “North American shale composite”: Its compilation, major and trace element characteristics. *Geochimica et Cosmochimica Acta*, 48(12), 2469–2482.
- Gulani, V., Calamante, F., Shellock, F. G., Kanal, E., & Reeder, S. B. (2017). Gadolinium deposition in the brain: Summary of evidence and recommendations. *The Lancet Neurology*, 16(7), 564–570.
- Gupta, C. K., & Krishnamurthy, N. (1992). Extractive metallurgy of rare earths. *International Materials Reviews*, 37(1), 197–248.
- Hammer, M. R. (2008). A magnetically excited microwave plasma source for atomic emission spectroscopy with performance approaching that of the inductively coupled plasma. *Spectrochimica Acta Part B: Atomic Spectroscopy*, 63(4), 456–464.
- Haque, N., Hughes, A., Lim, S., & Vernon, C. (2014). Rare earth elements: Overview of mining, mineralogy, uses, sustainability and environmental impact. *Resources*, 3(4), 614–635.
- Haschke, M. (2014a). Laboratory micro-X-ray fluorescence spectroscopy. *Cham: Springer International Publishing*, 10, 978–983.

- Haschke, M. (2014b). Main Components of X-ray Spectrometers. In *Laboratory Micro-X-Ray Fluorescence Spectroscopy* (pp. 19–118). Springer.
- Haskin, M. A., & Haskin, L. A. (1966). Rare earths in European shales: A redetermination. *Science*, *154*(3748), 507–509.
- He, F., & Van Espen, P. J. (1991). General approach for quantitative energy dispersive x-ray fluorescence analysis based on fundamental parameters. *Analytical Chemistry*, *63*(20), 2237–2244.
- Hein, J. R., Mizell, K., Koschinsky, A., & Conrad, T. A. (2013). Deep-ocean mineral deposits as a source of critical metals for high-and green-technology applications: Comparison with land-based resources. *Ore Geology Reviews*, *51*, 1–14.
- Helmecci, E., Wang, Y., & Brindle, I. D. (2016). A novel methodology for rapid digestion of rare earth element ores and determination by microwave plasma-atomic emission spectrometry and dynamic reaction cell-inductively coupled plasma-mass spectrometry. *Talanta*, *160*, 521–527.
- Henderson, P. (1984). General geochemical properties and abundances of the rare earth elements. In *Developments in geochemistry* (Vol. 2, pp. 1–32). Elsevier.
- Hoatson, D. M., Jaireth, S., & Mieзитis, Y. (2011). *The major rare-earth-element deposits of Australia: Geological setting, exploration, and resources*. Geoscience Australia.

- Hou, X., He, Y., & Jones, B. T. (2004). Recent advances in portable X-ray fluorescence spectrometry. *Applied Spectroscopy Reviews*, 39(1), 1–25.
- Hower, J. C., Dai, S., Seredin, V. V., Zhao, L., Kostova, I. J., Silva, L. F., Mardon, S. M., & Gurdal, G. (2013). A note on the occurrence of yttrium and rare earth elements in coal combustion products. *Coal Combustion and Gasification Products*, 5(2), 39–47.
- Hower, J. C., Granite, E. J., Mayfield, D. B., Lewis, A. S., & Finkelman, R. B. (2016). Notes on contributions to the science of rare earth element enrichment in coal and coal combustion byproducts. *Minerals*, 6(2), 32.
- Hulle, D. V. (2022). *Genetic Criticism: Tracing Creativity in Literature*. Oxford University Press.
- HUMPHRIES, M. (2012). *Rare Earth Elements: The Global Supply Chain Congressional Research Service Report*. Sept.
- IAEA, Q. X. (2005). Ray analysis system, QXAS, Doc. *Version, 1*, 1995–1996.
- Ivošević, T., Mandić, L., Orlić, I., Stelcer, E., & Cohen, D. D. (2014). Comparison between XRF and IBA techniques in analysis of fine aerosols collected in Rijeka, Croatia. *Nuclear Instruments and Methods in Physics Research Section B: Beam Interactions with Materials and Atoms*, 337, 83–89.

- Italian Institute for International Political Studies (ISPI). Commentary. The Scramble for Africa's Rare Earths: China is not Alone, Pier Paolo Raimondi 07 June 2021.
- Jalas, P., Ruottinen, J. P., & Hemminki, S. (2002). XRF Analysis of jewelry using fully standardless fundamental parameter approach. *World Gold Council*, 35, 28–34.
- Janssen, M., & Lehner, C. (2014). *The Cambridge Companion to Einstein* (Vol. 1). Cambridge University Press.
- Janssens, K., Snickt, G. V. der, Vanmeert, F., Legrand, S., Nuyts, G., Alfeld, M., Monico, L., Anaf, W., Nolf, W. D., & Vermeulen, M. (2017). Non-invasive and non-destructive examination of artistic pigments, paints, and paintings by means of X-ray methods. *Analytical Chemistry for Cultural Heritage*, 77–128.
- Janssens, K., & Van Grieken, R. (2004). *Non-destructive micro analysis of cultural heritage materials*. Elsevier.
- Jarvis, I., Burnett, W. C., Nathan, Y., Almbaydin, F. S. M., Attia, A. K. M., Castro, L. N., Flicoteaux, R., Hilmy, M. E., Husain, V., & Qutawnah, A. A. (1994). Phosphorite geochemistry: State-of-the-art and environmental concerns. *Eclogae Geologicae Helvetiae*, 87(3), 643–700.
- Jarvis, I., & Jarvis, K. E. (1985). Rare-earth element geochemistry of standard sediments: A study using inductively coupled plasma spectrometry. *Chemical Geology*, 53(3–4), 335–344.

- Jenkins, R. (1995). *Quantitative X-ray spectrometry*. CRC Press.
- Jenkins, R. (1999a). *Overview-XRF and XRD*.
- Jenkins, R. (1999b). X-Ray Fluorescence Analysis. *X-Ray Characterization of Materials*, 171–209.
- Jenkins, R. (2012). *X-ray fluorescence spectrometry*.
- Jochum, K. P., Seufert, H. M., Midinet-Best, S., Rettmann, E., Schönberger, K., & Zimmer, M. (1988). Multi-element analysis by isotope dilution-spark source mass spectrometry (ID-SSMS). *Fresenius' Zeitschrift Für Analytische Chemie*, 331(2), 104–110.
- Jordens, A., Cheng, Y. P., & Waters, K. E. (2013). A review of the beneficiation of rare earth element bearing minerals. *Minerals Engineering*, 41, 97–114.
- Juras, S. J., Hickson, C. J., Horsky, S. J., Godwin, C. I., & Mathews, W. H. (1987). A practical method for the analysis of rare-earth elements in geological samples by graphite furnace atomic absorption and X-ray fluorescence. *Chemical Geology*, 64(1–2), 143–148.
- Kamala, C. T., Balaram, V., Dharmendra, V., Satyanarayanan, M., Subramanyam, K. S. V., & Krishnaiah, A. (2014). Application of Microwave Plasma Atomic Emission Spectrometry (MP-AES) for environmental monitoring of industrially contaminated sites in Hyderabad City. *Environmental Monitoring and Assessment*, 186(11), 7097–7113.
- Karandashev, V. K., Orlova, T. A., Lezhnev, A. E., Nosenko, S. V., Zolotareva, N. I., Moskvina, I. R., & Turanov, A. N. (2007). Use of

- mass spectrometry with inductively coupled plasma method for element analysis of surrounding medium objects. *Zavodskaya Laboratoriya*, 73(1), 12–22.
- Kato, Y., Fujinaga, K., Nakamura, K., Takaya, Y., Kitamura, K., Ohta, J., Toda, R., Nakashima, T., & Iwamori, H. (2011). Deep-sea mud in the Pacific Ocean as a potential resource for rare-earth elements. *Nature Geoscience*, 4(8), 535–539.
- Kin, F. D., Prudêncio, M. I., Gouveia, M. Â., & Magnusson, E. (1999). Determination of rare earth elements in geological reference materials: A comparative study by INAA and ICP-MS. *Geostandards Newsletter*, 23(1), 47–58.
- King, F. L., Teng, J., & Steiner, R. E. (1995). Special feature: Tutorial. Glow discharge mass spectrometry: trace element determinations in solid samples. *Journal of Mass Spectrometry*, 30(8), 1061–1075.
- Klinkhammer, G., German, C. R., Elderfield, H., Greaves, M. J., & Mitra, A. (1994). Rare earth elements in hydrothermal fluids and plume particulates by inductively coupled plasma mass spectrometry. *Marine Chemistry*, 45(3), 179–186.
- Kogan, R. M., Nazarov, I. M., & Fridman, S. D. (1991). *Principles of Gamma-Spectrometry of Natural Media*. Énergoatomizdat Moscow.
- Kolesov, G. M. (1994). Determination of trace elements: Neutron-activation analysis in geochemistry and cosmochemistry. *Journal of Analytical Chemistry*, 49(1).

- Krishna, K. S., Bull, J. M., Ishizuka, O., Scrutton, R. A., Jaishankar, S., & Banakar, V. K. (2014). Growth of the Afanasy Nikitin seamount and its relationship with the 85 E Ridge, northeastern Indian Ocean. *Journal of Earth System Science*, 123(1), 33–47.
- Krishnamurthy, A., & Vissing-Jorgensen, A. (2015). The impact of treasury supply on financial sector lending and stability. *Journal of Financial Economics*, 118(3), 571–600.
- Krishnamurthy, N., & Gupta, C. K. (2015). *Extractive Metallurgy of Rare Earths* (2nd ed.). CRC Press. <https://doi.org/10.1201/b19055>
- Krusberski, N. (2006). Exploring potential errors in XRF analysis. *Analytical Challenges in Metallurgy. Johannesburg, South Africa: The Southern African Institute of Mining and Metallurgy*, 1–8.
- Lafleur, M. P.-J., Eng, P., Ayad, M. A. B., & Geo, P. (2012). NI 43-101 Technical Report to present the mineral resources of the rare earth elements zone Niobec Mine-IAMGOLD Corporation. *Ste-Therese, QC, CA*, 1–145.
- Lang, J., Zhang, Y., Zhou, Y., Cheng, S., Chen, D., Guo, X., Chen, S., Li, X., Xing, X., & Wang, H. (2017). Trends of PM_{2.5} and chemical composition in Beijing, 2000-2015. *Aerosol and Air Quality Research*, 17(2), 412–425.
- Lee, K.-H., Shishido, S., Kusachi, I., & Motomizu, S. (2000). Determination of lanthanoids and yttrium in JGb2 and JR3 by inductively coupled plasma-mass spectrometry after cation-exchange pretreatment. *Geochemical Journal*, 34(5), 383–393.

- Li, F., Ge, L., Tang, Z., Chen, Y., & Wang, J. (2020). Recent developments on XRF spectra evaluation. *Applied Spectroscopy Reviews*, 55(4), 263–287.
- Li, S., Yang, J., Chen, W.-H., & Chen, X. (2014). *Disturbance observer-based control: Methods and applications*. CRC press.
- Li, Z., & Schieber, J. (2020). Application of sequence stratigraphic concepts to the Upper Cretaceous Tununk Shale Member of the Mancos Shale Formation, south-central Utah: Parasequence styles in shelfal mudstone strata. *Sedimentology*, 67(1), 118–151.
- Liu, C.-Q., Masuda, A., Okada, A., Yabuki, S., Zhang, J., & Fan, Z.-L. (1993). A geochemical study of loess and desert sand in northern China: Implications for continental crust weathering and composition. *Chemical Geology*, 106(3), 359–374. [https://doi.org/10.1016/0009-2541\(93\)90037-J](https://doi.org/10.1016/0009-2541(93)90037-J)
- Long, K. R., Van Gosen, B. S., Foley, N. K., & Cordier, D. (2012). The Principal Rare Earth Elements Deposits of the United States: A Summary of Domestic Deposits and a Global Perspective. In R. Sinding-Larsen & F.-W. Wellmer (Eds.), *Non-Renewable Resource Issues* (pp. 131–155). Springer Netherlands. https://doi.org/10.1007/978-90-481-8679-2_7
- Lusty, P., & Walters, A. (2010). *Rare earth elements*.
- Makreski, P., Jovanovski, G., Runčevski, T., & Jaćimović, R. (2011). Simple and efficient method for detection of traces of rare earth elements in

- minerals by Raman spectroscopy instrumentation. *Macedonian Journal of Chemistry and Chemical Engineering*, 30(2), 241–250.
- Margui, E., & Van Grieken, R. (2013). *X-ray fluorescence spectrometry and related techniques: An introduction*. Momentum press.
- Mazet, V., Carteret, C., Brie, D., Idier, J., & Humbert, B. (2005). Background removal from spectra by designing and minimising a non-quadratic cost function. *Chemometrics and Intelligent Laboratory Systems*, 76(2), 121–133.
- Mazumder, J., Schifferer, A., & Choi, J. (1999). Direct materials deposition: Designed macro and microstructure. *Material Research Innovations*, 3(3), 118–131.
- McDonald, R. J., McDonald, J. S., Kallmes, D. F., Jentoft, M. E., Murray, D. L., Thielen, K. R., Williamson, E. E., & Eckel, L. J. (2015). Intracranial gadolinium deposition after contrast-enhanced MR imaging. *Radiology*, 275(3), 772–782.
- McLeod, C. L., & Krekeler, M. (2017). Sources of extraterrestrial rare earth elements: To the moon and beyond. *Resources*, 6(3), 40.
- Moore, D. S. (2014). *Handbook of Spectroscopy* (Vol. 1). John Wiley & Sons.
- Mzyk, Z., Baranowska, I., & Mzyk, J. (2002). Research on grain size effect in XRF analysis of pelletized samples. *X-Ray Spectrometry: An International Journal*, 31(1), 39–46.
- Nath, B. N., Balaram, V., Sudhakar, M., & Plüger, W. L. (1992). Rare earth element geochemistry of ferromanganese deposits from the Indian Ocean. *Marine Chemistry*, 38(3–4), 185–208.

- Nath, B. N., Roelandts, I., Sudhakar, M., Plüger, W. L., & Balaram, V. (1994). Cerium anomaly variations in ferromanganese nodules and crusts from the Indian Ocean. *Marine Geology*, 120(3–4), 385–400.
- Nath, B. N., & Sharma, R. (2000). Environment and deep-sea mining: A perspective. *Marine Georesources & Geotechnology*, 18(3), 285–294.
- Nieto, A., & Zhang, K. Y. (2013). Cutoff grade economic strategy for byproduct mineral commodity operation: Rare earth case study. *Mining Technology*, 122(3), 166–171.
- Nikonov, V. V., Lukina, N. V., & Frontas' Eva, M. V. (1999). Trace elements in Al-Fe-humus podzolic soils subjected to aerial pollution from the apatite-nepheline production industry. *Eurasian Soil Science*, 32(12), 1331–1339.
- Nude, P. M., Kwayisi, D., Taki, N. A., Kutu, J. M., Anani, C. Y., Banoeng-Yakubo, B., & Asiedu, D. K. (2015). Petrography and chemical evidence for multi-stage emplacement of western Buem volcanic rocks in the Dahomeyide orogenic belt, southeastern Ghana, West Africa. *Journal of African Earth Sciences*, 112, 314–327.
- Nyarko, B., Akaho, E., & Serfor-Armah, Y. (2003). Application of NAA standardization methods using a low power research reactor. *Journal of Radioanalytical and Nuclear Chemistry*, 257(2), 361–366.
- Onishi, H., Nagai, H., & Toita, Y. (1962). Spectrophotometric determination of rare earth elements and thorium with arsenazo. *Analytica Chimica Acta*, 26, 528–531.

- Osei, B., Baidoo, I. K., Odoi, H. C., Gasu, P. D., & Nyarko, B. J. B. (2021). The low enriched uranium miniature neutron source reactor (LEU-MNSR) neutron spectrum characterization for k₀-INAA. *Nuclear Instruments and Methods in Physics Research Section A: Accelerators, Spectrometers, Detectors and Associated Equipment*, 1005, 165397.
- Palaparathi, J., Chakrabarti, R., Banerjee, S., Guin, R., Ghosal, S., Agrahari, S., & Sengupta, D. (2017). Economically viable rare earth element deposits along beach placers of Andhra Pradesh, eastern coast of India. *Arabian Journal of Geosciences*, 10(9), 1–8.
- Palmer, C. A., & Baedeker, P. A. (1989). The determination of 41 elements in whole coal by instrumental neutron activation analysis. *Methods for Sampling and Inorganic Analysis of Coal: US Geological Survey Bulletin*, 1823, 27–34.
- Pandey, L. P. (1992). Certificate of Analysis of Sample No 2388. *CSIR-National Metallurgical Laboratory, Jamshedpur, India*.
- Pang, X., Li, D., & Peng, A. (2002). Application of rare-earth elements in the agriculture of China and its environmental behavior in soil. *Environmental Science and Pollution Research*, 9(2), 143–148.
- Paropkari, A. L., Ray, D., Balaram, V., Prakash, L. S., Mirza, I. H., Satyanarayana, M., Rao, T. G., & Kaisary, S. (2010). Formation of hydrothermal deposits at Kings Triple Junction, northern Lau back-arc basin, SW Pacific: The geochemical perspectives. *Journal of Asian Earth Sciences*, 38(3–4), 121–130.

- Pazand, K. (2015). Rare earth element geochemistry of coals from the Mazino Coal Mine, Tabas Coalfield, Iran. *Arabian Journal of Geosciences*, 8(12), 10859–10869.
- Pemmer, B., Roschger, A., Wastl, A., Hofstaetter, J. G., Wobrauschek, P., Simon, R., Thaler, H. W., Roschger, P., Klaushofer, K., & Strelci, C. (2013). Spatial distribution of the trace elements zinc, strontium and lead in human bone tissue. *Bone*, 57(1), 184–193.
- Perelomov, L. V. (2007). Interactions of rare earth elements with biotic and abiotic soil components. *AGROKHMIIA*, 11, 85.
- Potts, P. J., & Webb, P. C. (1992). X-ray fluorescence spectrometry. *Journal of Geochemical Exploration*, 44(1–3), 251–296.
- Potts, P. J., Webb, P. C., & Thompson, M. (2015). Bias in the determination of Zr, Y and rare earth element concentrations in selected silicate rocks by ICP-MS when using some routine acid dissolution procedures: Evidence from the GeoPT proficiency testing programme. *Geostandards and Geoanalytical Research*, 39(3), 315–327.
- Qi, H., Hu, R., & Zhang, Q. (2007). REE geochemistry of the Cretaceous lignite from Wulantuga germanium deposit, Inner Mongolia, northeastern China. *International Journal of Coal Geology*, 71(2–3), 329–344.
- Raju, C. S. K., Cossmer, A., Scharf, H., Panne, U., & Lück, D. (2010). Speciation of gadolinium based MRI contrast agents in environmental water samples using hydrophilic interaction chromatography

- hyphenated with inductively coupled plasma mass spectrometry. *Journal of Analytical Atomic Spectrometry*, 25(1), 55–61.
- Raut, N. M., Huang, L.-S., Aggarwal, S. K., & Lin, K.-C. (2003). Determination of lanthanides in rock samples by inductively coupled plasma mass spectrometry using thorium as oxide and hydroxide correction standard. *Spectrochimica Acta Part B: Atomic Spectroscopy*, 58(5), 809–822.
- Ravisankar, R., Manikandan, E., Dheenathayalu, M., Rao, B., Seshadreesan, N. P., & Nair, K. G. M. (2006). Determination and distribution of rare earth elements in beach rock samples using instrumental neutron activation analysis (INAA). *Nuclear Instruments and Methods in Physics Research Section B: Beam Interactions with Materials and Atoms*, 251(2), 496–500.
- Ray, J. S., & Shukla, P. N. (2004). Trace element geochemistry of Amba Dongar carbonatite complex, India: Evidence for fractional crystallization and silicate-carbonate melt immiscibility. *Journal of Earth System Science*, 113(4), 519–531.
- Redling, K. (2006). *Rare earth elements in agriculture with emphasis on animal husbandry* [PhD Thesis]. Imu.
- Rim, K.-T. (2016). Effects of rare earth elements on the environment and human health: A literature review. *Toxicology and Environmental Health Sciences*, 8(3), 189–200.
- ROBINSON, M. A. (2011). Rare earths provide critical weapons support. *Defense Media Network*.

- Rogan, N., Serafimovski, T., Dolenc, M., Tasev, G., & Dolenc, T. (2006). The distribution of rare earth elements (REEs) in paddy soil and rice seeds from Kočani Field (eastern Macedonia). *RMZ-Materials and Geoenvironment*, 53(4), 433–444.
- Savichev, A. T., & Sorokin, S. E. (2000). X-ray fluorescence analysis of micronutrients and heavy metals in soils. *Eurasian Soil Science*, 33(SUPPL. 2).
- Savichev, A. T., & Vodyanitskii, Y. N. (2012). Improvement of the X-ray radiometric method of lanthanides' diagnostics in soils. *Eurasian Soil Science*, 45(7), 665–674.
- Saxena, O. C. (1970). Direct titrimetric determination of samarium and neodymium. *Microchemical Journal*, 15(1), 38–41.
- Schneider, A. R., Cancès, B., Breton, C., Ponthieu, M., Morvan, X., Conreux, A., & Marin, B. (2016). Comparison of field portable XRF and aqua regia/ICPAES soil analysis and evaluation of soil moisture influence on FPXRF results. *Journal of Soils and Sediments*, 16(2), 438–448.
- Singh, H., Sadiq, M., & Sharma, B. B. (2014). Exploration for rare earth elements in North East India. *Current Science*, 107(2), 178–180.
- Singh, Y. (2020). Strategic and critical element potential of Indian carbonatites. *Jour. Geosciences Res*, 5(2), 161–170.
- Sitko, R. (2009). Quantitative X-ray fluorescence analysis of samples of less than 'infinite thickness': Difficulties and possibilities. *Spectrochimica Acta Part B: Atomic Spectroscopy*, 64(11–12), 1161–1172.

- Smoliński, A., Stempin, M., & Howaniec, N. (2016). Determination of rare earth elements in combustion ashes from selected Polish coal mines by wavelength dispersive X-ray fluorescence spectrometry. *Spectrochimica Acta Part B: Atomic Spectroscopy*, 116, 63–74.
- Sreenivasulu, V., Kumar, N. S., Dharmendra, V., Asif, M., Balaram, V., Zhengxu, H., & Zhen, Z. (2017). Determination of Boron, Phosphorus, and Molybdenum Content in Biosludge Samples by Microwave Plasma Atomic Emission Spectrometry (MP-AES). *Applied Sciences* (2076-3417), 7(3).
- Statham, P. J. (1977). Deconvolution and background subtraction by least-squares fitting with prefiltering of spectra. *Analytical Chemistry*, 49(14), 2149–2154.
- Storm, E., Israel, H. I., & Lier, D. W. (1970). *BREMSSTRAHLUNG EMISSION MEASUREMENT FROM THICK TUNGSTEN TARGETS IN THE ENERGY RANGE 12 TO 300 kV*. Los Alamos National Lab.(LANL), Los Alamos, NM (United States).
- Storm, L., & Israel, H. I. (1970). Photon cross sections from 1 keV to 100 MeV for elements $Z= 1$ to $Z= 100$. *Atomic Data and Nuclear Data Tables*, 7(6), 565–681.
- Syahfitri, W. Y. N., Kurniawati, S., Adventini, N., & Lestiani, D. D. (2013). *Evaluasi penerapan energi dispersive X-Ray fluorescence (Ed-Xrf) untuk analisis coal fly ash*.
- Taam, I., Mantovano, J. L., Gante, V., & Jesus, C. S. (2013). *Quantitative analysis of rare earths by x-ray fluorescence spectrometry*.

- Takahashi, T., & Thornton, B. (2017). Quantitative methods for compensation of matrix effects and self-absorption in Laser Induced Breakdown Spectroscopy signals of solids. *Spectrochimica Acta Part B: Atomic Spectroscopy*, 138, 31–42.
- Takaya, Y., Yasukawa, K., Kawasaki, T., Fujinaga, K., Ohta, J., Usui, Y., Nakamura, K., Kimura, J.-I., Chang, Q., Hamada, M., Dodbiba, G., Nozaki, T., Iijima, K., Morisawa, T., Kuwahara, T., Ishida, Y., Ichimura, T., Kitazume, M., Fujita, T., & Kato, Y. (2018). The tremendous potential of deep-sea mud as a source of rare-earth elements. *Scientific Reports*, 8(1), 5763. <https://doi.org/10.1038/s41598-018-23948-5>
- Tang, K., & Gomez, A. (1994). Generation by electrospray of monodisperse water droplets for targeted drug delivery by inhalation. *Journal of Aerosol Science*, 25(6), 1237–1249.
- Taylor, S. R., & McLennan, S. M. (1985). *The continental crust: Its composition and evolution*.
- Theodorakou, C., & Farquharson, M. J. (2008). Human soft tissue analysis using x-ray or gamma-ray techniques. *Physics in Medicine & Biology*, 53(11), R111.
- Thomas, P. J., Carpenter, D., Boutin, C., & Allison, J. E. (2014). Rare earth elements (REEs): Effects on germination and growth of selected crop and native plant species. *Chemosphere*, 96, 57–66.

- Totland, M., Jarvis, I., & Jarvis, K. E. (1992). An assessment of dissolution techniques for the analysis of geological samples by plasma spectrometry. *Chemical Geology*, 95(1–2), 35–62.
- Tsai, C. S., & Yeh, S. J. (1997). Determination of rare earth elements in Taiwan monazite by chemical neutron activation analysis. *Journal of Radioanalytical and Nuclear Chemistry*, 216(2), 241–245.
- Tsuji, K., Injuk, J., & Van Grieken, R. (2005). *X-ray spectrometry: Recent technological advances*. John Wiley & Sons.
- Tsuruta, T. (2005). Separation of rare earth elements by microorganisms. *Journal of Nuclear and Radiochemical Sciences*, 6(1), 81–84.
- Tupaz, C. A. J., Watanabe, Y., Sanematsu, K., & Echigo, T. (2020). Mineralogy and geochemistry of the Berong Ni-Co laterite deposit, Palawan, Philippines. *Ore Geology Reviews*, 125, 103686.
- Tyler, G. (2004). Rare earth elements in soil and plant systems-A review. *Plant and Soil*, 267(1), 191–206.
- USGS. (2002). *Rare Earth Elements—Critical Resources for High Technology* | USGS Fact Sheet 087-02. <https://pubs.usgs.gov/fs/2002/fs087-02/>
- Valeton, I. (1972). Developments in Soil Science—1. *Bauxites*; Elsevier: Amsterdam, The Netherlands.
- Van Espen, P., & Lemberge, P. (2000). ED-XRF spectrum evaluation and quantitative analysis using multivariate and nonlinear techniques. *Advances in X-Ray Analysis*, 43, 560–569.
- Van Gosen, B. S., Verplanck, P. L., Seal II, R. R., Long, K. R., & Gambogi, J. (2017). *Rare-earth elements*. US Geological Survey.

- Van Grieken, R. E., & Markowicz, A. A. (2002). Revised and expanded. *Handbook of X-Ray Spectrometry*.
- Van Grieken, R., & Markowicz, A. (2001). *Handbook of X-ray Spectrometry*. CRC press.
- Vekemans, B., Janssens, K., Vincze, L., Adams, F., & Van Espen, P. (1995). Comparison of several background compensation methods useful for evaluation of energy-dispersive X-ray fluorescence spectra. *Spectrochimica Acta Part B: Atomic Spectroscopy*, 50(2), 149–169.
- Ventura, L., Amaral, B. S., Wanderley, K. B., Godoy, J. M., & Gioda, A. (2014). Validation method to determine metals in atmospheric particulate matter by inductively coupled plasma optical emission spectrometry. *Journal of the Brazilian Chemical Society*, 25(9), 1571–1582.
- Verplanck, P. L. (2014). *A deposit model for carbonatite and peralkaline intrusion-related rare earth element deposits: Chapter J in Mineral deposit models for resource assessment*.
- Vind, J., Malfliet, A., Blanpain, B., Tsakiridis, P. E., Tkaczyk, A. H., Vassiliadou, V., & Papias, D. (2018). Rare earth element phases in bauxite residue. *Minerals*, 8(2), 77.
- Vo-Dinh, T. (2006). *Handbook of spectroscopy*. John Wiley & Sons.
- Vogel-Mikuš, K., Arčon, I., Kump, P., Pelicon, P., Nečemer, M., Vavpetič, P., Koren, Š., & Regvar, M. (2012). 25 Analytical Tools for Exploring Metal Accumulation and Tolerance in Plants. *Phytotechnologies: Remediation of Environmental Contaminants*, 443.

- Vysetti, B., Vummiti, D., Roy, P., Taylor, C., Kamala, C. T., Satyanarayanan, M., Kar, P., Subramanyam, K. S. V., Raju, A. K., & Abburi, K. (2014). Analysis of geochemical samples by microwave plasma-AES. *Atomic Spectroscopy*, 35(2), 65–78.
- Wakabayashi, T., Ymamoto, A., Kazaana, A., Nakano, Y., Nojiri, Y., & Kashiwazaki, M. (2016). Antibacterial, antifungal and nematicidal activities of rare earth ions. *Biological Trace Element Research*, 174(2), 464–470.
- Walsh, J. N., Buckley, F., & Barker, J. (1981). The simultaneous determination of the rare-earth elements in rocks using inductively coupled plasma source spectrometry. *Chemical Geology*, 33(1–4), 141–153.
- Wendt, R. H., & Fassel, V. A. (1965). Induction-Coupled Plasma Spectrometric Excitation Source. *Analytical Chemistry*, 37(7), 920–922.
- Wengert, G. B., Walker, R. C., Loucks, M. F., & Stenger, V. A. (1952). Gravimetric determination of thorium and rare earth elements in magnesium alloys. *Analytical Chemistry*, 24(10), 1636–1638.
- Wu, Z. M., & Guo, B. S. (1995). Application of rare earth elements in agriculture and medicines. *Bioinorganic Chemistry of Rare Earth Elements*, 13–55.
- Yasukawa, K., Nakamura, K., Fujinaga, K., Machida, S., Ohta, J., Takaya, Y., & Kato, Y. (2015). Rare-earth, major, and trace element geochemistry of deep-sea sediments in the Indian Ocean: Implications for the

potential distribution of REY-rich mud in the Indian Ocean.

Geochemical Journal, 49(6), 621–635.

<https://doi.org/10.2343/geochemj.2.0361>

Zaitsev, E. I., Sotskov, Y. P., & Reznikov, R. S. (1978). *Neutron activation analysis of rocks for rare elements. Nejtronno-aktivatsionnyj analiz gornykh porod na redkie ehlementy.*

Zawisza, B., Pytlakowska, K., Feist, B., Polowniak, M., Kita, A., & Sitko, R. (2011). Determination of rare earth elements by spectroscopic techniques: A review. *Journal of Analytical Atomic Spectrometry*, 26(12), 2373–2390.

Zeng, Z., Ma, Y., Yin, X., Selby, D., Kong, F., & Chen, S. (2015). Factors affecting the rare earth element compositions in massive sulfides from deep-sea hydrothermal systems. *Geochemistry, Geophysics, Geosystems*, 16(8), 2679–2693.

Zepf, V. (2013). *Rare Earth Elements: New Approach to the Nexus of Supply.* Springer Berlin Heidelberg.

Zhang, H., Feng, J., Zhu, W., Liu, C., & Gu, J. (2000). Bacteriostatic effects of cerium-humic acid complex. *Biological Trace Element Research*, 73(1), 29–36.

Zhong, Y., Chen, Z., Gonzalez, F. J., Zheng, X., Li, G., Luo, Y., Mo, A., Xu, A., & Wang, S. (2018). Rare earth elements and yttrium in ferromanganese deposits from the South China Sea: Distribution, composition and resource considerations. *Acta Oceanologica Sinica*, 37(7), 41–54.

Zhu, J. G., Chu, H. Y., Xie, Z. B., & Yagi, K. (2002). Effects of lanthanum on nitrification and ammonification in three Chinese soils. *Nutrient Cycling in Agroecosystems*, 63(2), 309–314.



APPENDICES

APPENDIX A

SAMPLE DK8

Element	Ag-x-ray tube XRF	Am-241	ICP-MS	INAA
Sc	6.7	5.8	6	5.9
Y		51.5	54	
La		101.5	147	244
Ce	184	119.4	212	559
Nd		62.1	60.6	60.2
Sm			15.5	25.8
Eu	30.4	20	34.9	30.9
Gd		4		
Er			3.7	5.1
Tb	50.6			5.3
Yb			13	22.4
Lu			2.6	

APPENDIX B

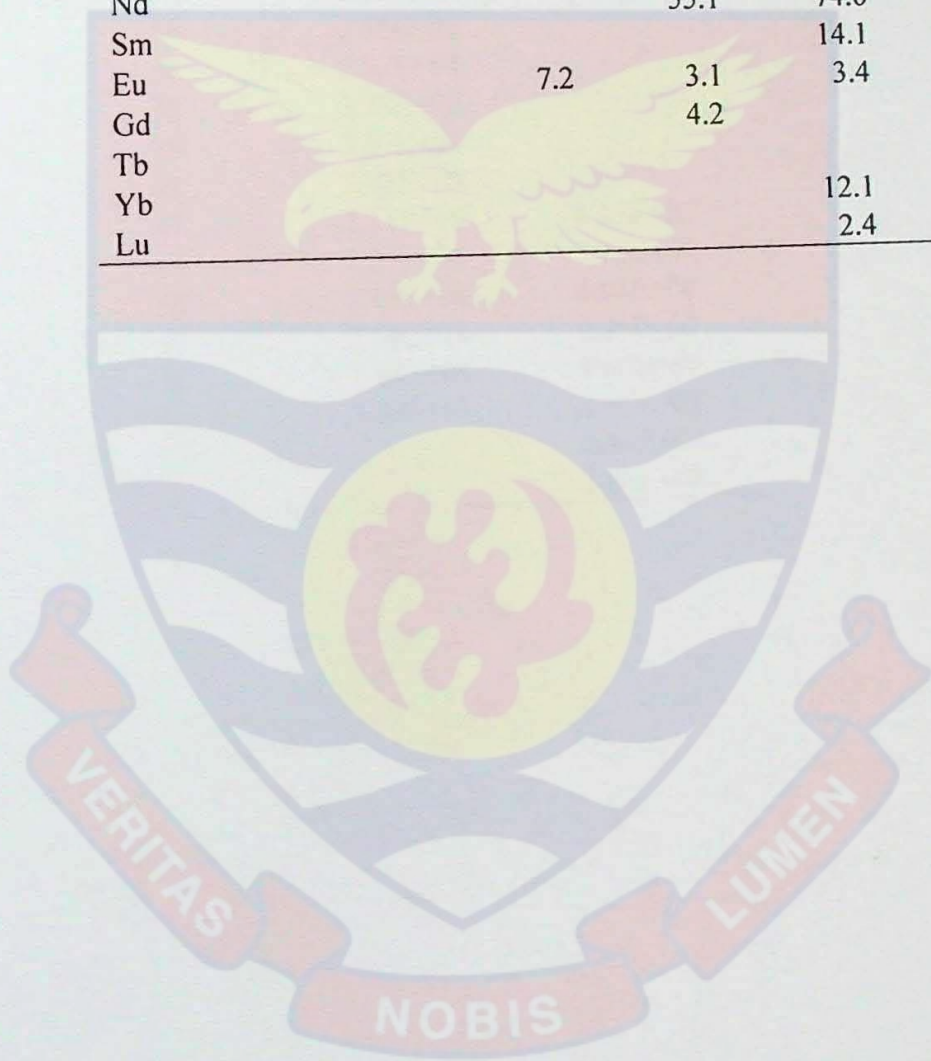
SAMPLE DK7

Element	Ag-x-ray tube XRF	Am-241	ICP-MS	INAA
Sc	6.8	5.9	6	6.2
Y		51.6	54.5	
La		99.2	144	204
Ce	27	116	207	229
Nd		35.4	15.7	22.2
Sm			15.7	22.2
Eu	20.1	3.3	3.7	5.5
Gd		3.9		
Er		1.5	1.6	1.7
Tb	20.2			3.9
Yb			12.7	18.7
Lu			2.7	

APPENDIX C

SAMPLE DK6

Elements	Ag-x-ray tube XRF	Am-241	ICP-MS	INAA
Sc	6.9	6.3	6	5.9
Y		50	49.7	
La	92.7	91.6	133	210
Ce	704	107	119	106
Nd		55.1	74.6	73
Sm			14.1	21.3
Eu	7.2	3.1	3.4	4.4
Gd		4.2		
Tb				3.1
Yb			12.1	12.5
Lu			2.4	2.6



APPENDIX D
SENSITIVITY LINE

Atomic Number	K-Sensitivity	L-Sensitivity
20	5.69E+07	
22	8.89E+07	
24	1.25E+08	
26	1.57E+08	
28	1.90E+08	
29	2.23E+08	
30	2.52E+08	
33	2.92E+08	
35	3.39E+08	
38	3.57E+08	
42	2.12E+08	
47	2.11E+08	6.33E+06
48	2.23E+08	7.12E+06
50	2.45E+08	8.02E+06
53	2.54E+08	2.26E+07
55	2.54E+08	4.64E+07
56	2.50E+08	6.67E+07
80		8.64E+07
82		1.06E+08

